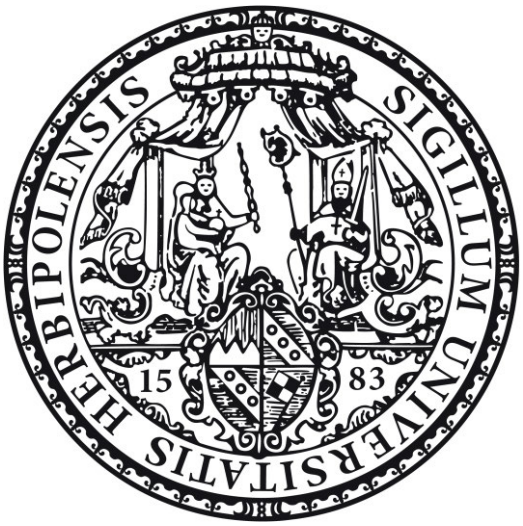

Expanding the Processability of Polymers for a High-Resolution 3D Printing Technology

Erweiterung der Verarbeitbarkeit von Polymeren für eine hochauflösende 3D-Drucktechnologie

Doctoral thesis for a doctoral degree
at the Graduate School of Life Sciences,
Julius-Maximilians-Universität Würzburg

Section: Biomedicine

submitted by
Juliane Carolin Kade

from Bad Mergentheim

Würzburg 2021

Submitted on / *Eingereicht am*:

Stamp / *Stempel* Graduate School

Members of the Thesis Committee / *Mitglieder des Promotionskomitees*

Chairperson / *Vorsitz*:	Prof. Dr. Carmen Villmann
Primary Supervisor / *Erster Betreuer*:	Prof. Dr. Paul D. Dalton
Supervisor (Second) / *Zweiter Betreuer*:	Prof. Dr. Robert Luxenhofer
Supervisor (Third) / *Dritter Betreuer*:	Prof. Dr. Rylie Green
Additional Examiners / *Weitere Prüfer*:	

Date of Public Defence / *Tag des Promotionskolloquiums*: 31.03.2022

Date of Receipt of Certificates / *Tag des Erhaltens der Urkunde*:

“Be like a flower,

survive the rain but use it to grow.”

- Unknown -

This work was conducted from January 2019 to December 2021 at the Department for Functional Materials in Medicine and Dentistry and at the Chair for Advanced Materials Synthesis at the University of Würzburg under the supervision of Prof. Dr. Paul Dalton.

Summary / Zusammenfassung

Summary

This thesis identifies how the printing conditions for a high-resolution additive manufacturing technique, melt electrowriting (MEW), needs to be adjusted to process electroactive polymers (EAPs) into microfibers. Using EAPs based on poly(vinylidene difluoride) (PVDF), their ability to be MEW-processed is studied and expands the list of processable materials for this technology.

PVDF-based materials are most commonly processed via film drawing and solution electrospinning that differ from melt processing into three dimensional (3D) structures. MEW enables the direct writing of polymers allowing high control over the fiber placement without the need of toxic solvents, as well as the fabrication of 3D structures for further applications in biomedical and/or electronical devices. PVDF has previously been MEW-processed into biomedical scaffolds, resulting in electroactive properties.[1] Warping and lifting during the fabrication process, however, limited the potential designs. In this thesis, the influence of a heated collector onto the warping process is studied resulting in improved stacking and fiber fusion. The collector temperature leads to slower solidification of the melt and thereby resulting in layer merging enabling better stability of the PVDF scaffolds. Depending on the collector temperature used, coalescent spheres appear on the scaffolds leading to biomimetic structures. → Chapter 2 - *Melt electrowriting of poly(vinylidene difluoride) using a heated collector.*

In order to impart controllable properties post-printing, magnetic carbonyl iron (CI) particles in different concentrations are compounded into a PVDF polymer matrix. The compounds are tested regarding their printability and the influence of the particle content on the MEW-processing. Particle contents of up to 30 wt.% are printable into fibers without nozzle clogging and appear as grey/black colored scaffolds. With increasing particle content, the fiber morphology changes from smooth to rough with visible CI particles on the surface. Printed constructs demonstrated movement due to the CI particles being attracted to magnets. → Chapter 3 - *Effect of carbonyl iron particles on the melt electrowriting process.*

Furthermore, poly(vinylidene fluoride-*co*-trifluoroethylene) (P(VDF-*co*-TrFE)), the PVDF copolymer, is also direct-written for the first time. The molten jet of the highly viscous polymer does not adhere to the collector at room temperature and a heated collector substrate is needed to enable sufficient adherence. At collector temperatures of 120 °C or higher, MEW-processing is possible at collector speeds between 10 to 100 mm/min resulting in straight lines. The fiber morphology indicates

spherulites and changes to lamella-like structures with increasing collector speeds. Furthermore, when cooling down the collector temperature, the straight fibers turn into sinusoidal structures depending on the number of stacked layers. → Chapter 4 - *Melt Electrowriting of poly(vinylidene fluoride-co-trifluoroethylene).*

In the final research chapter, a coaxial MEW system is investigated to enable the fabrication of dual material fibers. Therefore, neat poly(ε-caprolactone) (PCL) has been used as the shell material and PCL containing CI particles as the core. The combination of a light and a dark material is chosen to visualize the placement of the two materials within the fibers using an optical light microscope. The influence of the printing speed, as well as the applied pressure onto both materials is studied for two different nozzle setups. The shell nozzle is kept constant while changing the diameter of the core resulting in different ratios of the two materials. The resulting fibers are dual-material fibers consisting of the neat PCL and the PCL containing CI particles. Nevertheless, the current nozzle setup is leading to alternating Janus- and coaxial fibers depending on the printing direction, due to the core nozzle design. → Chapter 5 – *Establishing a coaxial MEW system.*

Zusammenfassung

Im Rahmen dieser Arbeit wird *melt electrowriting* (MEW), eine hochauflösende additive Fertigungstechnik, zur Herstellung von Polymerfasern im unteren Mikrometerbereich eingesetzt. Neue Materialien, hauptsächlich elektroaktive Polymere (EAPs) auf Basis von Poly(vinylidendifluorid) (PVDF), werden hinsichtlich ihrer Druckbarkeit untersucht, um die Liste der prozessierbaren Materialien für diese Technologie zu erweitern.

PVDF-basierte Materialien werden in der Regel durch Filmziehen und *solution electrosprinning* verarbeitet, was die Herstellung von dreidimensionalen (3D) Proben erschwert und/oder eine gute Kontrolle über die Faserplatzierung verhindert. Im Gegensatz dazu ermöglicht MEW das direkte Schreiben von Polymeren mit hoher Kontrolle über die Faserplatzierung ohne giftige Lösungsmittel, sowie die Herstellung von 3D-Strukturen für Anwendungen in biomedizinischen und/oder elektronischen Bereichen. PVDF wird bereits mit MEW zu so genannten *Scaffolds* verarbeitet, die zu elektroaktiven Proben führen.[1] Allerdings ist die Schichthöhe aufgrund von Verformungen und teilweisem Ablösen der Proben während des Herstellungsprozesses begrenzt. In diesem Kapitel wird der Einfluss eines beheizten Kollektors auf den Verformungsprozess untersucht, was eine verbesserte Stapelung und Faserverschmelzung der einzelnen Fasern in der Probe bewirkt. Die erhöhte Kollektortemperatur verlangsamt die Erstarrung der Schmelze und führt zu einem Zusammenschmelzen der Schichten, wodurch eine bessere Stabilität der PVDF-Gerüste erzielt wird. In Abhängigkeit von der verwendeten Kollektortemperatur entstehen auf den Gerüsten vereinigende Kugeln, die biomimetische Strukturen verursachen. → Kapitel 2 - *Melt electrowriting of poly(vinylidene difluoride) using a heated collector.*

Im nächsten Kapitel werden magnetische Carbonyleisen (CI)-Partikel in unterschiedlichen Konzentrationen in eine PVDF-Polymermatrix eingearbeitet, um die Materialeigenschaften zu verändern. Die entstehenden Materialien werden auf ihre Druckbarkeit und den Einfluss des Partikelgehalts auf die MEW-Verarbeitung getestet. Partikelgehalte von bis zu 30 Gew.-% sind druckbar, ohne dass es zu Düsenverstopfungen kommt und resultieren in grau bis schwarz gefärbte Fasergerüste. Mit steigendem Partikelgehalt verändert sich die Fasermorphologie von glatt zu rau mit sichtbaren CI-Partikeln auf der Oberfläche. Die gedruckten Konstrukte zeigen magnetische Eigenschaften, ausgelöst durch die eingebetteten CI-Partikel. → Kapitel 3 - *Effect of carbonyl iron particles on the melt electrowriting process.*

Darüber hinaus wird im Rahmen dieser Arbeit auch das PVDF-Copolymer Poly(vinylidenfluorid-*co*-trifluorethylen) (P(VDF-*co*-TrFE)) gedruckt. Der Polymerstrahl des hochviskosen P(VDF-*co*-TrFE) haftet bei Raumtemperatur nicht am Kollektor, und ein beheiztes Kollektorsubstrat war erforderlich, um eine ausreichende Haftung zu ermöglichen. Bei Kollektortemperaturen von 120 °C oder höher ist die MEW-Verarbeitung bei Kollektorgeschwindigkeiten zwischen 10 und 100 mm/min möglich, was zu geraden Faserlinien führt. Die Fasermorphologie zeigt Sphärolithe und geht mit zunehmender Kollektorgeschwindigkeit in lamellenartige Strukturen auf der Faseroberfläche über. Zusätzlich verändern sich die geraden Fasern beim Abkühlen der Kollektortemperatur in sinusförmige Strukturen. → Kapitel 4 – *Melt Electrowriting of poly(vinylidene fluoride-co-trifluoroethylene).*

Im letzten Kapitel wird ein bereits vorhandener Drucker modifiziert, um ein koaxiales MEW-System zu etablieren, das die Herstellung von Fasern aus zwei Materialien ermöglicht. Dazu wird reines Poly(ε-caprolacton) (PCL) als äußeres und PCL mit CI-Partikeln als Kernmaterial verwendet. Die Kombination aus einem hellen und einem dunklen Material wird gewählt, um die Platzierung der beiden Polymere in den Fasern mit Hilfe eines optischen Lichtmikroskops sichtbar zu machen. Der Einfluss der Druckgeschwindigkeit, sowie der auf beide Materialien ausgeübten Druck, wird für zwei verschiedene Düsenkonfigurationen untersucht. Die äußere Düse bleibt konstant, während der Durchmesser der inneren Nadel verändert wird. Die resultierenden Fasern bestehen somit aus zwei Polymeren, dem reinen PCL und dem PCL mit CI-Partikeln. Allerdings führt das aktuelle Nadelsetup, abhängig von der Druckrichtung, abwechselnd zu *Janus*- und koaxialen Fasern, da die innere Nadel nicht perfekt in der äußeren Nadel zentriert ist. → Kapitel 5 - *Establishing a coaxial MEW system.*

Table of Contents

Aims and Motivation

Aims and Motivation

In this thesis, melt electrowriting (MEW) has been used as the 3D printing method to process polymer melts into fibers and porous materials. MEW is a high-resolution additive manufacturing technique capable of producing fibers without the need of toxic solvents. The extruded polymer melt is pulled and stretched into a thin jet that is direct written onto a collector. The applied voltage is stabilizing the polymer jet allowing a continuous polymer flow and the electrohydrodynamic principle leads to fibers with diameters typically ranging between 5 to 50 µm. As MEW is still a quite young technique, only a limited amount of processable materials have been investigated. However, within the last years, the interest in the technique and the resulting research has been dramatically increased. More and more publications are dealing with adjustments and improvements of the MEW printer for example enabling to process new materials.

Within this thesis, the general aim is to further expand the list of processable materials mainly focused on poly(vinylidene difluoride) (PVDF)-based polymers. As those materials are of increasing interest due to their electroactive nature, the most common processing techniques are film drawing, casting or electrospinning and are based on polymer solutions using expensive and toxic solvents. Additionally, these techniques do not allow the fabrication of complex designs and/or the fabrication of samples with accurate fiber placement. MEW enables the fabrication of highly porous scaffolds with resulting fibers in the lower diameter range without the need of solvents. Therefore, improving and expanding the list of processable electroactive polymers based on PVDF via MEW would enable the fabrication of highly porous scaffolds with controllable geometries. Additionally, such piezoelectric samples offer potential use in biomedical applications especially for muscle, nerve, and bone regeneration, as well as electrical devices in need of small fibers placed in high precision and complex geometries.

To overcome this limitation, within this thesis a general aim is to improve and expand the printability of the PVDF-based polymers. Furthermore, another aim is to establish a coaxial MEW system enabling the combination of dual material fibers.

Accordingly, this thesis can be divided in four main chapters:

1) Improving the MEW-printability of PVDF by introducing a heated collector (Chapter 2).
2) Investigation of effect on blended magnetic carbonyl iron particles embedded in PVDF on the MEW-processability (Chapter 3).

3) Establishing the direct-writing via MEW of a highly viscous PVDF copolymer (P(VDF-*co*-TrFE)) (Chapter 4).
4) Setting up and establishing a coaxial MEW print head to fabricate dual material fibers based on PCL (Chapter 5).

Chapter 1

– Introduction

Chapter 1 was published as original review article (Kade, J. C., Dalton, P. D., *Polymers for Melt Electrowriting*. Advanced Healthcare Materials, 2020, 10, 2001232. https://doi.org/10.1002/adhm.202001232), reproduced from © 2020 The Authors. Published by Wiley-VCH GmbH.

The original text was slightly modified to improve readability.

1.1 Abstract

Melt electrowriting (MEW) is an emerging high-resolution additive manufacturing technique based on the electrohydrodynamic processing of polymers. MEW is predominantly used to fabricate scaffolds for biomedical applications, where the microscale fiber positioning has substantial implications in its macroscopic mechanical properties. This review gives an update on the increasing number of polymers processed via MEW and different commercial sources of the gold standard poly(ε-caprolactone) (PCL). A description of MEW-processed polymers beyond PCL is introduced, including blends and coated fibers to provide specific advantages in biomedical applications. Furthermore, a perspective on printer designs and developments is highlighted, to keep expanding the variety of processable polymers for MEW.

1.2 Introduction

Additive manufacturing (AM) is increasingly used for applications in biomaterials, tissue engineering, and biofabrication partly due to the potential fabrication of patient-specific designs.[1] In general, every fabrication technology has an ideal printing resolution range and for many techniques this is ≈50–500 µm.[2, 3] For biomedical applications that aim to replicate the tissue microarchitecture, it is necessary to be able to print even smaller structural features in the low micrometer or nanometer scale. Such small fiber diameters can be facilitated with electrohydrodynamic (EHD) techniques such as solution electrospinning (SES), melt electrospinning (MES), and melt electrowriting (MEW).[4] This review is directed at the latter AM technology, highlighting the different materials that have been used and provide a forward perspective on the material options for this technique.

1.3 What Is MEW?

MEW is a high-resolution AM method with the capability to produce fibers in the micro- and nanometer range using a similar configuration to MES, except using different parameters and with a moving collector that facilitates direct-writing.[5] A MEW device consists of a printing head equipped with a heating system to melt the material within a syringe, which is delivered to a metal nozzle. The MEW head is configured with a computer-aided translating system so that direct writing onto a collector is established. A delivery system (typically air pressure) forces the extrusion of the polymer melt through the nozzle and an applied potential difference between the nozzle to the collector leads to an electrical field. While this configuration has similarities to electrospinning, there are important distinctions between MEW and MES with respect to ideal parameters, particularly the collector distance and the required electric field.[6]

Applying an electric field concentrates charges in the fluid drop at the closest point to the collector. In SES, these charges overcome the surface tension forces and a conical-shaped jet is ejected toward the collector. The beginning of this jet and the remaining fluid at the tip of the nozzle is termed as the *Taylor cone*, named after Sir Geoffrey Taylor, a 20th century physicist who performed substantial fluid mechanics research including EHD phenomenon.[7] For SES, this is a rapid event with a *Taylor cone* generated within seconds, as soon as the applied electrical field overcomes the surface tension of the droplet at the tip of the nozzle.[8, 9] As the jet approaches the collector for SES and MES, the surface charges increase in density to a level that secondary electrical instabilities, often called *whipping*,

occur.[10] There are even further levels of electrical instability that stretch the jet into the nanoscale dimensions typically observed for SES.[8]

Figure 1A shows how jet initiation for MEW occurs. Similar to SES, applying an electric field results in charges aggregating at the part of the drop closest to the electric field. Polymer melts used in effective MEW, however, are typically more viscous and have less molecular species capable of charging compared to solvent-based systems.

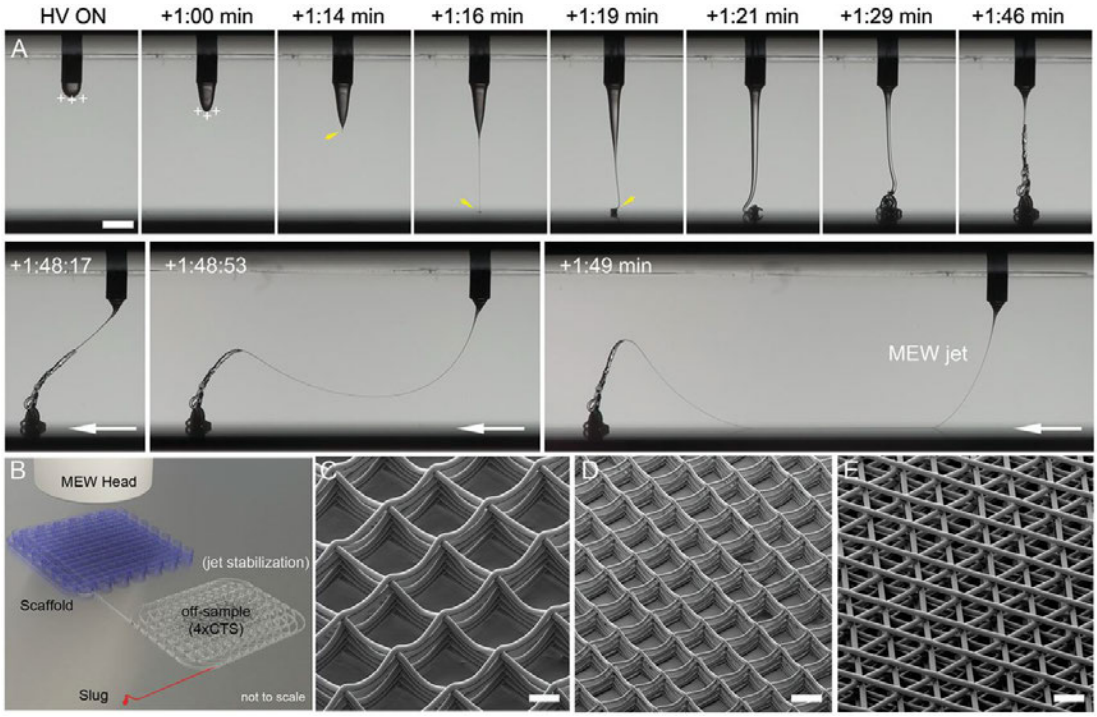

Figure 1. MEW jet initiation of poly(ε-caprolactone) and examples of scaffolds. A) Photograph sequence with time indicated after high voltage (HV) application. When an electric field is applied to a PCL melt drop, charges aggregate at the surface of the liquid closest to the collector. As the drop increases in volume, it is distorted after +1:00 min, leading to a fluid column and jet at +1:16 min (yellow arrow). Another 30 s is required for the excess volume in the *Taylor cone* to be drawn to the collector, at which time (+1:48 min), the MEW jet is ready to direct-write. B) Schematic showing how this jet initiation can be followed by a stabilization pattern off-sample, with the slug being the collected material in the jet initiation step shown in (A). SEM images of MEW scaffolds in a box morphology using different diameter fibers of C) 20 µm and D) 10 µm and fiber spacings of 250 µm and 125 µm, respectively. E) The hexagonal laydown pattern results in a triangular morphology. A) Snapshots from a previously unpublished video kindly provided by Mr. Thomas Robinson. B) Adapted with permission under the terms of the Creative Commons Attribution-NonCommercial License.[11] Copyright 2017 The Authors. Published by Wiley-VCH GmbH. C–E) Reproduced with permission.[12] Copyright 2019, Mary Ann Liebert, Inc. Scale bars: (A) = 1 mm; (C)–(E) = 100 µm.

As shown in Figure 1A, this charge concentration does not overcome surface tension and no jet is formed for over a minute. As the *Taylor cone* is filled with more molten polymer, the weight of the melt begins to neck from the initial droplet forming

a thin column. This proceeds until the forces (gravitational and charges) draw the solidified polymer to be in contact with the collector (Figure 1A). While variations on this jet initiation can occur, such as the solidification of the polymer drop before reaching the collector, only when the polymer touches the collector can direct-writing be commenced. The initiation of a jet within MEW depends on the mass flow rate to the nozzle, applied voltage, and collector distance, and can take in the order of several or even tens of minutes, depending on the flow rate and/or melt viscosity. The molten jet is stabilized with the voltage and the whipping that is associated with electrospinning does not occur.

This EHD effect that prevents Plateau–Rayleigh instabilities allows the nozzle flow rate to be substantially reduced for MEW.[5, 13] Additionally, the comparable high viscosity and low conductivity of melt fluids support the control and stability of the jet.[5, 13-15] This in combination with the controllable collector plate, allows the defined deposition of the jet, which starts to solidify on the way to the collector enabling the layer-by-layer process.[5, 13] Depending on the printing parameters, the resulting fiber diameter can be controlled, adjusted, and direct-written in different configurations (Figure 1B–E).[11, 16] The controlled fiber placement of small diameter fibers allows one to print porous structures, called scaffolds, that are used in biomedical sciences.[5, 17, 18]

Depending on the collector speed, the jet can be deposited as straight lines as soon as the collector speed is higher than the critical translation speed (CTS) of the polymer melt.[11] The CTS is defined as the speed at which the jet results in straight lines. This phenomenon is analogous to the liquid rope coiling of a viscous thread solution.[5, 19]

1.4 Poly(*ε*-caprolactone) (PCL)

Without question, the current gold standard polymer used for MEW is PCL.[11, 16] In the literature, studies are performed with different designs including the typical box-structured scaffolds[16] or scaffolds for cell experiments[20-22] to more complicated designs like sinusoid structures with horizontal layer stacking,[23] tubes,[24, 25] or a fiber-hydrogel composite with mechanical properties similar to that of a heart valve.[26]

Why PCL?

PCL is a semicrystalline, biodegradable polyester that is readily processable via MEW due to its low melting temperature[5, 27] and rapid solidification.[28] It is favorable from the biomedical perspective as it is approved by the U.S. Food and

Drug Administration (FDA) for certain clinical purposes[29] and offers a slow degradation rate up to several years.[18, 27, 30] PCL is also well-studied in biomedical engineering as part of many other manufacturing technologies, such as SES, phase separation, and dip-coating. Its interaction with different cell types has been widely used for tissue engineering and in the biomedical field[27, 28, 30] due to the availability in different molecular weights.

For MEW, the most widely studied polymer is medical-grade PCL (PC12; Corbion, NL), which is made using good-manufacturing practices (GMP) (Table 1).

Table 1. Sources of linear PCL used for MEW.

Description	Properties	M_w [g mol^{-1}] (flow properties)	References
PURASORB PC12	Medical grade	Viscosity 1.2 dL g^{-1} Measured as $M_w = 80$ kDa[31]	[11,16,12,20,22–24,26,31–55]
Sigma Aldrich	Product number 440744[46]	$M_n = 80 \times 10^3$[5,21,56,57] $M_n = 35 \times 10^3$ $M_w = 83 \times 10^3$[13] $M_w = 45$ kDa[58–60] $M_n = 45 \times 10^3$[61]	[5,13,21,56–61]
Capa 6400		$M_w \approx 37 \times 10^3$ a) MFI = 40 b)	[62,63]
Capa 6430		$M_w \approx 43 \times 10^3$ a) MFI = 40 b) $M_n = 83$ kDa[14] $M_w = 37$ kDa[64]	[14,25,64–66]
Capa 6500		$M_w \approx 50 \times 10^3$ a) MFI = 7 b) $M_w = 45.6 \times 10^3$[67,68] $M_w = 50$ kDa[64]	[5,67,68,64,15]
Capa 6500C	High clarity grade when molten	$M_w = 50 \times 10^3$ a)[69] MFI = 7 b)	[69,70]
Capa 6506	Medical grade	$M_w = 50$ kDa[29]	[29]
Capa 6800		$M_w \approx 80 \times 10^3$ a) MFI = 3 b)	[71]
CELLINK		$M_n = 5000$[72]	[72]

Note: Weight average molecular weight (M_w); number average molecular weight (M_n).

a) Approximate molecular weight

b) Typical values, melt flow index (MFI) measured with 1 in. PVC die, 2.16 kg weight, g/10 min at indicated temperature; for 6200 s at 80 °C, 6500 and 6800 s at 160 °C. Values/information provided by Perstorp CAPA brochure.

Medical-grade PCL has improved purity compared to technical-grade PCL and, in our experience, produces the highest printing quality. Table 1 demonstrates an interesting perspective for MEW, that the gold standard polymer with the most processing knowledge is one made under GMP conditions.

As PCL is highlighted in several reviews on clinical translation of tissue engineering products, the transition from university-led research to application in the clinic is often negatively impacted by the need to repeat experiments with medical-grade polymers. In this instance, our understanding of processing via MEW is predominantly obtained with GMP-manufactured PCL. Using medical-grade PCL for MEW should therefore be the preferable material compared to technical-grade PCL as the processed structures and designs have excellent control and accuracy (Figure 1).

There are many studies investigating the printing parameters or phenomena using PCL[13, 11, 16, 67] so as to make different scaffold designs for biomedical applications.[3] This includes the standard box pore morphology scaffolds (Figure 1C,D) or triangular pore scaffolds (Figure 1E) that are followed by understanding how this influences cell morphology and cell adhesion,[20-22, 31, 46] including mathematical modeling of pore bridging dynamics.[66] However, more recently, complex designs or further improvements for specific applications are gaining more and more interest. Some designs approached are discussed next, while an in-depth review on MEW designs can be found elsewhere.

Importantly, MEW can be used to fabricate microstructures with tailored mechanical behavior and response. Depending on the direct-written fibers, the structures can result in ultra-stretchable scaffolds.[36] Those hexagonal scaffolds showed up to 40 times more elastic energy compared to rectangular box structures and exhibited large biaxial deformations. Furthermore, the hexagonal microstructures were used to engineer native-like myocardial muscle.[36]

Medical-grade PCL was used to fabricate constructs with different pattern designs similar to the wavy architecture of native collagen fibers to mimic the anisotropy and viscoelastic properties of native heart valve leaflets.[26] By changing design parameters like the radial fiber spacing, curvature degree, and number of printed layers, the fabricated constructs displayed tunable tensile properties. Furthermore, the scaffolds supported growth of human vascular smooth muscle cells and demonstrated excellent acute hydrodynamic performance under aortic physiological conditions in a custom-made flow loop offering a promising design approach for heart valve tissue engineering.[26]

Complex designs can not only be used to improve approaches regarding their specific applications but also can change the mechanical properties or result in auxetics, which expand in transverse directions when applying tensile load (Figure 2A). Normally, constructs with a positive Poisson´s ratio shrink under tensile loading.[25, 73] A similar approach is shown by Paxton *et al*.[25] fabricated MEW tubes with a negative Poisson´s ratio enabled expansion under tensile load based on a reentrant honeycomb unit cell design (Figure 2B). With this approach, the tubular scaffolds enabled a diameter increase up to 80.8%, depending on the applied tensile load, until the honeycomb design aligned with the axis of the tube.[25]

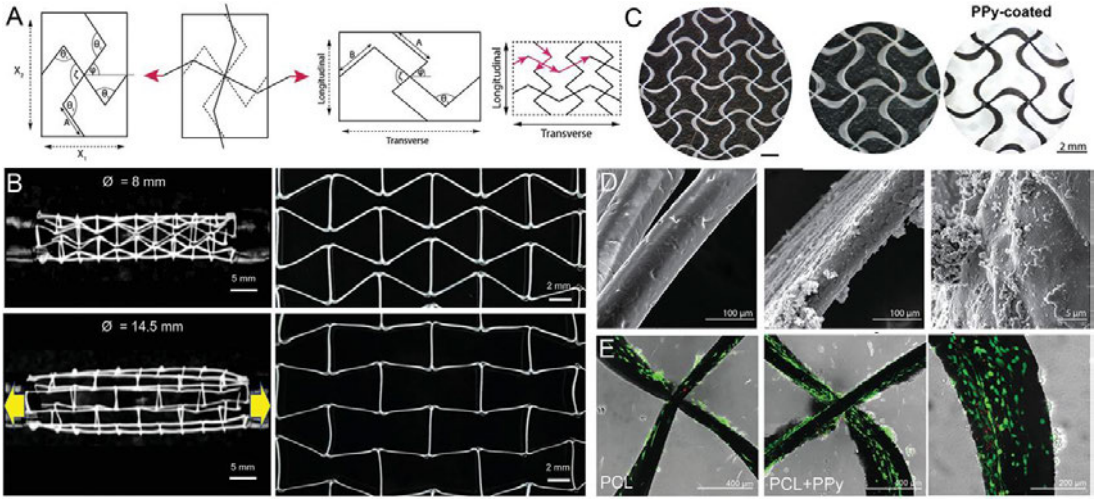

Figure 2. A) Schematic principle of auxetic designs with transverse expansion under tensile load and B) implemented in a tubular MEW scaffold. C) Polypyrrole (PPy) coating of auxetic patches enhancing electroconductive properties. D) Scanning electron microscope (SEM) images of neat PCL, PPy-coated MEW fibers and E) showing Live/dead staining of neonatal cardiac fibroblasts after 48 h on PCL and PPy-coated PCL fibers. A,C–E) Reproduced with permission.[58] Copyright 2020, Wiley-VCH GmbH. B) Adapted under the terms of the Creative Commons CC-BY license.[25] Copyright 2020 The Authors. Published by Elsevier Ltd.

Surface Coatings of PCL

PCL is a hydrophobic polymer and lacks bioactive cues, even though it supports cell attachment and proliferation through protein adsorption.[34, 74] Due to the hydrophobicity, air bubbles trapped between the PCL fibers can cause handling issues especially within cell culture media. To overcome this limitation, several studies have focused on hydrophilizing the PCL fiber surface and improving properties for cells,[32-34] adding electroactive cues to aid cell alignment[60] or to introduce specific properties by coating with calcium phosphate (CaP)[31, 51] or conductive materials.[58, 61]

Olvera *et al*.[58] fabricated an auxetic PCL patch with fiber diameters of 80–120 µm and a fiber spacing set to 2 mm, which is designed to adapt the strains and

stresses by the human myocardium and was treated with an electroconductive coating (Figure 2C,D). These patches were designed to offer the possibility of longitudinal and transverse deformations by the fabrication of missing-rib geometry for anisotropic behavior compared to the typical box-structured MEW scaffolds.[58] The PCL scaffolds were coated with polypyrrole (PPy) to impart the electroconductive properties for stimulating the human myocardium and those patches demonstrated cytocompatibility (Figure 2E).[58] The auxetic patches showed average values of electroconductivity of 2.51 ± 0.7 S m^{-1} in transverse direction and 2.07 ± 0.4 S m^{-1} in the longitudinal direction for a coating thickness of 0.77 ± 0.15 µm.[58]

Wang and colleagues sputter-coated box-structured PCL scaffolds with resulting fiber diameters of around 15 µm and fiber spacings of 200 µm with a nanolayer of gold (Au) ranging from 10 to 80 nm to enhance conductivity for the application in nerve regeneration (Figure 3A,C).[61] Due to the high flexibility and recoverability of the coated samples, the scaffolds were injectable through a nozzle. Furthermore, the Au coating enabled conductivity of 0.12 S cm^{-1} (Au thickness of 10 nm) to 1.39 S cm^{-1} (Au thickness of 80 nm) as demonstrated in Figure 3D and significantly increased the neurite number per cell and the neurite length, especially under electrical stimulation.[61]

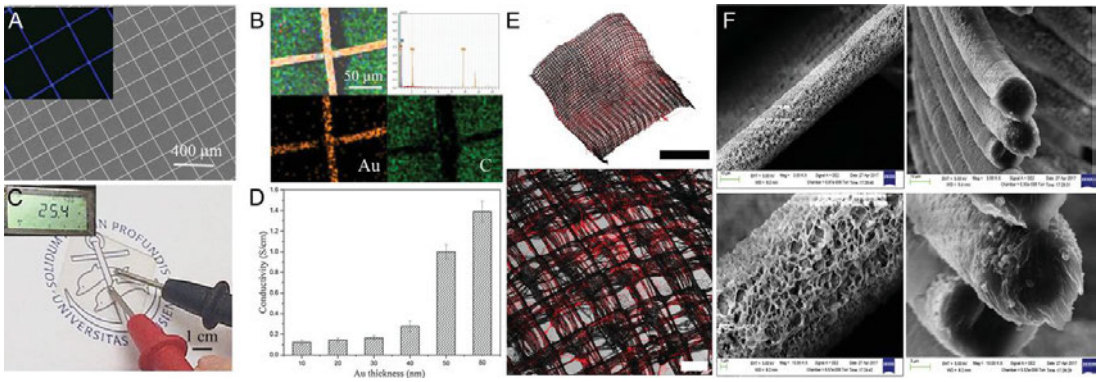

Figure 3. Various coating approaches for MEW scaffolds. A) SEM images of a gold (Au) coated PCL and B) EDS elemental analysis (Au in yellow and carbon in green). C) The resistance of the PCL scaffold coated with 50 nm Au and D) quantitative conductivity of the different thicknesses of Au coating. E) Confocal microscopy images of collagen-functionalized PCL scaffolds highlighted through red staining. F) SEM images of the inorganic CaP coating deposited on PCL fibers showing the surface morphology and cross sections of the fibers. A–D) Reproduced with permission.[61] Copyright 2020, Elsevier B.V. All rights reserved. E) Reproduced with permission.[33] Copyright 2019, Wiley-VCH GmbH. F) Reproduced with permission.[31] Copyright 2019, American Chemical Society. Scale bars: (B) = 5 mm and 200 µm and (F) = 10, 10, 1, and 3 µm, respectively.

As previously mentioned, coatings can reduce the hydrophobicity of PCL scaffolds resulting in improved handling during cell culture. Extracellular matrix (ECM) coatings on PCL are commonplace[75] and are also effective with MEW scaffolds. For example, an ECM suspension made from human decellularized adipose tissue provided an adipo-inductive microenvironment for human bone-marrow mesenchymal stromal cells (bmMSCs).[34] To both hydrophilize the PCL fibers and functionalize them, a hydrogel coating based on a six-arm star-shaped NCO-poly(ethylene oxide-*stat*-propylene oxide) (sP(EO-*stat*-PO)) was used to prevent unspecific interactions with proteins and cells.[33] Additionally, this approach offers the possibility to covalently attach bioactive molecules resulting in a photoactivatable scaffold that enables the binding of sterically demanding molecules via post-modification irrespective of time and pH.[33] This leads to a successful collagen coating (Figure 3E) with the collagen fibrils along the PCL fibers and biofunctionalization was proven by post-seeding of human MSCs showing a high cell viability after 8 days.[33]

CaP coatings are known to be hydrophilic,[31, 76] offer higher surface areas supporting cell adhesion and subsequent cellular behavior,[31, 77] and therefore offering promising results for bone regeneration using medical-grade PCL scaffolds.[31, 51] PCL fibers with diameters of 6 to 10 µm were coated with inorganic CaP and are shown in Figure 3F. The coating had no significant effect on the resulting pore size of the scaffolds or the fiber diameter but increased the surface area on the fiber.[31] Depending on the fiber spacing (250, 500, and 750 µm) within the scaffolds, as well as the fiber lay-down pattern with offsets (30/70 and 50/50) or gradient, the scaffolds resulted in different mechanical properties with Young's modulus ranging from 0.91 ± 0.25 kPa for the 750 µm spacing to 4.34 ± 0.32 kPa for the 250 µm fiber spacing.[31]

In a different study, a cell-accumulation and scaffold layering technique increased the thickness of medical-grade PCL scaffolds resulting in oriented capillary-like networks.[78] The PCL scaffolds were fibronectin-coated and then seeded with human umbilical vein endothelial cells and, afterward, with human dermal fibroblasts incorporated in a gelatin nanofilm.[78] With this technique, the orientation of capillary-like structures and the guidance of neovascular structures were successfully influenced into the center of the pores within the scaffolds. Furthermore, this approach should be easily applicable to other MEW-processable thermoresponsive polymers with the advantage of being dissolvable resulting in microchannel networks.[78]

Dissolvable Channels

The embedding of particulates/fibers to later dissolve them away is one technique to introduce porosity/channels within a hydrogel[69, 79] or polymer[80] as shown in Figure 4. Haigh *et al*.[79] submersed PCL scaffolds within poly(2-ethyl-2-oxazoline-*co*-2-(3-butenyl)-2-oxazoline) (PEtOx-ButenOx) copolymer hydrogels (Figure 4A). Afterward, the PCL was dissolved with an acetone:water solution resulting in porous hydrogel structures. The dissolved channels were then back-filled with a fluorescent dye.[79]

Wang and colleagues further built on this using both fused deposition modeling (FDM) and MEW to fabricate a PCL template, which was later embedded in a PEG hydrogel.[69] The swollen PEG enabled the simple removal of the PCL fibers and scaffolds (Figure 4B), then the resulting hollow structures post-treated with cell-adhesion peptides that allowed cell guidance throughout the channels without active perfusion.[69]

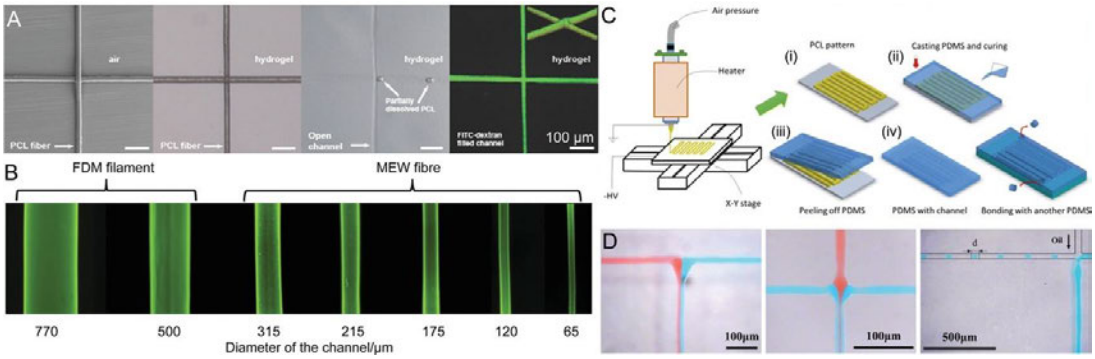

Figure 4. Dissolving MEW fibers to make channels. A) A series of images showing the PCL fibers embedded in a hydrogel that are then dissolved away and backfilled with fluorescent dye. B) Fluorescence images of FDM and MEW processed fibers resulting in channels with varying diameters. C) Schematic of inverse molding by curing the polymer PDMS around MEW fibers followed by delamination, for use as D) microfluidic systems. A) Reproduced with permission.[79] Copyright 2015, Wiley-VCH GmbH. B) Reproduced under the terms of the Creative Commons CC-BY license.[69] Copyright 2020 The Authors. Published by Wiley-VCH GmbH. C–D) Reprinted by permission.[80] Copyright 2020, Springer Nature.

Another MEW fiber dissolution approach also demonstrates microfluidic potential (Figure 4C,D). Once PCL fibers are printed, they are embedded in poly(dimethyl siloxane) (PDMS) and dissolved away afterward.[80] Laminar flow and controlled mixing is demonstrated in this study.[80] MEW-processed PCL was used as a dissolvable material embedded in an amorphous silica nanocomposite that is ultraviolet (UV)-crosslinked and subsequently heated to 1300 °C.[39] Thermal debinding and sintering of the silica nanocomposite resulted in suspended hollow

microstructures in fused silica glass for applications in optics and photonics, microfluidics, and lab-on-a-chip.[39]

1.5 Materials beyond PCL

There is a general lack of well-studied processable materials for MEW, contrasting with the many different polymers investigated and possible for SES.[18, 81] This is an indication of the early stage of development for the process, as the electrohydrodynamic effect of jet stabilization is generally applicable to fluids. Polymer solutions can similarly be direct-written with EHD principles,[82, 83] and there are differences with respect to electric field and fiber placement.[83] For biomedical applications, melt processing provides an opportunity to process polymers without toxic solvents within the fabrication process. However, this comes with limitations on the types of polymers that can be processed, including those that are thermally stable. Nonetheless, several important polymers (Table 2) such as poly(propylene) (PP), poly(vinylidene fluoride) (PVDF), and poly(2-oxazoline)s (POx) can be readily processed to provide different properties than MEW-processed PCL.

Table 2. List of MEW-processed polymers beyond PCL showing the resulting fiber diameters and the printing parameters used.

Polymer class		Fiber diameter [µm]	Layers	Nozzle diameter [Gauge]	Temperature [°C]	Voltage [kV]	Pressure [bar]	Speed [mm min^{-1}]	Distance [mm]	Reference
Polyesters	pHMGCL/PCL 40:60	3–7	25–30 200 × 200 µm 150 × 300 µm	27	84	5–8.5 5	1–4 2	600–2400 300	3–5 3	[84]
	Poly(urea-siloxane)s; thermoplastic elastomer	10.6 ± 0.6 to 19.5 ± 1.5	100 50 in *x*/*y*	24	80–100 90	8–12 10	1–3 2	1500–4000 2500	8.5	[85]
Water-soluble polymers	PEtOx	8–183	180	30, 27, 25, and 23	200–220 210	3–7 4	1–3 2	200–400	3–7 5	[86]
Hydrogel	PEtOzi	45 ± 5 (dry) 89 ± 12 (wet)	10 500 µm spacing	N/A	130 Spinneret 150	2–4	1.5–2	1300–1800	3.3	[87]
Photocurable polymers	Poly(LLA-*c*-CL-AC)	24.6 ± 2.7	20 100 µm	30	130 Spinneret 145	7	3	420	4.5	[88]
	Poly(*c*-CL-AC)	≈15–75 26.8 ± 1.9	10 5 in *x*/*y* 200 µm	30	90 Spinneret 105	7	0.3–4 1	100–810 300	4.5	[89]
Nondegradable polymers	PP	20–105 16.4 ± 0.2	10 on top (wall) 5 in *x*/*y* 200 µm	25	215 Collector 70–90 80	6.2	0.5–1.0 0.5	25–150 750	3.3 ± 0.5	[90]
Electroactive polymers	PVDF	25–50	5	26	190 ± 2	2.70 ± 0.08	1.5–3.0	1800–5000	4.0 ± 0.5	[91]
Compounding particulates	3 and 7 wt% HAp in PCL	16.84 ± 2.41 20.46 ± 1.09	190 µm	21	80	7	20 mL h^{-1}	N/A	10	[47]
	Bioactive milk proteins in PCL	≈50 µm	5 300 µm	25 µm diameter	85	20	1	720		[29]
	5 wt% 45S5 BG in PLA-PEG-PLA/PLA 10 wt%	31 ± 2	10 5 in *x*/*y*	23	142	4	2	5000	3.5	[92]
	SrBG in PCL	≈100 µm	≈8–10 ≈4–5 in *x*/*y* 1000 µm	N/A	55	−6	3.8 0.69 0.36	N/A	8	[64]
	PEG and ROX in PCL	3–10	0°–90° pattern 15 100 µm pore size	45	95	2.3–2.6 kV	0.015–0.03	600–1200	1.5	[70]

Polyesters beyond PCL

While PCL is a polyester, this specific polymer has been described separately due to the substantial research already performed. Beyond pure PCL, Castilho and colleagues[84] blended a less hydrophobic material poly(hydroxymethylglycolide-*co*-*ε*-caprolactone) (pHMGCL) with PCL for cardiac tissue engineering processed using MEW. The hydroxyl-functionalized polyester pHMGCL has increased hydrophilicity compared to pure PCL,[93] and offers the possibility for further functionalization and tunable degradation rate.[84, 94]

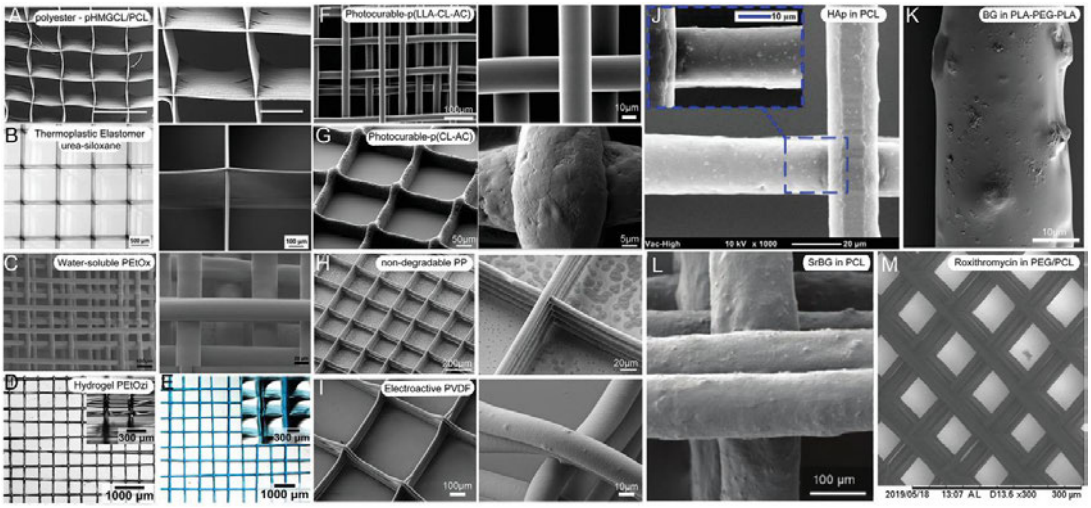

Figure 5. A–I) Scanning electron microscope (SEM) and microscope images of MEW-processed materials beyond PCL and J–M) compounded particulates within polymers to improve the polymer properties. A) MEW-processed polyester and B) printed thermoplastic elastomer with high printing accuracy similar to the gold-standard material PCL. C) A printed scaffold of water-soluble PEtOx and stereomicroscopic images of D) dry and E) swollen hydrogel PEtOzi scaffolds. SEM images of photocurable F) p(LLA-CL-AC) with smooth and uniform fiber surface and G) p(CL-AC) with rougher fiber surface morphology. Typical box-structure scaffold made of H) nondegradable PP and I) electroactive PVDF. PCL fibers including J) HAp particles and K) the fiber morphology of PLA-PEG-PLA blends including bioactive glass (BG) particles. L) PCL fibers with incorporated 33 wt.% strontium-substituted BG particles dissolved in chloroform and M) PCL-PEG scaffold loaded with roxithromycin enabling antibacterial and drug-release properties. A) Reprinted with permission.[84] Copyright 2017, Wiley-VCH GmbH. B) Reproduced with permission.[85] Copyright 2018, Wiley-VCH GmbH. C) Reproduced with permission.[86] Copyright 2014, the Authors. Published by Elsevier Ltd. D,E) Reproduced with permission.[87] Copyright 2020, The Royal Society of Chemistry. F) Reproduced with permission.[88] Copyright 2015, American Chemical Society. G) Reproduced with permission.[89] Copyright 2018, Elsevier Ltd. H) Reproduced with permission.[90] Copyright 2017, Elsevier B.V. I) Reproduced with permission.[91] Copyright 2018, Society of Chemical Industry. J) Reproduced with permission.[47] Copyright 2018, Elsevier Ltd. All rights reserved. K) Reproduced with permission.[92] Copyright 2017, the Authors. Published by Elsevier B.V. L) Reproduced with permission.[64] Copyright 2019, Wiley-VCH GmbH. M) Reproduced with permission.[70] Copyright 2019, Elsevier B.V. All rights reserved. Scale bar: (A) = 300 and 100 µm, respectively.

Furthermore, the blend showed enhanced biocompatibility and improved fiber architecture stimulating cell retention and guiding cardiac cell growth.[84] The printability of pHMGCL compared to PURAC PC-12 PCL, however, was reduced (Figure 5A).

Since PCL is ductile, more elastic materials for MEW have been synthesized to overcome this limitation. For example, the MEW processability of a thermoplastic elastomer (TPE) based on an $(AB)_n$-type segmented copolymer was studied.[85] This urea-siloxane copolymer consists of hard urea units in combination with soft PDMS segments to provide a combination of typical thermoplastic polymer properties and elastomers. Materials with thermoreversible physical crosslinks were processable with MEW resulting in scaffolds and fibers with elastomeric properties. Additionally, this material could be continuously processed for 14 h at a moderate processing temperature of 90 °C. The resulting poly(urea-siloxane) scaffolds printed with were especially well-stacked without fiber sagging at intersecting points at 50 layers (Figure 5B) resulting in stacking ability superior to the benchmark medical-grade PCL.[85]

Water-Soluble Polymers

Another class of materials are hydrophilic polymers, often used in medical and pharmaceutical applications. One class of these polymers is POx with adjustable macromolecular structure known to be biologically compatible and for the ability as a drug delivery system. Poly(2-ethyl-2-oxazoline) (PEtOx) is one type of POx with a high melting temperature between 200 and 220 °C demonstrated to be an excellent candidate for MEW as demonstrated in Figure 5C. Additionally, the sharp transition temperature for POx opens the possibility to design and adjust material properties during the polymer synthesis for thermoreversible behavior. This provides a tool for post-printing control through swelling,[87] as POx-based polymers can be synthesized to control water solubility in temperature ranges for cell viability or to control drug release.[86]

Hydrogel MEW Fibers

Another hydrophilic polymer synthesized for MEW is poly(2-ethyl-2-oxazine) (PEtOzi). This novel biomaterial ink spontaneously crosslinks via dynamic Diels–Alder click chemistry after processing as shown by Nahm and colleagues.[87] Therefore, the hydrogel can be MEW-processed into scaffolds, which are both soft and robust with thermoreversible hydrogel characteristics in dry and swollen state (Figure 5D,E). The successful fabricated hydrogel scaffolds can

be inserted into aqueous solutions and show temperature-dependent deswelling from 2 to 80 °C by 50% of the relative area. The robust mechanical properties allowed the scaffold to be repeatedly aspirated and ejected through a canula without any visible structural damage. These properties are highly desirable for injectable scaffolds, which can be direct-written into any essential micro structured design.[87]

Photocurable Polymers

Due to creep and the plasticizing effect of absorbed water when incorporating the fabricated constructs in an aqueous solution, the modulus of a swollen polymer can decrease.[95, 96] Therefore, synthesizing and processing a polymer, which can be post-crosslinked and thereby resisting the plasticizing effect in aqueous media could overcome this issue. On the basis of an already electrospun polymer poly(L-lactide-*co*-acryloyl carbonate) (poly(LLA-AC)),[95] which provided a high modulus in the hydrated scaffold after post-photocrosslinking, Chen and colleagues synthesized a poly(L-lactide-*co*-***ε***-caprolactone-*co*-acryloyl carbonate) (poly(LLA-***ε***-CL-AC)) polymer in an actual molar ratio of 60/31/9, which did slowly undergo premature crosslinking while melting.[88] However, the premature crosslinking was slow enough to enable MEW-processing of the poly(LLA-***ε***-CL-AC) polymer as shown in Figure 5F. The new synthesized polymer was prepared by mixing L-lactide (LLA), a trimethylene carbonate-based monomer (5-methyl-2-oxo-1,3-dioxan-5-yl acrylate, or acryloyl carbonate (AC)) and ***ε***-caprolactone (***ε***-CL). The ***ε***-CL was added to adjust the melting point required for MEW resulting in a melting onset temperature of 87 °C. Irgacure 651, a thermally stable crosslinking agent to temperatures up to 160 °C, was added to enable post-crosslinking of the MEW-processed scaffolds. The hydrated constructs showed an increased modulus and good stability after dynamic loading due to the successful post UV-irradiation at room temperature.[88]

Hochleitner and colleagues[89] investigated another photopolymerizable polymer, poly(***ε***-CL-AC). Compared to the previous investigated polymer poly(LLA-***ε***-CL-AC), poly(***ε***-CL-AC) showed considerably longer printing lifetime of up to 13 ± 7 h compared to 1.4 ± 0.7 h due to a remarkable slower crosslinking within the melt reservoir during MEW.[88, 89] Additionally, the melting onset temperature of the polymer was reduced to 55 °C due to the absence of lactide in the polymer. With this, poly(***ε***-CL-AC) resulted in a stable and controllable printing process with homogeneous and accurate fiber placement (Figure 5G). The post-printing UV-curing process improved the tensile strength and the Young´s modulus, as well as the elasticity and the creep resistance.[89] Therefore, the polymer was used to fabricate crimped patterns using sub-CTS deposition of sinusoidal fibers to mimic

tendon and ligament tissue as it is already shown that such morphologies are beneficial in generating fibroblast extracellular.[89, 97]

Nondegradable Polymers

Compared to the elastic properties given by the aforementioned polymers, some applications require mechanical strength and long-term stability of the scaffolds or implants. Therefore, another well-known material, PP, with a long-term stability in medical devices was tested for MEW to fabricate microscale fibers by Haigh and colleagues.[90] Using MEW to process PP offers the potential to fabricate small diameter fibers and constructs in an ordered manner (Figure 5H). However, compared to PCL and other MEW-processed materials, PP requires a high set temperature of 215 °C to be extrudable using MEW. Together with the high viscosity, a melt flow rate of 16 g min^{-1} (ISO1 133 230 °C/2.16 kg), the extruded PP does not adhere to the collector, which inhibits a stable jet. Using a heated collector, as shown by other extrusion-based techniques like FDM, enabled the fabrication of linear PP fibers and porous scaffolds.[90]

Electroactive Polymers

Another material family with remarkable properties, gaining more and more attention within the last years, are electroactive polymers (EAP). EAPs can generate electrical activity in response to deformations and are widely used in various electronic and biomedical applications.[98, 99] PVDF-based polymers are fluorinated electroactive materials, which are known for their remarkable ferroelectric and piezoelectric properties.[98] Compared to other piezoelectric materials such as lead zirconate titanate[100] or aluminum nitrite,[101] PVDF-based polymers are mechanically flexible[98] and mainly processed using SES.[102]

Florczak *et al*.[91] processed PVDF using MEW for the first time. A processing temperature of around 170 °C was needed and a voltage of around 2.70 kV was applied.[91] The fibers were uniform in shape, had diameters in the range from 17 to 55 µm, and showed sufficient coherence resulting in stable constructs. Scaffolds were fabricated with up to five alternating layers in 0° and 90° (Figure 5I), however, higher amounts of printed layers were not possible due to lifting of the scaffold edges while printing.[91] The MEW-processed polymer showed an increase in *β*-phase content to 79% compared to unprocessed material (49%) resulting in good piezoresponse with d_{33} values from 15.4 to 23.7 pm V^{-1}.[91] The fabrication of electroactive PVDF fibers with high control over the fiber placement and design offers promising potential for the use as sensors or actuators.[91]

Compounding Particulates

For in vivo applications of PCL it is advantageous that the biodegradability can be tailored, however, due to its hydrophobic properties, there is a limitation regarding the attachment of cells.[64, 103] Therefore, PCL can be modified by adding substitutes to design a PCL-based material with the desired properties.

Therefore, hydroxyapatite (HAp) particles were added to medical-grade PCL to enhance the bioactivity of MEW-fabricated PCL scaffolds for the application in mineralized tissue reconstruction.[47] The PCL/HAp composites showed good control over the fiber placement and high stacking ability (Figure 5J). The influence of the incorporated particles on the fiber diameter was studied and showed an increasing fiber diameter with increasing amount of HAp particles. The fiber morphology of the PCL/HAp fibers was slightly rougher compared to plain medical-grade PCL fibers and the HAp nanoparticles were uniformly distributed throughout the fibers. The resulting composite scaffolds induced higher cell growth of human osteoblasts cultured over 7 days and a significant acceleration in degradation rate compared to plain medical-grade scaffolds.[47] In general, the PCL/HAp composites offer a promising material for MEW-fabricated scaffolds for bone regeneration applications.[47]

Another approach to increase the bioactivity of MEW PCL scaffolds is demonstrated by Hewitt *et al*.[29] combining PCL with bioactive milk proteins, lactoferrin, and whey protein for skin regeneration. Printed scaffolds showed smooth and homogenous fibers.

Mixing and blending materials can easily improve limited or non-existing material properties, as well as broaden up the range of MEW-processable polymers. Therefore, Hochleitner and colleagues[92] used a poly(lactide-*block*-ethylene glycol-*block*-lactide) (PLA-PEG-PLA) triblock copolymer and blended it with low molecular weight PLA to lower the melting temperature of the degradable polymer. The PLA-PEG-PLA blend with 10 wt.% PLA showed promising printing results regarding the shape fidelity of the scaffolds and additionally, incorporating 5 wt.% solid 45S5 bioactive glass (BG) particles did not negatively influence the printability and processability (Figure 5K). This approach represents a promising novel material combination for bone tissue engineering and cell culture research.[92]

By adding strontium-substituted bioactive glass (SrBG) to PCL, Paxton and colleagues[64] were able to combine the beneficial properties of the bioactive SrBG with the good mechanical properties and the simple processability of PCL.[103, 104] With this approach, it was the first time that a PCL/SrBG composite was extruded and direct-written with a SrBG concentration of 33 wt.% demonstrated

in Figure 5L. However, this was only possible by dissolving the PCL/SrBG 33 wt.% composite in chloroform, an evaporable solvent, which reduced the viscosity of around 100 times and enabled MEW processability.[64] This study showed the advantage of combining a well-studied MEW-processable material with an additive resulting in the fabrication of direct-written scaffolds using a high-ceramic-content polymer.[64]

Another approach to combine different materials for the application in bone repair and regeneration is shown by adding PEG, as well as roxithromycin (ROX) to PCL resulting in smooth and homogenous fibers (Figure 5M).[70] Therefore, PEG and ROX increased the hydrophilicity of the processed material and enabled effective antibacterial properties while retaining cell viability and cell growth on the scaffolds. Additionally, the fabricated scaffolds featured an initial short-term burst release and subsequent long-term sustained antibiotic release behavior due to the added ROX.[70]

1.6 Hybrid Fabrication

One general approach to improve deficiencies in scaffold fabrication is to combine different manufacturing processes overcoming limitations in any single technology.

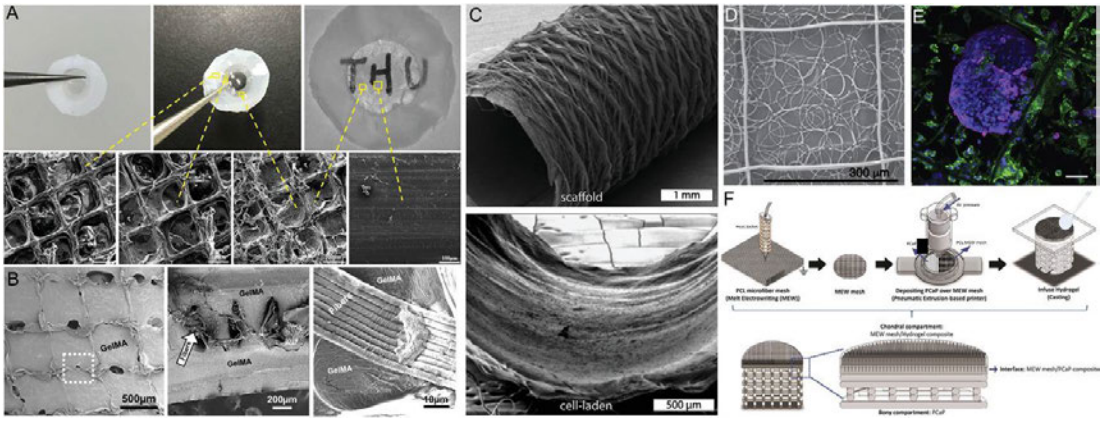

Figure 6. Various hybrid fabrication approaches of soft network composites embedding poly(ε-caprolactone) (PCL) fibers in A) PHEMA (core) and compressed collagen (skirt) as artificial cornea, and B) GelMA including amorphous magnesium phosphate (AMP). C) Combining different fabrication techniques like electrospinning and MEW resulting in bilayered tubular scaffolds and D) combining MEW and SES to design tight filters as E) on-site substrate of circulating tumor cells stained for cytokeratin (magenta), DNA (blue), and CD45 (green). F) A bone–cartilage interface design using MEW of GelMA reinforced PCL and extrusion-based printing of printable calcium phosphate (CaP). A) Reproduced with permission.[56] Copyright 2020, Elsevier Ltd. All rights reserved. B) Reproduced with permission.[72] Copyright 2020, Elsevier Ltd. All rights reserved. C) Reproduced with permission.[49] Copyright 2019, IOP Publishing Ltd. D,E) Reproduced with permission.[59] Copyright 2020, The Author(s). Published by Elsevier Ltd. F) Reproduced with permission.[52] Copyright 2020, The Author(s). Published by IOP Publishing Ltd. Scale bars: (B) = 100 µm and (F) = 50 µm.

Hybrid fabrication[105] and a detailed summary of hybrid developments using MEW are given by Afghah *et al*.[106] Using composite materials and techniques offers promising strategies to combine advantageous properties of different materials or techniques to one design approach (Figure 6).

Soft Network Composites

Soft network composites are the combination of MEW fibers and cast/bioprinted hydrogels. The synergistic mechanical reinforcement of MEW scaffolds with weak, cell-friendly hydrogels offers the possibility to mitigate limitations regarding biomechanical properties. This is one approach to shift the biofabrication window to softer hydrogels and matrices while retaining handling or biomechanical requirements.[35, 38, 42, 57]

Such composite approaches, reinforcing MEW-fabricated PCL scaffolds into hydrogels that include gelatin methacryloyl (GelMA), show promising results regarding the stiffness increasing by up to 54-fold.[42] In this fiber-reinforced composite study, embedded human chondrocytes showed good viability and retained their roundish morphology, showing compatibility in terms of stiffness and biological cues for cartilage applications.[42]

To further improve and investigate the reinforcement mechanism behind the composite PCL/GelMA structures, the composites were tested under axial compression to obtain more in detail insights into the deformation process, which can help further planning for designs of the embedded MEW scaffolds.[35] Agarwal *et al*.[57] also embedded PCL scaffolds within a polyvinyl alcohol (PVA) matrix resulting in hybrid films with improved mechanical stability. Finally, to provide 3D neuronal cell culture models with a weak matrix microenvironment closer to the native tissue, MEW fabricated scaffolds were embedded into Matrigel.[38, 41] Those reinforced scaffolds within the Matrigel improved the mechanical properties and therefore the handling of the delicate constructs.[38, 41]

Another approach to mimic native tissue and its composition was demonstrated by using orthogonal microfiber scaffolds embedded into compressed collagen to design an artificial cornea.[56] Furthermore, the PCL scaffold served as an interface between the compressed collagen and a PHEMA hydrogel resulting in a core-skirt design (Figure 6A).

To even further increase the stability of the hydrogel-fiber composites, out-of-plane fibers stabilized an existing MEW wall-like structure.[37] Those fibers were printed in sinusoids above the existing wall structure to specifically increase the

shear modulus. Those composite structures were designed to better withstand mechanical load that the matrix is subjected to once implanted in the body.[37]

Similar to the previous studies, the combination of a porous MEW mesh with a soft material allows flexibility regarding the mechanical properties and additionally, for further modification by doping the hydrogels with bioactive cues. Dubey *et al*.[72] upgraded a GelMA hydrogel with amorphous magnesium phosphate to improve the osteogenic ability of the reinforced constructs for guided bone regeneration, shown in Figure 6B.

Combining Electrospinning with MEW

Combining different fiber orientations, diameters or even different fabrication techniques can improve the outcome of the design regarding the mechanical properties or the hierarchical design. Especially SES or MES with MEW is more frequently combined for different approaches.

Therefore, Zhang *et al*.[60] used SES to fabricate aligned PCL nanofibrous meshes, which were coated with gold in different thicknesses to introduce electroactive cues to the nanoscale PCL meshes. MEW was used to direct-write microgrooves, also made of PCL on top of the coated meshes. Those hierarchically organized scaffolds were fabricated to investigate the influence of the nano- and microfibers in combination with the electroactive cues on myotube guidance for skeletal muscle regeneration.[60] Furthermore, the hierarchically hybrid scaffolds were rolled up to form fascicle mimicking the native bundles of parallel aligned myofibers within skeletal muscles.[60]

A hierarchically bilayered tubular scaffold was fabricated by combining the two techniques SES and MEW.[48] The inner SES layer enabled a dense fiber mesh with randomly oriented nanofibers and the outer layer was fabricated using MEW to control the microfiber placement and orientation. The tubular scaffold showed promising results directing the cell morphology and differentiation, as well as mimicking the intimal and medial layers of native vessels.[48] To further improve this approach, Pennings *et al*.[49] developed a bioreactor system for the coculture of endothelial colony forming cells and multipotent mesenchymal stromal cells within the hybrid tubular scaffolds described previously (Figure 6C).[48] The bioreactor induced simultaneous layer-specific cell differentiation under shear stress. These studies showed promising results for bioengineered vascular grafts, particularly, mimicking the tunica intima and media.[48, 49]

Hybrid scaffolds fabricated using the combination of SES and MEW can also be used for applications in cancer treatment.[59] The scaffolds made of non-medical-

grade PCL were designed as a filter to catch circulating tumor cells within the blood, as well as the culture substrate directly on site (Figure 6D,E).[59] For the filters, different solvents were used to fabricate coiled fiber arrays by SES and on top of those tight membranes, MEW-processed fibers were printed as a frame in the shape of typical box structures to stabilize the constructs.[59]

One strength of MEW is its solvent-free perspective, and therefore combining with SES diminishes this standpoint. Recently, MES nanofibers with a diameter as small as 275 nm were generated by inserting an acupuncture nozzle in a nozzle.[107] In this way, medical-grade PCL could be used to produce nanofibers that are of such interest for biomedical engineers. This study additionally combined this MES nozzle with MEW using a dual-head printer, where electrospinning formed a thin barrier of nonwoven fibers and could be subsequently direct-written upon. Therefore, a nanoscale/microscale product could be generated using GMP-manufactured polymer on a single printer without the use of solvents.[107]

Combining Extrusion-Based 3D Bioprinting with MEW

Soft network composites showed promising results regarding the adaptable mechanical properties and the handling of the samples. Additionally, the hydrogel can provide an improved biological environment for cells.[35, 37, 38, 41, 42] However, embedding the MEW scaffold into a gel prevents an accurate and controlled placement of the cells within the constructs. Therefore, de Ruijter *et al*.[43] used a simultaneous micropatterning approach by combining extrusion-based bioprinting and MEW. 3D bioprinting enabled the accurate and controlled placement of the cell-laden hydrogel and allowed the fabrication of more complex organized cellular structures by converging this technique with MEW.[43] GelMA including fluorescent dyes labeled equine-derived mesenchymal stromal cells was printed into the pores of the medical-grade PCL scaffold and the biological tolerance was demonstrated. This converged one-step printing approach offers improved freedom in design and a defined control over cell deposition within the MEW scaffold.[43]

Diloksumpan *et al*.[52] used an extrusion-based printer in combination with MEW to engineer a bone–cartilage interface. The hierarchically organized construct consisted of a bioceramic part of printable CaP-based ink, which was deposited onto a MEW scaffold made of medical-grade PCL to directly anchor the two components. To further mimic the chondral component, the MEW scaffold was embedded in GelMA,[52] as shown in Figure 6F.

1.7 Future Perspectives for MEW Printers

While the future of MEW may partly be an essential additional head for a bioprinter, there are several reasons to pursue research-line, standalone devices. Both commercial and custom-built MEW printers are available, with over 95% of MEW publications coming from the latter. Custom-built systems allow specialized MEW-processing research and provide indicators of required properties for any future MEW head. There are several different concept MEW printers described, for research perspectives such as *Printomics*[108] as well as scale-up systems.

Collectors

Beyond a flat collector substrate, a cylindrical collector has been demonstrated for MEW.[24, 25, 48, 49, 53, 109, 110] When calculating the printing path, a current limitation of MEW is not being readily able to stop/start the jet. Therefore, a tubular shape such as shown in Figure 7A requires some mathematical calculations to generate the appropriate G-codes for winding/translation.[24, 109]

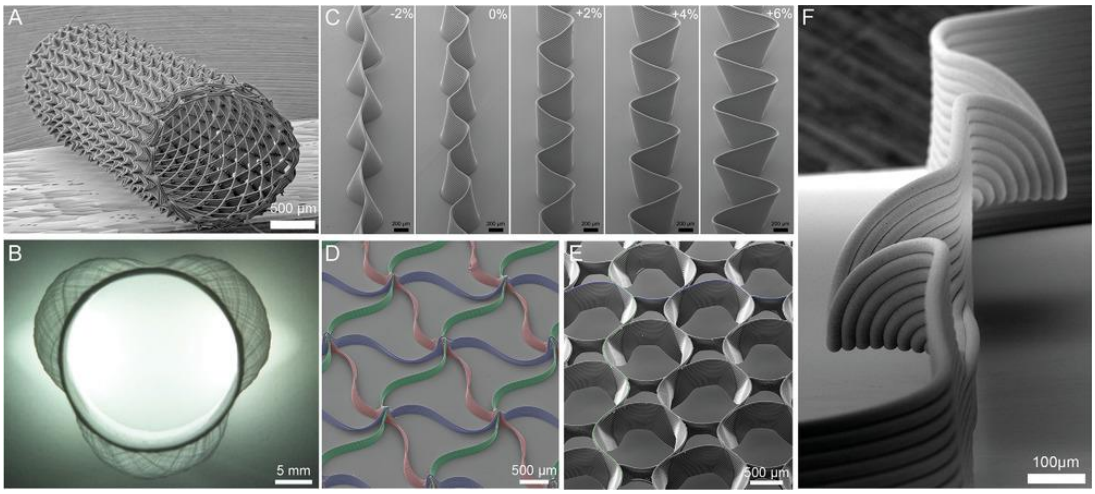

Figure 7. SEM images of melt electrowritten scaffold designs using medical-grade PCL: Different complex architectures include A) tubular constructs, including B) anatomically relevant tubes such as the aortic root model, C–F) microscale layer shifting and tilting due to increasing amplitudes resulting in fiber walls, triangle-shaped pores, circular pores, and horizontal fibers. A) Reproduced with permission.[24] Copyright 2018 The Authors. Published by Elsevier Ltd. B) Reproduced under the terms of the Creative Common CC-BY license.[54] Copyright 2020, the Authors. Published by Frontiers Media S.A. C–F) Reproduced under the terms of the Creative Common CC-BY license.[23] Copyright 2020, the Authors. Published by Wiley-VCH GmbH.

An open-access web-based application “MEWTubes” allows such design of the tubes with different pore size, winding angle, and the lengths of translation, described in detail by McColl *et al*.[24] Similar to when performing MEW on flat

collectors, the laydown pattern has a clear influence on the mechanical properties of the fabricated structures[24, 109] and can result in auxetic tubular scaffolds.[25]

As previously discussed, the collector and its properties have a significant role for MEW to enable polymer processability and to fabricate constructs with accurate fiber placement even on tubular collectors. Since MEW is based on the EHD principle stabilizing the polymer jet[6] and therefore enabling the fabrication of fibers in the micrometer range due to a constant electrical field,[50] it also limits the fabrication of uniform fibers onto more complex, nonuniform collectors.[54, 55] This technical boundary is due to the interaction of the collector with the EHD working principle leading to jet instabilities and limiting the accurate fiber placement.[54, 55] One approach to overcome these limitations is shown by using a hybrid collector consisting of an aluminum (Al) mandrel in combination with a 3D-printed PLA tube.[54] Compared to a full Al mandrel and a full conductive combination of Al and titanium, the Al-PLA setup enabled a consistent electrical field strength. Using the double-component collector consisting of a conductive and a nonconductive material combination, the PLA part collected the deposited fibers without causing electrical field disruptions and furthermore, enabled to possibility to fabricate patient-specific designs due to the advantage of being 3D printed (Figure 7B).[54] Using this collector approach, the fabrication of an aortic wall including three aortic sinuses was possible and proved that MEW can be used to fabricate nonuniform complex designs.[54]

Another approach to print medical-grade PCL in anatomical relevant structures with non-flat (wedge- and curved-shaped) geometries was demonstrated with different collector substrates for nonconductive materials like magnesium phosphate (MgP) and PCL, as well as on conductive materials like GelMA and Al.[55] Comparing the different collector substrates, the conductive materials did result in bigger fiber diameters and higher scaffolds, as well as, for the first layer, a more flattened (ellipsoidal) fiber shape. Using computational stimulations, it was possible to relate these findings to a higher electrical field strength for conductive collecting materials compared to the nonconductive materials.[55] Furthermore, fiber deposition with high accuracy onto non-flat collectors was possible with a z-correction in the printhead trajectory keeping the distance between the collector and the printhead, as well as the electrical field strength constant.[55]

The accuracy of MEW is also dependent on the stage quality, especially the axis precision.[90] Additionally, remaining charges as well as electrostatic attraction of the fibers is restricting the design and the result of MEW-processed constructs. Therefore, understanding the principle of the jet formation, the influences on it and

by controlling the jet lag for each layer while printing, inaccuracies can be corrected enabling control over fiber placement and horizontal layer stacking.[23] Medical-grade PCL has been processed into complex structures with overhangs, wall texturing, and branching by introducing vertical layer shifting (Figure 7C,F).[23] Using those approaches, mechanical properties can be tailored by changing the scaffold design introduced by microscale layer shifting and furthermore, opening a new possibility to even more complex constructs.[23] Such shifts in printing path are as low as 6 µm, therefore stages are required that can deliver such precision.

Delivery of Melt to the Nozzle

Some of the first MEW printers used a piston attached to a syringe pump to control the melt flow to the nozzle.[5, 14] More recently, air (or nitrogen) pressure has been used for pressurizing the syringe for melt flow with improved startup times. Furthermore, the use of digitally controlled pressure valves allows controlled alteration of air pressure, resulting in the capability to change the fiber diameter “on the fly” during a print. It is notable that there are instances when a higher pressure (than 5 bar) is required to achieve extrusion to the nozzle,[64] or lower pressures are needed to obtain small diameter fibers for MEW.[11]

Using the pressure to control fiber diameter, Hrynevich *et al*.[11] showed how variable diameters can be generated in a single print, through controlling the collector speed and applied pressure. The fabricated PCL scaffolds were adapted for spheroid seeding to develop a sheet-like tissue scaffold including multicellular spheroids. The design was based on the typical box-structured scaffolds, but included two 7 µm diameter catching fibers close to the bottom of the scaffold, to prevent spheroids passing through during seeding and cultivation.[11, 40] This tissue-sheet construct enabled simultaneous high spheroid seeding efficiency with ease of handling, high cell viability, and successful differentiation of the spheroids.[40]

Thermal Requirements

When considering polymers beyond PCL, an increased operation temperature is one significant area that is a prerequisite for many of the polymers highlighted in Table 2 and Figure 5. Melt processing temperatures above 100 °C are commonplace in other technologies and there are important engineering polymers that require processing at 200 °C and higher. There are three general approaches for heating the MEW/MES jet: 1) electrical, 2) circulating fluids/air (Figure 8A), and

3) infrared lasers. Both circulating air and infrared lasers have advantages in both upper temperature limits achievable and speed of jet initiation.[111] The most common approach, however, is the electrical heater (Figure 8B), designed to be isolated from the high voltage supply.

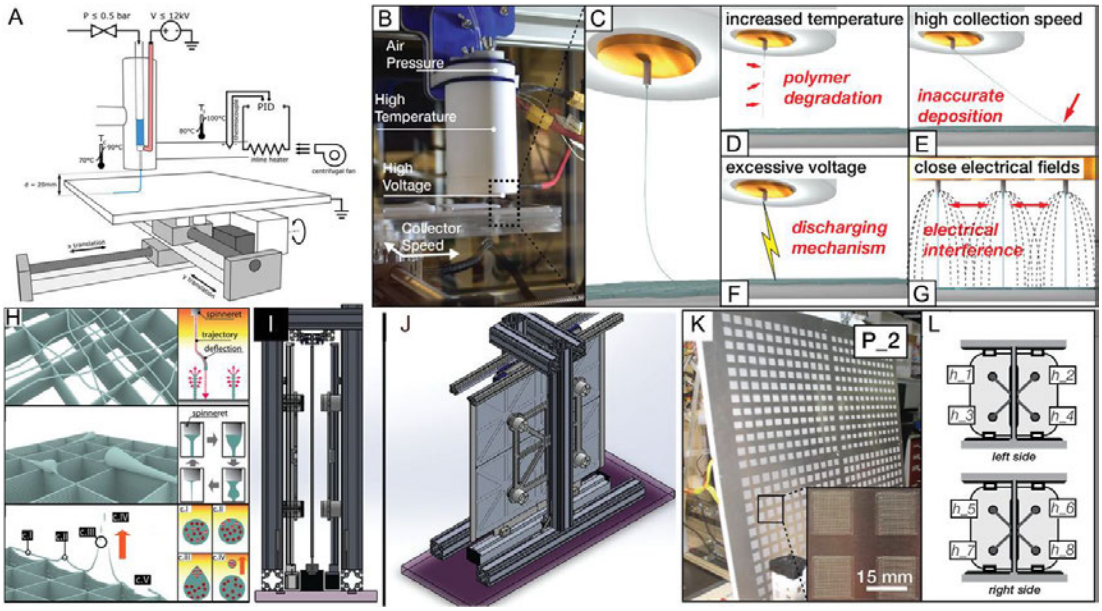

Figure 8. Overview of MEW printers. A) Schematic illustration of a MEW printer using an industrial heat gun as hot air stream supply, heating the polymer melt while the jet remains in ambient temperature conditions. B) Images of typical single material MEW head and C) the resulting polymer jet. There are limitations during fiber generation resulting from D) polymer degradation due to high temperatures, E) high printing speeds resulting in inaccurate fiber deposition, F) excessive voltage causing arcing, and G) electrical interference between close electrical fields. H) Schematic of fiber printing defects as increased build height due to electrostatic repulsion and/or attraction of the polymer melt, fiber pulsing, or fiber attraction toward the nozzle. I–J) CAD models showing different views of the high-throughput MEW printer using eight simultaneous printheads extruding onto a vertical collector. K) Images of one side of the vertical collector with 576 scaffolds and L) the labeling of the eight printheads on both, the left and right side. A) Reproduced with permission.[21] Copyright 2018, Elsevier Ltd. All rights reserved. B–G) Reproduced with permission.[44] Copyright 2019, Mary Ann Liebert, Inc., publishers. H) Reproduced with permission.[50] Copyright 2018, Wiley-VCH GmbH. I–L) Reproduced with permission.[44] Copyright 2019, Mary Ann Liebert, Inc.

Alternatively, a high voltage can be applied to the collector and the heating nozzle grounded. The implications of such voltage configurations on the fiber diameter, stacking, pulsing, and the CTS are still not fully elucidated.

Similar to FDM, MEW extrudes a polymer melt through a small nozzle generating layer-by-layer constructs with partially fiber fusion. However, the cooling down of the polymer within a specific shape can cause internal stresses leading to deformations (called warping) especially in corners.[112] Furthermore, when a substantial temperature difference between the nozzle and the ambient air is used,

build plate adhesion issues are commonplace for FDM printing and can result in poor fiber adhesion to the collector. To overcome this issue, a heated collector has been shown to be necessary to achieve fiber collection. When processing PP with a nozzle temperature of 215 °C, for example, a heated collector of 70 °C is needed for adhesion of the fibers.[90] Ideally, controlling all aspects of the heating profile including nozzle, syringe, ambient temperatures, and heated collector would ensure control over jet processing, fiber adhesion, and fiber–fiber adhesion with the latter, having a substantial influence on the mechanical properties of the printed material. While an ideal ambient humidity of 25–45% r.h. at room temperature allows sample consistency, this level can be affected by seasonal changes.

Dynamic Electric Fields

MEW-processed scaffolds are quite limited in thickness and volume when static collector distances and voltages are used, due to residual charges within the printed fibers that remain with increasing build height similar to the principles previously discussed for nonuniform collectors. Wunner and colleagues[50] investigated the underlying physical principles to overcome the current limitation regarding the thickness of the scaffolds, and identified a solution to attain thick (7 mm) MEW scaffolds. Since MEW requires an electrical field to form a stable jet, using a fixed voltage and collector distance between the printhead and the translating collector results in several complications. The resulting scaffolds are limited in the accurate fiber placement with increasing height due to the accumulation of excess charge (Figure 8H). These charges remaining in the deposited fibers result in attraction of the fibers back to the heated head and distorting of the scaffold architectures.[50] Maintaining the electrostatic force at a constant level during the print by an adjustable working distance between collector and printhead, and an increase of the voltage, a scaffold with a height of 7 mm was fabricated.[50] MEW printers therefore require the ability to digitally adjust both the collector distance and applied voltage to obtain thicker scaffolds.

Imaging and Visualization: Toward Digitization

While different AM technologies have their strengths and weaknesses, MEW has extremely good advantageous visual access to important monitoring information. While real-time visual information from electron beam melting, stereolithography, or even FDM is of limited value, the MEW nozzle raised several millimeters above the collector provides an excellent view of the electrified jet. This information including jet angle provides process stability information and is relatively simple to collect with

digital cameras (Figure 1A).[108] Such camera information and its subsequent digital processing was used to describe *Printomics*, the analysis of MEW printing parameters, through digital control and processing.[108] In this concept MEW printer, an inexpensive USB camera combined with a simple objective microscope was used to provide the jet angle and fiber diameter information, respectively. The lag in the jet is especially important for predictive fiber placement. Jin *et al*.[71] further established a model based on a reversed speed planning process to compensate the lag effect, which limits the accurate fiber placement depending on the printing speed using a high molecular weight PCL.

Scale-Up Systems

An increasing number of AM technologies are used to fabricate 3D scaffolds for cell culture experiments especially for the application in tissue engineering and regenerative medicine. MEW, therefore, was used to produce scaffolds for researchers consisting of ordered fibers with micrometer size in diameter. However, scale-up productions, which are necessary to effectively translate to industrial applications, are only commencing[44] and require uniform jet formation across different nozzles. Figure 8I–L shows a MEW system including eight simultaneously extruding printheads, which enabled to fabricate large-scale structures based on printing parameters given from a single-head system.[44] Scaffolds with identical morphologies and fiber diameters were successfully fabricated in dimensions up to 78 × 78 cm.[44] To establish a MEW printer ecosystem, which can be easily upscaled, the collector of the system was transferred to the vertical mounting.[44] Previous research by Wunner *et al*.[45] demonstrated the possibility to perform MEW printing from all directions (horizontal, lateral, and upside down) without affecting the fiber jet.[44, 45]

Future Perspectives for Processable Materials

Exploring the compatibility of new polymers with MEW has only recently commenced, and improvements in printer designs and expansion into applications beyond biomedical will enhance this perspective. The capability of MEW printers is inextricably linked to exploring new polymers, however, based on our fundamental understanding of jet instabilities, it is possible to look forward and identify the properties of fluids that will be compatible with the process.

Fundamentally, fluid columns exist under many circumstances; a simple example is when water comes out of a faucet.[113] With unlimited space to fall, such a contiguous fluid column eventually breaks due to Plateau–Rayleigh instabilities

(Figure 9A), where perturbations in the fluid column result in the formation of a discontinuous phase (Figure 9B).[114] Important and well-known considerations that influence when this fluid break up include the flow rate, the shape of the outlet, and the viscosity of the fluid used.[113, 115] When these fluids land on a solid collector, they buckle and form patterns depending on various parameters (Figure 9C–E).[115, 116]

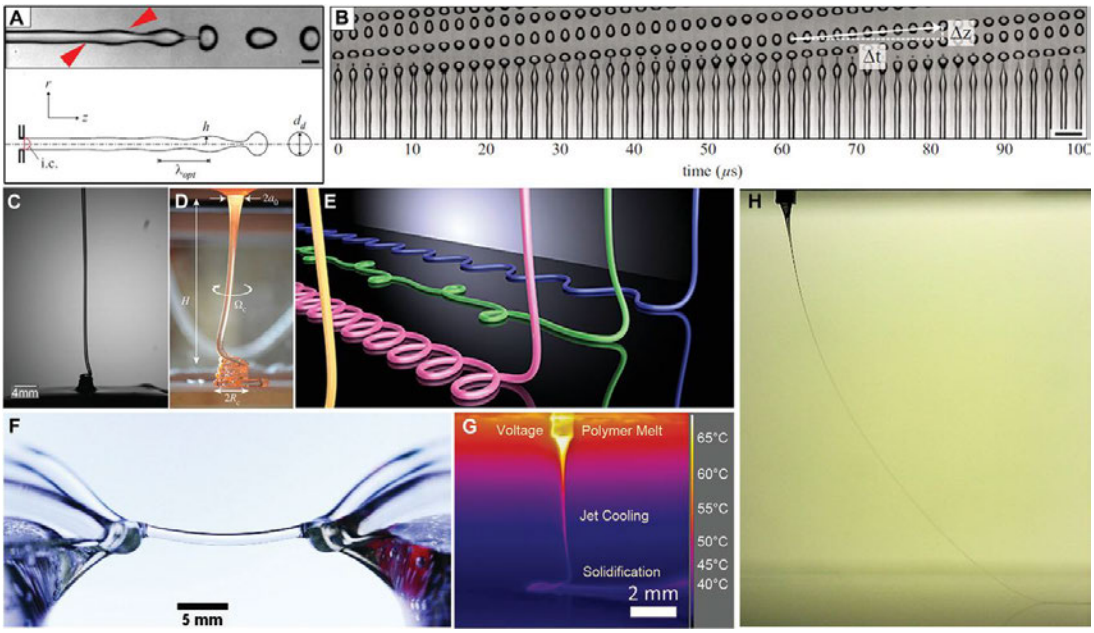

Figure 9. Fluid jets and their breakup or stabilization. A) Photograph and schematic of a water jet that undergoes perturbations (red arrow) as part of Plateau–Rayleigh instabilities and prior to jet breakup. B) Photograph of 49 jets at different stages of Plateau–Rayleigh instabilities. Photographs of "liquid rope" coiling of C) honey and D) molten glass landing on a static collector with E) showing a render of how such fluid columns buckle and land when direct-written. Photograph of F) a floating water bridge, where deionized water is suspended between two beakers using the application of a voltage, and G) from an infrared camera of a PCL MEW jet landing on a stationary collector and H) a photograph of a MEW jet, showing how the applied voltage can prevent this jet from undergoing Plateau–Rayleigh instabilities, even at low flow rates. A,B) Reproduced with permission.[114] Copyright 2010, AIP Publishing. C) Reproduced under the terms of the Creative Commons Agreement 4.0 (CC BY).[117] Copyright 2018, the Authors. Published by MDPI. D) Reproduced with permission.[116] Copyright 2017, The Royal Society. E) Reprinted figure with permission.[115] Copyright 2015, American Physical Society. F) Reproduced with permission.[118] Copyright 2010, AIP Publishing. G) Previously unpublished image provided by Mr. Andrei Hrynevich. H) Reproduced with permission.[108] Copyright 2019, IOP Publishing.

It is lesser known that applying a potential difference across this fluid column can suppress the Plateau–Rayleigh instabilities. Figure 9D shows how a column of deionized water can be horizontally suspended in mid-air through the application of a voltage. This floating water bridge shows that charged species at the surface of the fluid column prevents local perturbations and therefore suppress fluid

breakup.[118] This EHD effect was also shown by Sir Geoffrey Taylor in the 1960s[7] and is described in detail elsewhere in the context of MEW.[6] This is distinct to electrospraying water where the voltage is increased to such a high level that surface charges overcome surface tension.[119] It is these two EHD effects that resulted in the distinction between MES (where electrical instabilities in the jet are deliberately initiated) and MEW (Figure 9G). Once a fluid column is stabilized by a voltage, it can persist at low flow rates (Figure 9H) depending on the fluid properties.

When selecting a fluid to use for direct-writing jetting in general, much can be learned from our understanding how noncharged fluid columns behave (Figure 9C,D). As previously mentioned, the flow rate to the nozzle is a significant indicator of whether a contiguous column is formed, as is the height of release. Higher flow rates can establish a fluid column, however of greater importance to the additive manufacturing community are smaller diameter fibers that result from low flow rates. Research on Plateau–Rayleigh instabilities is often performed with water/glycerol blends, where the viscosity can be substantially increased with minimal changes in surface tension.[113]

Certain fluids form contiguous columns at low flow rates, for example, honey, treacle, and certain oils.[120] Central to all of these materials are long polymer chains that result in macromolecular entanglement, which is also a commonality in all MEW-processed polymers to date. The localized increased viscosity on the jet (which also increases during cooling) minimizes jet perturbations, especially at low flow rates. For MEW to achieve a small fiber diameter, an especially low flow rate is required—measured at 2.6 µL h^{-1} for 2–3 µm diameter fibers.[107] Therefore, low viscosity fluids are difficult to MEW process unless increased flow rates (and therefore diameters) are adopted.

The use of heat for MEW processing can also affect the fluid properties, both physical and chemical. The residency of a polymer at elevated temperatures is amplified by the need for low flow rates to achieve small diameter fibers. The heat applied to the melt can have 1) no effect on the melt, 2) initiate crosslinking, or 3) cause thermal degradation, depending on the chemical nature of the polymer used, and the level of heat required to achieve molten flow through the nozzle. For biologically derived polymers, denaturation[121] is an issue that needs to be overcome or avoided in future printing iterations.

The quantity of charged species within the polymer melt will also affect the printing properties of the polymer. As certain classes such as conductive polymers are MEW-processed, the printer configurations are expected to change accordingly. Also observed with noncharged fluid columns, the diameter of the nozzle affects the

resulting thinning of the jet—this effect was also observed in a previous MES paper.[122]

Understanding Plateau–Raleigh instabilities will enhance the selection of new polymers for MEW and excellent research studies and reviews on this phenomenon are found elsewhere. It is important to appreciate that, unlike electrospinning, MEW uses the applied voltage to stabilize the jet and to prevent it from breaking up droplets as known from noncharged falling fluids.[6, 7] In combination with the significant lower flow rates and the smaller distance between collector and nozzle, it is essential that Plateau–Raleigh instabilities are prevented so that controlled direct-writing can be achieved.[6]

Since the EHD effect of preventing fluid column breakup is general to fluids, it is expected that many fluids will work in this manner, although the lower dimensions achieved will be dependent on their macromolecular interactions. The minimum operating temperature is also crucial, as this affects the degradation profile (if any) and is one reason why the development of new polymers needs to go hand-in-hand with improvements to MEW printers. The temperature is important when delivering highly viscous fluids through small diameter nozzles can therefore pose problems in achieving certain flow rates. It is expected that over the next five to ten years, however, researchers will dramatically expand the number of polymers processable and enhance their specific properties with some of the design possibilities also outlined here.

1.8 Conclusion

While the vast majority of publications on MEW research use PCL, there is a growing number of studies demonstrating that many other polymers can be processed with this technique. Keeping in line with a biomedical application perspective, most other studies are performed with various chemical permutations of hydrolytically degradable polyesters. Furthermore, surface coatings of fabricated fibers and compounding additives into the melt phase are two strategies used to impart further function into the final printed structure. Beyond biomedical applications, other fields such as microfluidics,[80] optic guides,[123] or pressure sensors[124] are taking advantage of this high-resolution AM technology. Expanding the number of processable polymers for MEW will also require improvements to current printers, which can lack the added features that aid in this type of processing. However, based on the current trends and the general interest in EHD-assisted AM, we expect many more polymers will be processed via MEW.

1.9 Acknowledgements

Proofreading by Dr. Biranche Tandon is greatly appreciated. This work was supported by funding from the Volkswagen Stiftung (Grant No. 93417). Open access funding enabled and organized by Projekt DEAL.

1.10 References

[1] J. Henkel, J. T. Schantz, D. W. Hutmacher, Osteologie 2013, 22, 180.

[2] M. Mao, J. He, X. Li, B. Zhang, Q. Lei, Y. Liu, D. Li, Micromachines 2017, 8, 113.

[3] D. W. Hutmacher, T. B. F. Woodfield, P. D. Dalton, in Tissue Engineering (Eds: C. van Blitterswijk, J. De Boer), Elsevier, Amsterdam 2014, p. 311.

[4] T. D. Brown, F. Edin, N. Detta, A. D. Skelton, D. W. Hutmacher, P. D. Dalton, Mater. Sci. Eng., C 2014, 45, 698.

[5] T. D. Brown, P. D. Dalton, D. W. Hutmacher, Adv. Mater. 2011, 23, 5651.

[6] P. D. Dalton, Curr. Opin. Biomed. Eng. 2017, 2, 49.

[7] G. I. Taylor, M. D. Van Dyke, Proc. R. Soc. London, Ser. A 1969, 313, 453.

[8] D. H. Reneker, A. L. Yarin, Polymer 2008, 49, 2387.

[9] a) A. L. Yarin, S. Koombhongse, D. H. Reneker, J. Appl. Phys. 2001, 90, 4836; b) A. Vaseashta, Appl. Phys. Lett. 2007, 90, 093115.

[10] a) T. Han, D. H. Reneker, A. L. Yarin, Polymer 2007, 48, 6064; b) Y. M. Shin, M. M. Hohman, M. P. Brenner, G. C. Rutledge, Appl. Phys. Lett. 2001, 78, 1149; c) S. V. Fridrikh, J. H. Yu, M. P. Brenner, G. C. Rutledge, Phys. Rev. Lett. 2003, 90, 144502.

[11] A. Hrynevich, B. ¸S. Elçi, J. N. Haigh, R. McMaster, A. Youssef, C. Blum, T. Blunk, G. Hochleitner, J. Groll, P. D. Dalton, Small 2018, 14, 1800232.

[12] A. Youssef, A. Hrynevich, L. Fladeland, A. Balles, J. Groll, P. D. Dalton, S. Zabler, Tissue Eng., Part C 2019, 25, 367.

[13] G. Hochleitner, T. Jüngst, T. D. Brown, K. Hahn, C. Moseke, F. Jakob, P. D. Dalton, J. Groll, Biofabrication 2015, 7, 035002.

[14] B. L. Farrugia, T. D. Brown, Z. Upton, D. W. Hutmacher, P. D. Dalton, T. R. Dargaville, Biofabrication 2013, 5, 025001.

[15] C. Mota, D. Puppi, M. Gazzarri, P. Bártolo, F. Chiellini, Polym. Int. 2013, 62, 893.

[16] G. Hochleitner, A. Youssef, A. Hrynevich, J. N. Haigh, T. Jungst, J. Groll, P. D. Dalton, BioNanoMaterials 2016, 17, 159.

[17] N. C. Paxton, M. Lanaro, A. Bo, N. Crooks, M. T. Ross, N. Green, K. Tetsworth, M. C. Allenby, Y. Gu, C. S. Wong, S. K. Powell, M. A. Woodruff, J. Mech. Behav. Biomed. Mater. 2020, 105, 103695.

[18] T. M. Robinson, D. W. Hutmacher, P. D. Dalton, Adv. Funct. Mater. 2019, 29, 1904664.

[19] M. J. Blount, J. R. Lister, J. Fluid Mech. 2011, 674, 489.

[20] A. Fuchs, A. Youssef, A. Seher, G. Hochleitner, P. D. Dalton, S. Hartmann, R. C. Brands, U. D. A. Müller-Richter, C. Linz, BMC Oral Health 2019, 19, 28.

[21] K. F. Eichholz, D. A. Hoey, Acta Biomater. 2018, 75, 140.
[22] T. Tylek, C. Blum, A. Hrynevich, K. Schlegelmilch, T. Schilling, P. D. Dalton, J. Groll, Biofabrication 2020, 12, 025007.
[23] I. Liashenko, A. Hrynevich, P. D. Dalton, Adv. Mater. 2020, 32, 2001874.
[24] E. McColl, J. Groll, T. Jungst, P. D. Dalton, Mater. Des. 2018, 155, 46.
[25] N. C. Paxton, R. Daley, D. P. Forrestal, M. C. Allenby, M. A. Woodruff, Mater. Des. 2020, 193, 108787.
[26] N. T. Saidy, F. Wolf, O. Bas, H. Keijdener, D. W. Hutmacher, P. Mela, E. M. De-Juan-Pardo, Small 2019, 15, 1900873
[27] A. Charuchinda, R. Molloy, J. Siripitayananon, N. Molloy, M. Sriyai, Polym. Int. 2003, 52, 1175.
[28] D. Mondal, M. Griffith, S. S. Venkatraman, Int. J. Polym. Mater. Polym. Biomater. 2016, 65, 255.
[29] E. Hewitt, S. Mros, M. McConnell, J. Cabral, A. Ali, Biomed. Mater. 2019, 14, 055013.
[30] M. Bartnikowski, T. R. Dargaville, S. Ivanovski, D. W. Hutmacher, Prog. Polym. Sci. 2019, 96, 1.
[31] N. Abbasi, A. Abdal-hay, S. Hamlet, E. Graham, S. Ivanovski, ACS Biomater. Sci. Eng. 2019, 5, 3448.
[32] O. Bas, D. D'Angella, J. G. Baldwin, N. J. Castro, F. M. Wunner, N. T. Saidy, S. Kollmannsberger, A. Reali, E. Rank, E. M. De-Juan-Pardo, D. W. Hutmacher, ACS Appl. Mater. Interfaces 2017, 9, 29430.
[33] S. Bertlein, G. Hochleitner, M. Schmitz, J. Tessmar, M. Raghunath, P. D. Dalton, J. Groll, Adv. Healthcare Mater. 2019, 8, 1801544.
[34] C. Blum, K. Schlegelmilch, T. Schilling, A. Shridhar, M. Rudert, F. Jakob, P. D. Dalton, T. Blunk, L. E. Flynn, J. Groll, ACS Biomater. Sci. Eng. 2019, 5, 6655.
[35] M. Castilho, G. Hochleitner, W. Wilson, B. van Rietbergen, P. D. Dalton, J. Groll, J. Malda, K. Ito, Sci. Rep. 2018, 8, 1245.
[36] M. Castilho, A. van Mil, M. Maher, C. H. G. Metz, G. Hochleitner, J. Groll, P. A. Doevendans, K. Ito, J. P. G. Sluijter, J. Malda, Adv. Funct. Mater. 2018, 28, 1803151.
[37] M. de Ruijter, A. Hrynevich, J. N. Haigh, G. Hochleitner, M. Castilho, J. Groll, J. Malda, P. D. Dalton, Small 2018, 14, 1702773.
[38] D. Janzen, E. Bakirci, A. Wieland, C. Martin, P. D. Dalton, C. Villmann, Adv. Healthcare Mater. 2020, 9, 1901630.
[39] F. Kotz, P. Risch, K. Arnold, S. Sevim, J. Puigmartí-Luis, A. Quick, M. Thiel, A. Hrynevich, P. D. Dalton, D. Helmer, B. E. Rapp, Nat. Commun. 2019, 10, 1439.

[40] R. McMaster, C. Hoefner, A. Hrynevich, C. Blum, M. Wiesner, K. Wittmann, T. R. Dargaville, P. Bauer-Kreisel, J. Groll, P. D. Dalton, T. Blunk, Adv. Healthcare Mater. 2019, 8, 1801326.

[41] N. Schaefer, D. Janzen, E. Bakirci, A. Hrynevich, P. D. Dalton, C. Villmann, Adv. Healthcare Mater. 2019, 8, 1801226.

[42] J. Visser, F. P. W. Melchels, J. E. Jeon, E. M. van Bussel, L. S. Kimpton, H. M. Byrne, W. J. A. Dhert, P. D. Dalton, D. W. Hutmacher, J. Malda, Nat. Commun. 2015, 6, 6933.

[43] M. de Ruijter, A. Ribeiro, I. Dokter, M. Castilho, J. Malda, Adv. Healthcare Mater. 2019, 8, 1800418.

[44] F. M. Wunner, S. Eggert, J. Maartens, O. Bas, P. D. Dalton, E. M. De-Juan-Pardo, D. W. Hutmacher, 3D Print. Addit. Manuf. 2019, 6, 82.

[45] F. M. Wunner, J. Maartens, O. Bas, K. Gottschalk, E. M. De-JuanPardo, D. W. Hutmacher, Mater. Lett. 2018, 216, 114.

[46] M. Gwiazda, S. Kumar, W. Swieszkowski, S. Ivanovski, C. Vaquette, J. Mech. Behav. Biomed. Mater. 2020, 104, 103631.

[47] A. Abdal-hay, N. Abbasi, M. Gwiazda, S. Hamlet, S. Ivanovski, Eur. Polym. J. 2018, 105, 257.

[48] T. Jungst, I. Pennings, M. Schmitz, A. J. W. P. Rosenberg, J. Groll, D. Gawlitta, Adv. Funct. Mater. 2019, 29, 1905987.

[49] I. Pennings, E. E. van Haaften, T. Jungst, J. A. Bulsink, A. J. W. P. Rosenberg, J. Groll, C. V. C. Bouten, N. A. Kurniawan, A. I. P. M. Smits, D. Gawlitta, Biofabrication 2019, 12, 015009.

[50] F. M. Wunner, M.-L. Wille, T. G. Noonan, O. Bas, P. D. Dalton, E. M. De-Juan-Pardo, D. W. Hutmacher, Adv. Mater. 2018, 30, 1706570.

[51] E. Dondossola, S. Alexander, B. M. Holzapfel, S. Filippini, M. W. Starbuck, R. M. Hoffman, N. Navone, E. M. De-Juan-Pardo, C. J. Logothetis, D. W. Hutmacher, P. Friedl, Sci. Transl. Med. 2018, 10, eaao5726.

[52] P. Diloksumpan, M. de Ruijter, M. Castilho, U. Gbureck, T. Vermonden, P. R. van Weeren, J. Malda, R. Levato, Biofabrication 2020, 12, 025014

[53] C. Black, J. M. Kanczler, M. C. de Andrés, L. J. White, F. M. Savi, O. Bas, S. Saifzadeh, J. Henkel, A. Zannettino, S. Gronthos, M. A. Woodruff, D. W. Hutmacher, R. O. C. Oreffo, Biomaterials 2020, 247, 119998.

[54] N. T. Saidy, T. Shabab, O. Bas, D. M. Rojas-González, M. Menne, T. Henry, D. W. Hutmacher, P. Mela, E. M. De-Juan-Pardo, Front. Bioeng. Biotechnol. 2020, 8, 793.

[55] Q. C. Peiffer, M. de Ruijter, J. van Duijn, D. Crottet, E. Dominic, J. Malda, M. Castilho, Mater. Des. 2020, 195, 109025.
[56] J. Wang, Y. Chen, Y. Bai, D. Quan, Z. Wang, L. Xiong, Z. Shao, W. Sun, S. Mi, Exp. Eye Res. 2020, 195, 108037.
[57] K. Agarwal, R. Sahay, A. Baji, Polymers 2020, 12, 1089.
[58] D. Olvera, M. S. Molina, G. Hendy, M. G. Monaghan, Adv. Funct. Mater. 2020, 1909880.
[59] M. L. Jørgensen, C. Müller, M. Sikkersoq, M. Nadzieja, Z. Zhang, Y. Su, J. Just, K.-L. G. Spindler, M. Chen, Mater. Today Bio 2020, 6, 100052.
[60] Y. Zhang, Z. Zhang, Y. Wang, Y. Su, M. Chen, Mater. Sci. Eng., C 2020, 116, 111070.
[61] Y. Wang, Y. Zhang, Z. Zhang, Y. Su, Z. Wang, M. Dong, M. Chen, Colloids Surf., B 2020, 195, 111210.
[62] S. K. Powell, N. Ristovski, S. Liao, K. A. Blackwood, M. A. Woodruff, K. I. Momot, 3D Print. Addit. Manuf. 2014, 1, 95.
[63] C. B. Dayan, F. Afghah, B. S. Okan, M. Yıldız, Y. Menceloglu, M. Culha, B. Koc, Mater. Des. 2018, 148, 87.
[64] N. C. Paxton, J. Ren, M. J. Ainsworth, A. K. Solanki, J. R. Jones, M. C. Allenby, M. M. Stevens, M. A. Woodruff, Macromol. Rapid Commun. 2019, 40, 1900019.
[65] N. Ristovski, N. Bock, S. Liao, S. K. Powell, J. Ren, G. T. S. Kirby, K. A. Blackwood, M. A. Woodruff, Biointerphases 2015, 10, 011006.
[66] P. R. Buenzli, M. Lanaro, C. S. Wong, M. P. McLaughlin, M. C. Allenby, M. A. Woodruff, M. J. Simpson, Acta Biomater. 2020, 114, 285.
[67] H. Ding, K. Cao, F. Zhang, R. C. Chang, Mater. Des. 2019, 178, 107857.
[68] F. Tourlomousis, A. Babakhanov, H. Ding, R. C. Chang, in Proc. 2015 Manufacturing Science and Engineering, ASME, New York 2015, pp. 1–11.
[69] S. Wang, M. Sarwat, P. Wang, D. C. Surrao, D. G. Harkin, J. A. St John, E. C. L. Bolle, A. Forget, P. D. Dalton, T. R. Dargaville, Macromol. Rapid Commun. 2020, 41, 2000295.
[70] J. Bai, H. Wang, W. Gao, F. Liang, Z. Wang, Y. Zhou, X. Lan, X. Chen, N. Cai, W. Huang, Y. Tang, Int. J. Pharm. 2020, 576, 118941.
[71] Y. Jin, Q. Gao, C. Xie, G. Li, J. Du, J. Fu, Y. He, Mater. Des. 2020, 185, 108274.
[72] N. Dubey, J. A. Ferreira, A. Daghrery, Z. Aytac, J. Malda, S. B. Bhaduri, M. C. Bottino, Acta Biomater. 2020.
[73] R. S. Lakes, Annu. Rev. Mater. Res. 2017, 47, 63.
[74] a) Z. Ma, W. He, T. Yong, S. Ramakrishna, Tissue Eng. 2005, 11, 1149;

b) F. Yang, J. G. C. Wolke, J. A. Jansen, Chem. Eng. J. 2008, 137, 154.
[75] M. A. Woodruff, D. W. Hutmacher, Prog. Polym. Sci. 2010, 35, 1217.
[76] C. Vaquette, S. Ivanovski, S. M. Hamlet, D. W. Hutmacher, Biomaterials 2013, 34, 5538.
[77] A. Escada, J. Machado, A. P. Alves Claro, Mater. Res. 2015, 18, 3.
[78] S. Bertlein, D. Hikimoto, G. Hochleitner, J. Hümmer, T. Jungst, M. Matsusaki, M. Akashi, J. Groll, Small 2018, 14, 1701521.
[79] J. N. Haigh, Y.-m. Chuang, B. Farrugia, R. Hoogenboom, P. D. Dalton, T. R. Dargaville, Macromol. Rapid Commun. 2016, 37, 93.
[80] J. Zeng, H. Wang, Y. Lin, J. Zhang, F. Liang, F. Fang, F. Yang, P. Wang, Z. Zhu, X. Chen, X. Chen, Z. Wang, N. Cai, Y. Tang, P. Wu, Microfluid. Nanofluid. 2018, 22, 23.
[81] T. D. Brown, P. D. Dalton, D. W. Hutmacher, Prog. Polym. Sci. 2016, 56, 116.
[82] J. H. Jordahl, L. Solorio, H. Sun, S. Ramcharan, C. B. Teeple, H. R. Haley, K. J. Lee, T. W. Eyster, G. D. Luker, P. H. Krebsbach, J. Lahann, Adv. Mater. 2018, 30, 1707196.
[83] K.-W. Kim, H. Oh, J. H. Bae, H. Kim, H. C. Moon, S. H. Kim, ACS Appl. Mater. Interfaces 2017, 9, 18994.
[84] M. Castilho, D. Feyen, M. Flandes-Iparraguirre, G. Hochleitner, J. Groll, P. A. F. Doevendans, T. Vermonden, K. Ito, J. P. G. Sluijter, J. Malda, Adv. Healthcare Mater. 2017, 6.
[85] G. Hochleitner, E. Fürsattel, R. Giesa, J. Groll, H.-W. Schmidt, P. D. Dalton, Macromol. Rapid Commun. 2018, 39, 1800055.
[86] G. Hochleitner, J. F. Hümmer, R. Luxenhofer, J. Groll, Polymer 2014, 55, 5017.
[87] D. Nahm, F. Weigl, N. Schaefer, A. Sancho, A. Frank, J. Groll, C. Villmann, H.-W. Schmidt, P. D. Dalton, R. Luxenhofer, Mater. Horiz. 2020, 7, 928.
[88] F. Chen, G. Hochleitner, T. Woodfield, J. Groll, P. D. Dalton, B. G. Amsden, Biomacromolecules 2016, 17, 208.
[89] G. Hochleitner, F. Chen, C. Blum, P. D. Dalton, B. Amsden, J. Groll, Acta Biomater. 2018, 72, 110.
[90] J. N. Haigh, T. R. Dargaville, P. D. Dalton, Mater. Sci. Eng., C 2017, 77, 883.
[91] S. Florczak, T. Lorson, T. Zheng, M. Mrlik, D. W. Hutmacher, M. J. Higgins, R. Luxenhofer, P. D. Dalton, Polym. Int. 2018, 68, 735.
[92] G. Hochleitner, M. Kessler, M. Schmitz, A. R. Boccaccini, J. Teßmar, J. Groll, Mater. Lett. 2017, 205, 257.
[93] a) H. Seyednejad, W. Ji, F. Yang, C. F. van Nostrum, T. Vermonden, J. J. J. P. van den Beucken, W. J. A. Dhert, W. E. Hennink, J. A. Jansen, Biomacromolecules

2012, 13, 3650; b) H. Seyednejad, T. Vermonden, N. E. Fedorovich, R. van Eijk, M. J. van Steenbergen, W. J. A. Dhert, C. F. van Nostrum, W. E. Hennink, Biomacromolecules 2009, 10, 3048.

[94] a) K. W. M. Boere, M. M. Blokzijl, J. Visser, J. E. A. Linssen, J. Malda, W. E. Hennink, T. Vermonden, J. Mater. Chem. B 2015, 3, 9067; b) K. W. M. Boere, J. Visser, H. Seyednejad, S. Rahimian, D. Gawlitta, M. J. van Steenbergen, W. J. A. Dhert, W. E. Hennink, T. Vermonden, J. Malda, Acta Biomater. 2014, 10, 2602.

[95] F. Chen, J. W. S. Hayami, B. G. Amsden, Biomacromolecules 2014, 15, 1593.

[96] a) M. P. Hiljanen-Vainio, P. A. Orava, J. V. Seppälä, J. Biomed. Mater. Res. 1997, 34, 39; b) D. C. Surrao, J. W. S. Hayami, S. D. Waldman, B. G. Amsden, Biomacromolecules 2010, 11, 3624; c) M. C. Azevedo, R. L. Reis, M. B. Claase, D. W. Grijpma, J. Feijen, J. Mater. Sci.: Mater. Med. 2003, 14, 103; d) D. Puppi, N. Detta, A. M. Piras, F. Chiellini, D.

A. Clarke, G. C. Reilly, E. Chiellini, Macromol. Biosci. 2010, 10, 887.

[97] D. C. Surrao, J. C. Y. Fan, S. D. Waldman, B. G. Amsden, Acta Bio mater. 2012, 8, 3704.

[98] J. Hafner, M. Teuschel, M. Schneider, U. Schmid, Polymer 2019, 170, 1.

[99] A. H. Rajabi, M. Jaffe, T. L. Arinzeh, Acta Biomater. 2015, 24, 12.

[100] I. Kanno, H. Kotera, K. Wasa, Sens. Actuators, A 2003, 107, 68.

[101] a) A. Ababneh, U. Schmid, J. Hernando, J. L. Sánchez-Rojas, H. Seidel, Mater. Sci. Eng., B 2010, 172, 253; b) M. Schneider, A. Bittner, U. Schmid, J. Phys. D: Appl. Phys. 2015, 48, 405301.

[102] a) S. M. Damaraju, Y. Shen, E. Elele, B. Khusid, A. Eshghinejad, J. Li, M. Jaffe, T. L. Arinzeh, Biomaterials 2017, 149, 51; b) S. M. Damaraju, S. Wu, M. Jaffe, T. L. Arinzeh, Biomed. Mater. 2013, 8, 045007; c) Y.- S. Lee, T. L. Arinzeh, Tissue Eng., Part A 2012, 18, 2063; d) Y.-S. Lee, G. Collins, T. Livingston Arinzeh, Acta Biomater. 2011, 7, 3877.

[103] H.-H. Lee, H.-S. Yu, J.-H. Jang, H.-W. Kim, Acta Biomater. 2008, 4, 622.

[104] a) L. L. Hench, J. Am. Ceram. Soc. 1991, 74, 1487; b) M. N. Rahaman, D. E. Day, B. S. Bal, Q. Fu, S. B. Jung, L. F. Bonewald, A. P. Tomsia, Acta Biomater. 2011, 7, 2355.

[105] P. D. Dalton, T. B. F. Woodfield, V. Mironov, J. Groll, Adv. Sci. 2020, 7, 1902953.

[106] S. F. Afghah, C. Dikyol, M. Altunbek, B. Koc, Appl. Sci. 2019, 9, 3540.

[107] C. Großhaus, E. Bakirci, M. Berthel, A. Hrynevich, J. C. Kade, G. Hochleitner, J. Groll, P. D. Dalton, Small, unpublished. https://doi.org/10.1002/smll.202003471.

[108] F. M. Wunner, P. Mieszczanek, O. Bas, S. Eggert, J. Maartens, P. D. Dalton, E. M. De-Juan-Pardo, D. W. Hutmacher, Biofabrication 2019, 11, 025004.
[109] T. D. Brown, A. Slotosch, L. Thibaudeau, A. Taubenberger, D. Loessner, C. Vaquette, P. D. Dalton, D. W. Hutmacher, Biointerphases 2012, 7, 13.
[110] T. Jungst, M. L. Muerza-Cascante, T. D. Brown, M. Standfest, D. W. Hutmacher, J. Groll, P. D. Dalton, Polym. Int. 2015, 64, 1086.
[111] H. Xu, M. Yamamoto, H. Yamane, Polymer 2017, 132, 206.
[112] a) M. Alsoufi, A. El-Sayed, Int. J. Mech. Mechatron. Eng. 2017, 17, 7; b) A. Guerrero de Mier, M. M. Espinosa, M. Domínguez, Proc. Eng. 2015, 132, 126.
[113] X. D. Shi, M. P. Brenner, S. R. Nagel, Science 1994, 265, 219.
[114] W. v. Hoeve, S. Gekle, J. H. Snoeijer, M. Versluis, M. P. Brenner, D. Lohse, Phys. Fluids 2010, 22, 122003.
[115] P. T. Brun, B. Audoly, N. M. Ribe, T. S. Eaves, J. R. Lister, Phys. Rev. Lett. 2015, 114, 174501.
[116] P.-T. Brun, C. Inamura, D. Lizardo, G. Franchin, M. Stern, P. Houk, N. Oxman, Phys. Eng. Sci. 2017, 375, 20160156.
[117] F. A. Mier, R. Bhakta, N. Castano, J. Garcia, M. J. Hargather, Fluids 2018, 3, 107.
[118] A. G. Marin, D. Lohse, Phys. Fluids 2010, 22, 122104.
[119] N. Bock, M. A. Woodruff, D. W. Hutmacher, T. R. Dargaville, Polymers 2011, 3, 131.
[120] S. Chiu-Webster, J. R. Lister, J. Fluid Mech. 2006, 569, 89.
[121] C. A. Miles, T. V. Burjanadze, A. J. Bailey, J. Mol. Biol. 1995, 245, 437.
[122] E. Zhmayev, D. Cho, Y. L. Joo, Phys. Fluids 2011, 23, 073102.
[123] X. Yu, M. Feng, R. Zhang, Y. Feng, H. You, F. Guo, S. Chen, D. Zhang, Org. Electron. 2017, 51, 442.
[124] G. Y. Lee, H. T. Lee, W. Ryu, S. H. Ahn, J. Yang, Smart Mater. Struct. 2018, 27, 11LT01.

Chapter 2

– Melt electrowriting of poly(vinylidene difluoride) using a heated collector

Chapter 2 was published as original research article (Kade, JC, Otto, PF, Luxenhofer, R, Dalton, PD. *Melt electrowriting of poly(vinylidene difluoride) using a heated collector*. Polymers for Advanced Technologies, 2021; 32(12): 4951-4955. https://doi.org/10.1002/pat.5463), reproduced from © 2021 John Wiley & Sons Ltd with permission.

This work is part of the project thesis of P.F. Otto, who was directly supervised by Juliane C. Kade during the time from September 2020 to December 2020. J.C. Kade performed the contact angle measurements, XRD measurements, further printing experiments and the composition of the manuscript.

The original text was slightly modified to improve readability.

2.1 Abstract

Previous research on the melt electrowriting (MEW) of poly(vinylidene difluoride) (PVDF) resulted in electroactive fibers, however, printing more than five layers is challenging. Here, we investigate the influence of a heated collector to adjust the solidification rate of the PVDF jet so that it adheres sufficiently to each layer. A collector temperature of 110 °C is required to improve fiber processing, resulting in a total of 20 fiber layers. For higher temperatures and higher layers, an interesting phenomenon occurred, where the intersection points of the fibers coalesced into periodic spheres of diameter 206 ± 52 µm (26G, 150 °C collector temperature, 2000 mm/min, 10 layers in x- and y-direction). The heated collector is an important component of a MEW printer that allows polymers with a high melting point to be processable with increased layers.

2.2 Introduction

Melt electrowriting (MEW) is a high-resolution 3D printing technology that fabricates well-defined structures with fiber diameters down to the sub-micron range.[1,2] The technique offers the production of scaffolds with fibers larger than those processed using solution electrospinning (SES) and smaller than using extrusion-based 3D printing while maintaining the control over the fiber placement. There remains a limited number of polymers that have been processed via MEW, however, this is recently changing.[3] The most commonly used polymer for MEW is poly(ε-caprolactone) (PCL), as it minimally degrades during processing and micrometer-range fibers can be stacked upon each other up to 7 mm in thickness.[4] The MEW processing capabilities for PCL are the current gold standard for the technique.

Another polymer that has been demonstrated compatible with MEW is poly(vinylidene difluoride) (PVDF),[5] an electroactive polymer with a range of applications involving electronic,[6–9] actuating,[10] biomedical materials[11] and membranes.[12–14] One noticeable distinction between MEW processing of PVDF in this study and PCL, is that the printing process becomes unstable above five layers, with warping of the scaffold from the collector back towards the printer head. This limitation in the number of printable layers resulted in thin PVDF samples that were difficult to handle and manipulate.

MEW is, however, a multi-parametric technology and that different variables can be altered to achieve improved printing outcomes, including a final fiber diameter.[15] Other important features include fiber sagging and inter-fiber fusion, as these define the final mechanics of the printed material.

2.3 Materials and Methods

The white PVDF powder (Piezotech Kynar RC10.287) was used as received,[5] loaded into a 3 ml glass syringe (Fortuna Optima 3 ml Luer Lock) and connected to an injection cannula (26-gauge with Luer Lock, Carl Roth, Germany) with a cut length of 5.0 ± 0.5 mm. Direct writing was performed on a MEW printer, equipped with a custom-made heated collector as previously described.[16] More details about the printer and the heated collector can be found in the supporting information. The distance between the glass microscope slides (ground edge, cat # 631–1552, VWR, Germany), which are placed and fixed with tape on the collector, was set to 4.0 ± 0.3 mm depending on the collector temperature. The applied potential difference was kept constant and set to 3.0 ± 0.08 kV. The polymer within the syringe, as well as the nozzle tip were heated to 190 ± 5 °C and, when used, the collector temperature was varied from 50 to 150 °C. For collector temperatures of 100–120 °C, the collector distance required adjustments to 3.3 ± 0.3 mm and at 150 °C the distance was set to 2.5 ± 0.3 mm. The polymer melt was extruded by applying 3.0 ± 0.1 bar, which enabled direct writing at collector speeds between 1000 and 4000 mm/min.

The surface contact angle of the PVDF scaffolds was investigated with an optical contact angle measuring and contour analysis system OCA (DataPhysics Instruments GmbH, Germany). A droplet of deionized water (3 µl) was deposited onto the scaffold and the contact angle was calculated using the SCA 20 software (4.4.3 build 1053, DataPhysics Instruments GmbH, Germany). Experiments were repeated for three different locations on each scaffold with three scaffolds per condition. The average contact angle between each side of the droplet and the scaffold surface was then calculated.

SEM imaging of the scaffolds sputter-coated with 4 nm platinum was performed using a Crossbeam 340 (Carl Zeiss Microscopy GmbH, Germany). Videography was conducted using a Nikon Z6 digital camera with a Nikon ED 200 mm lens and video editing was done using the software DaVinci Resolve 16.2.7.01.

2.4 Results and Discussion

This study was directed towards the influence of a heated collector on the layer stacking of PVDF using MEW, specifically towards avoiding the warping of the final printed structure. As previously shown by Florczak *et al*.[5] the layer stacking was limited to around five layers in x- and y-direction. This phenomenon of fiber lifting is illustrated by screenshots in the Figure S1A–C when a nonheated collector at room temperature is used. This lifting and warping of the printed construct can cause jet break-up and introduces defects as fibers get attracted back towards the print head. Warping is also a phenomenon when the extruded material starts to detach from the collector substrate while printing and does then interfere with the printing process.[17] This phenomenon is well-known from FDM printing and can be related to the shrinkage and remaining stresses in the polymer material when extruded from a nozzle.[17] When processing PVDF using MEW, the printed construct first starts to lift at the edges and corners of the scaffold until it quite often gets attracted to the print head completely, most-likely resulting in melting and damage to the printed structure (Figure S1D–F). However, it can also happen that warping does occur without significantly effecting the resulting scaffold outcome.

To overcome this defect, a heated collector was tested at temperatures between 50 and 150 °C with the latter indicating the maximum temperature as the fibers lose their shape. Such increasing fiber flattening/melting onto the collector substrate is expected and was observed when processing polypropylene or poly(vinylidene fluoride-co-trifluoroethylene) onto a heated collector with increasing temperature.[16,18] This slightly affected the fiber diameter which ranged from 35 ± 16 to 39 ± 9 µm for RT to 110 °C at a printing speed of 4000 mm/min. At collector temperatures of 150 °C, the fiber fusion and coalescing were so conspicuous that the diameter was significantly larger with an average diameter of 48 ± 25 µm when using the same printing parameters. The heating of the collector substrate to 120 °C enabled both fiber adherence and, post-cooling, sample removal without damage.

SEM images show the fiber morphology from above, side and underneath views indicating fiber fusion and embossing with increasing collector temperature varying from room temperature to 50, 100 and 150 °C (Figure 1).

The fabricated constructs in Figure 1 seem to be strongly influenced by the collector temperature as the heat increases the stacking accuracy, as well as the solidification rate of the polymer jet. With increasing collector temperature, starting at 100 °C, the fiber showed rougher surfaces due to spherulite formation. Similarly seen with PCL,[19] these spherulites are formed by the slow cooling of the jet. Spherulite formation is expected to affect the alignment of polymer chains along the

length of the printed fiber, with implications for beta-phase formation (Figure S2). Without the use of a heated collector, the resulting construct shows no fiber fusion limiting the handling of the construct (Video S1) and therefore, leading to an insufficient design stability. With the usage of a heated collector starting at 50 °C, the fabricated constructs show slight fiber fusion (Figure 1). The underneath view of the constructs also shows increasing embossing of the fibers with increasing collector temperature. Figure 2A, B shows how the fiber deposition improves with the collector temperature of 120 °C, while Figure 2C shows how warping occurs with such scaffolds printed with the collector at RT.

Scaffolds printed at RT or a collector temperature of 50 °C seem to be influenced regarding their stacking accuracy by the printing speed (Figure S3). With increasing printing speed, varied from 1000, 2000 to 4000 mm/min, the scaffolds consist of more straight fibers with enhanced printing precision. The fastest speed significantly improved the layer stacking (supporting information Figure S3).

At collector temperatures of at least 100 °C, the lifting of the scaffolds has been reduced compared to room temperature, which might be due to the better adherence and melting of the first fibers printed onto the collector substrate, as indicated by the increasing embossing of the fibers (Figure 1). The heated collector leads to a slower solidification rate of the MEW jet, as well as an increase in the fiber area touching the collector substrate (Figure 1). This change in the jet behavior is also leading to less straight fibers when keeping the collector distance at 4.4 mm, therefore, this gap required adjustments to a smaller distance of 3.3 mm. Furthermore, the differences in the cooling rates/solidification of the jet are leading to a change in the fiber morphology with increasing collector temperature. Fibers with spherulites can be seen starting at a collector temperature of around 100 °C (Figure 1). Similar observations have been reported when MEW-processing polypropylene using a heated collector.[16]

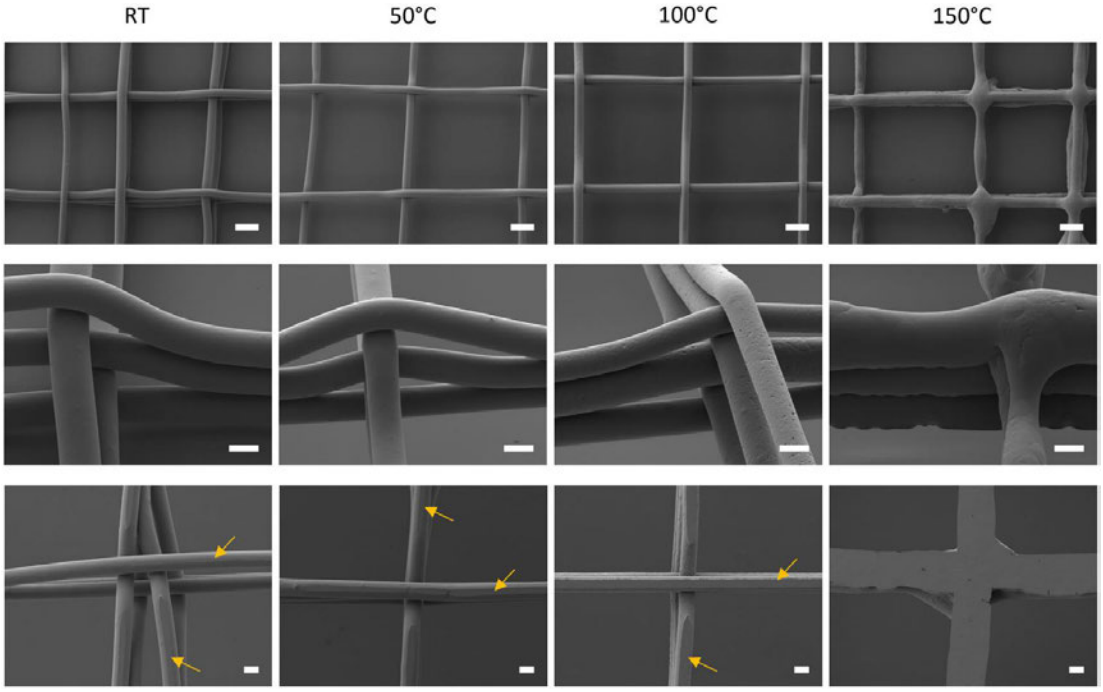

Figure 1. SEM images showing scaffolds with three layers in x- and y-direction printed at 4000 mm/min onto a collector at room temperature, 50, 100 and 150 °C showing the above view (first row), tiled/side view (middle row) and underneath view (third row). Yellow arrows indicate the embossing of the fibers onto the collector substrate, Scale bars for the upper, middle and lower row are 100, 25 and 25 µm, respectively.

At collector temperature of 150 °C, the processed fibers lose their roundish shape as well as the uniformity of the resulting strands. The collector distance was also further reduced to around 2.5 mm to process straight fibers. Furthermore, the cooling of the jet is not fast enough resulting in flattening of each fiber. The individual layers are still visible, nevertheless, the stacked fibers start to form a more solid-like wall. Therefore, a collector temperature of 150 °C was defined as the maximum, as the fibers significantly flatten resulting in an increase in fiber diameter and a less roundish fiber shape.

The maximum number of layers stacked upon each other was either limited due to the lifting of the scaffold, which was reduced using higher collector temperatures but was still present, or due to the heat of the print head getting too hot/close to the uppermost layer (Figure 2D and Figure S4). It was observed that increasing collector temperatures allowed an increasing number of stackable layers up to a collector temperature of 100–120 °C resulting in 20 alternating layers due to the inhibiting warping phenomenon.

However, with increasing number of layers, the height of the constructs increases as well, leading to a decrease in distance between the deposited fiber and the heated print head. This caused melting of the uppermost layer and resulted in “spheres” appearing at the top of the scaffold, as shown in Figure 2D and in Video

S2. While these are the result of an unintended artifact—the excessive heating due to the proximity of the MEW head, the regularity and size of the spheres (206 ± 52 µm) may offer possibilities for certain applications and introduce a clear anisotropy between the top and bottom of the scaffold. Figure 2E summarizes how the maximum number of well-formed layers are affected by the collector temperature.

With respect to utility of these structures on the scaffold, it was investigated for any possible super hydrophobicity in regard to similarities to favorable air-grid surface patterning[20,21] and biomimetic structures.[22] The water contact angles of the processed scaffolds were measured to have a maximum average value of 134 ± 5° for a scaffold with a 250 µm fiber spacing printed with a 30G nozzle and a collector to print head distance of around 2.5 mm (Figure S5).This did not indicate a substantially higher contact angle over flat substrates, with results further summarized in Table S1. Similar contact angles, in the range of 136° to 153°, have been shown in literature for SES membranes.[14,23]

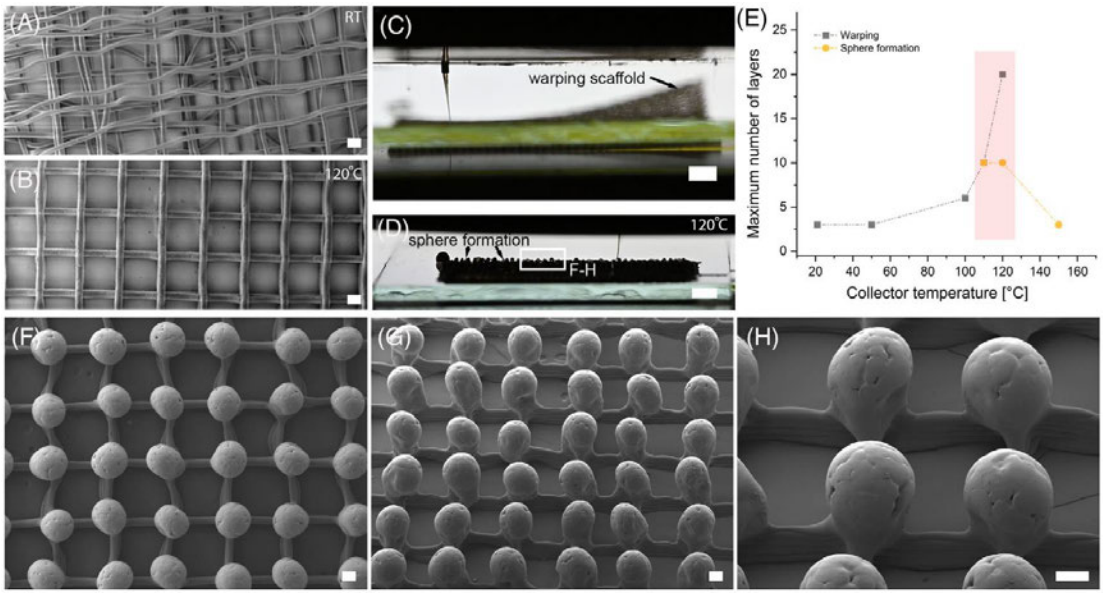

Figure 2. Warping and sphere formation for PVDF scaffolds. SEM image of three-fiber layers at (A) RT and (B) 120 °C. (C) Photograph of a print at RT that is warping and lifting off the collector. (D) Photograph of thicker samples where spheres can be seen forming with increased layer height. (E) Graphical illustration showing the correlation between the maximum number of layers in x- and y-direction and the collector temperature. SEM images showing the coalesced spheres on the scaffold printed at 2000 mm/min due to the heat from the print head (F) above view, (G) side view and overview image and (H) magnified side view showing the still existing lower layers and the coalesced spheres. Scale bars = (A, B) 200 µm, (C, D) 2 mm and (F–H) 100 µm.

When balancing the decrease in the warping phenomenon, as well as sufficient fiber fusion (Figure 1), the focus for the increasing layer stacking will be on the

collector temperatures at 110 °C and 120 °C. Scaffolds printed at these collector temperatures and a printing speed of 4000 mm/min resulted in well-stacked layers with up to 10 layers in x- and y-direction meaning a total of 20 alternating layers, as shown in Figure 3.

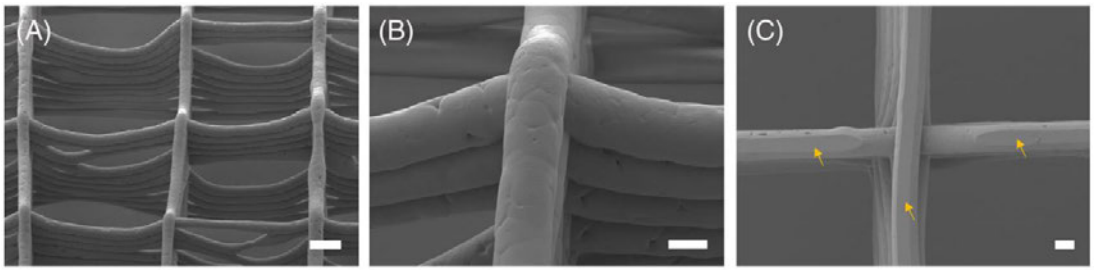

Figure 3. SEM images showing (A, B) above- and (C) underneath-views of a scaffold printed at a collector temperature of 110 °C and a speed of 4000 mm/min resulting in 20 alternating layers. The yellow arrows in (C) indicate the embossing of the fibers when touching the heated collector. Scale bars are (A) 100 µm and (B, C) 25 µm.

The most promising results to enhance the printability of PVDF were achieved with a collector temperature of 110 °C. The amount of layers was increased from previous results[5] printing five layers in each x- and y-direction to up to 10 layers in x- and y-direction. The resulting fibers already show spherulites on their surface similar to the scaffolds printed at a collector temperature of 150 °C (Figure 1). Furthermore, the layers are well stacked on top of each other, however, due to the heat between the collector and the print head and the resulting reduced solidification, some of the fibers are sagging in between the crossing points of the box structure. Even though the lifting and warping of the printed constructs was decreased, it was not achievable to completely prevent this phenomenon from occurring.

The maximum scaffold height using PVDF is ultimately limited by the decreasing distance between the uppermost layer and the print head. As discussed in a previous review,[3] the drawback of MEW regarding the lack of a wide variety of MEW-processable materials, as well as the freedom in design, is quite often limited by the printer design and features. Using a MEW printer with an adjustable Z-height and adjustable high voltage while printing would potentially help to overcome the before mentioned boundary in the layer stacking height, as previously shown.[7] Furthermore, the thermal gradient of the jet[24] would be better defined within a controlled temperature/ humidity environment to tailor fiber fusion.

2.5 Conclusion

In this study, the use of a heated collector enabled the increase in printable layers for PVDF. The heat improved the attachment of the first layers to the collector substrate and successfully decreased the lifting and warping effect. Furthermore, the formation of coalesced spheres appeared at the fiber intersections at collector temperatures of 150 °C that might have some potential utility in scaffold design. Future work should be performed using dynamic printing conditions with both, collector distance and voltage, changing during MEW-processing to control the print and even adjusting the collector temperature during printing. This should control the fiber fusion and solidification rates and allow much thicker samples to be fabricated via MEW.

2.6 Acknowledgements

We gratefully acknowledge financial support by the Volkswagen Foundation (grant number 93418) and additionally Juliane C. Kade is supported by the Joachim Herz Foundation. The video editing by Dr. Ievgenii Liashenko and the technical assistance of Dr. Philipp Stahlhut for SEM imaging is appreciated while the Zeiss Crossbeam CB 340 SEM was funded by the German Research Foundation (DFG) State Major Instrumentation Programme (INST 105022/58-1 FUGG). We also thank Andreas Züge for his input and assistance with recording videos.

2.7 References

[1] Robinson TM, Hutmacher DW, Dalton PD. The next frontier in melt electrospinning: taming the jet. Adv Funct Mater. 2019;29(44): 1904664.

[2] Hochleitner G, Jungst T, Brown TD, et al. Additive manufacturing of scaffolds with sub-micron filaments via melt electrospinning writing. Biofabrication. 2015;7(3):035002.

[3] Kade JC, Dalton PD. Polymers for melt electrowriting. Adv Healthc Mater. 2021;10(1):2001232.

[4] Wunner FM, Wille ML, Noonan TG, et al. Melt electrospinning writing of highly ordered large volume scaffold architectures. Adv Mater. 2018;30(20):e1706570.

[5] Florczak S, Lorson T, Zheng T, et al. Melt electrowriting of electroactive poly(vinylidene difluoride) fibers. Polym Int. 2018;68(4):735-745.

[6] Luo Z, Chen J, Zhu Z, et al. High-resolution and high-sensitivity flexible capacitive pressure sensors enhanced by a transferable electrode
array and a micropillar–PVDF film. ACS Appl Mater Interfaces. 2021;13 (6):7635-7649.

[7] Pramod K, Gangineni RB. Low voltage bipolar resistive switching in self-assembled PVDF nanodot network in capacitor like structures on Au/Cr/Si with Hg as a top electrode. Org Electron. 2017;42:47-51.

[8] Lee JP, Lee JW, Baik JM. The progress of PVDF as a functional mate rial for triboelectric nanogenerators and self-powered sensors. Micromachines. 2018;9(10):532

[9] Wang X, Sun F, Yin G, Wang Y, Liu B, Dong M. Tactile-sensing based on flexible PVDF nanofibers via electrospinning: a review. Sensors. 2018;18(2):330.

[10] Bae J-H, Chang S-H. PVDF-based ferroelectric polymers and dielectric elastomers for sensor and actuator applications: a review. Funct Compos Struct. 2019;1(1):012003.

[11] Li Y, Liao C, Tjong SC. Electrospun polyvinylidene fluoride-based fibrous scaffolds with piezoelectric characteristics for bone and neural tissue engineering. Nanomaterials. 2019;9(7):952.

[12] Munirasu S, Banat F, Durrani AA, Haija MA. Intrinsically superhydrophobic PVDF membrane by phase inversion for membrane distillation. Desalination. 2017;417:77-86.

[13] Wu J, Ding Y, Wang J, et al. Facile fabrication of nanofiber- and micro/nanosphere-coordinated PVDF membrane with ultrahigh permeability of viscous water-in-oil emulsions. J Mater Chem A. 2018;6 (16):7014-7020.

[14] Liao Y, Wang R, Tian M, Qiu C, Fane AG. Fabrication of poly vinylidene fluoride (PVDF) nanofiber membranes by electro-spinning for direct contact membrane distillation. J Membr Sci. 2013;425-426: 30-39.

[15] Hrynevich A, Elci BS, Haigh JN, et al. Dimension-based design of melt electrowritten scaffolds. Small. 2018;14(22):e1800232.

[16] Haigh JN, Dargaville TR, Dalton PD. Additive manufacturing with polypropylene microfibers. Mater Sci Eng C. 2017; 77:883-887.

[17] Alsoufi MS, Elsayed A. Warping deformation of desktop 3D printed parts manufactured by open source fused deposition modeling (FDM) system. Int J Mech Mechatron Eng. 2017;17(4):7-16.

[18] Kade JC, Tandon B, Weichhold J, et al. Melt electrowriting of poly(vinylidene fluoride-co-trifluoroethylene). Polym Int. 2021. https://doi.org/10.1002/pi.6272.

[19] Blum C, Weichhold J, Hochleitner G, et al. Controlling topography and crystallinity of melt electrowritten poly(ϵ-caprolactone) fibers. 3D Print Addit Manufac. 2021;0(0): null.

[20] Chen L, Yang G, Wang S. Air-grid surface patterning provided by superhydrophobic surfaces. Small. 2012;8(7):962-965.

[21] Kwon Y, Patankar N, Choi J, Lee J. Design of surface hierarchy for extreme hydrophobicity. Langmuir. 2009;25(11):6129-6136.

[22] Yan YY, Gao N, Barthlott W. Mimicking natural superhydrophobic surfaces and grasping the wetting process: a review on recent progress in preparing superhydrophobic surfaces. Adv Colloid Interface Sci. 2011;169(2):80-105.

[23] Zhou Z, Wu X-F. Electrospinning superhydrophobic–superoleophilic fibrous PVDF membranes for high-efficiency water–oil separation. Mater Lett. 2015;160:423-427.

[24] Kade JC, Dalton PD. Polymers for melt Electrowriting. Adv Healthc. Mater. 2021;10(1):e2001232.

Chapter 3

– Effect of carbonyl iron particles on the melt electrowriting process

Chapter 3 is based on a manuscript, which is currently in revision (journal: Polymer Composites).

Authors: Juliane C. Kade, Ezgi Bakirci, Biranche Tandon, Danila Gorgol, Miroslav Mrlik, Robert Luxenhofer, Paul D. Dalton.

The chapter is based on the work of the author of this thesis Juliane C. Kade, who performed all MEW experiments, data evaluation of the MEW printing parts and composition of this manuscript.

3.1 Abstract

Melt electrowriting (MEW), a high-resolution additive manufacturing technique, is used in this study to process a magnetic polymer-based blend for the first time. Carbonyl iron (CI) particles homogenously distribute into poly(vinylidene fluoride) (PVDF) to result in well-defined, highly porous structures or scaffolds comprised of fibers ranging from 30 to 50 µm in diameter. We investigate CI particle distribution up to 30 wt.% enabling processing without nozzle clogging and only showed heterogenous fiber morphologies for the highest, 30 wt.%, CI particle loading. The viability of L929 CC1 cell is observed using Live/Dead imaging on the printed samples. MEW processing of PVDF containing CI particles with magnetic properties offers promising potential for the use in stimuli-responsive applications such as 4D printing.

3.2 Introduction

Blends of poly(vinylidene fluoride) (PVDF) and magnetic particles, to induce advantageous properties in addition to PVDF's piezoelectricity, are gaining increased attention [1-5] and are being studied for the stimulation of cells .[6] Different processing techniques for electroactive polymers have been studied [7]; however, many require volatile solvents or lack control over the design and/or the resolution. Using melt electrowriting (MEW) to fabricate 3D constructs offers the possibility to process highly porous and well-defined structures without the addition of toxic solvents.

MEW is a high-resolution additive manufacturing technique that uses an electrohydrodynamic effect to place fibers layer-by-layer to produce designs onto a computer-aided moveable collector.[8, 9] The electrified jet typically produces uniform fibers with diameters between 5 and 50 µm.

After poly(ε-caprolactone), PVDF is the most commonly MEW-processed polymer [10, 11] but has not yet been combined with particles. While particles of hydroxyapatite (HAp) [12]; strontium-substituted bioactive glass (SrBG) [13]; bioactive milk proteins, lactoferrin, whey protein [14] or reduced graphene oxide (rGO) [15] have been combined with PCL, particles with magnetic capacity such as carbonyl iron (CI) have never been studied for MEW. The CI particles constitute a magnetic powder known for its high thermal stability, non-cytotoxicity [16, 17] and is often used in magnetic polymer-based blends.[5, 18, 19]

Furthermore, shape changing scaffolds, either induced by different printing parameters [20] or through a multiphasic material combination [21, 22], are of interest due to their ability to change their configuration.[23, 24. An interesting class of materials enabling these properties are, for example, hydrogels [20-25] and electroactive materials.[26] Therefore, 4D printing enables motions or functions of 3D printed constructs controlled by external stimuli.[24] One example for such stimuli responsive materials are magnetically responsive polymers.[27-29]

In this study, PVDF blends containing up to 30 wt.% CI particles were prepared and characterized for thermal properties and melt viscosity. Different blends with particles showed sufficient MEW processability without nozzle clogging [30] or the use of solvents to lower the viscosity, as previously shown by Paxton *et al*. [13]. MEW-processed constructs were imaged and characterized using scanning electron microscopy (SEM) and energy-dispersive X-ray spectroscopy (EDX). The magnetic behavior of the printed constructs was shown, and the cell viability was investigated using L929 CC1 cells over a period of 4 days. PVDF containing up to 30 wt.% CI

particles offer the potential use for magnetoactive cell stimulation in tissue engineering.

3.3 Materials and methods

Materials

As magnetic particles, CI (BASF, Germany) with 99.5% purity, magnetic saturation of 229 emu g^{-1} and negligible magnetization saturation [16], necessary to provide suitable magnetic response in blends, was chosen. These particles were also used due to their known cytocompatibility.[16, 17] As the polymer matrix, PVDF (Sigma Aldrich, USA) was used as received. PVDF has M_n = 107 kg/mol, with a dispersity of Đ = 2.33 and was supplied in the form of pellets.

Mixing and Viscosity

The master batches consisting of PVDF and CI particles were mixed using laboratory twin-screw mixing machine DSM MC-15 (Xplore Instruments, Netherlands). The rheological characteristics of the blends were measured utilizing rheometer Physica (MCR502, Anton Paar, Austria) connected to Peltier heating/cooling fixture and parallel-plate geometry (PP10). Samples in form of discs with thicknesses of 1 mm and 10 mm in diameter were investigated and to avoid the sample slippage, a constant 0.3 N force was applied. First, the linear viscoelastic region was identified, and all further measurements were performed in this region. Subsequently, a frequency sweep in the range from 10^{-1} to 10^{1} Hz was performed. The values given in the figures are average values obtained from three individual measurements. It should be noted that standard deviation of the individual measurements is not higher than the height of the symbol presented in the Figure 1.

Differential Scanning Calorimetry (DSC)

Differential scanning calorimetry (DSC) measurements were performed using differential scanning calorimeter (DSC-1, Mettler-Toledo, Switzerland). The nitrogen gas flow rate was set to 20 mL min^{-1} and the weight of the investigated samples ranged from 4 to 5 mg. DSC curves were reached by heating from -80 to 200 °C and back with a rate of 10 °C min^{-1}. All experiments were performed three times, and average values were used. In order to show if the presence of CI particles affects the crystallinity, X_c of the PVDF based samples was calculated using equation (1) [31], where ΔH_m is the heat of fusion for individual samples and ΔH_m^0 is the heat of fusion obtained for 100% crystalline PVDF (104.5 J g-1).

$$X_c = \frac{\Delta H_m}{\Delta H_m^0} \times 100 \qquad (1)$$

Melt Electrowriting Configuration

MEW was conducted using a custom-built MEW printer as previously described.[32] The material was placed in a glass syringe (3 mL FORTUNA OPTIMA Luer Lock Tip, Poulten & Graf GmbH, Wertheim, Germany) and connected to a metal injection cannula (26-gauge with Luer Lock, Carl Roth, Germany), which was ground manually to a length of 7.0 ± 0.4 mm. The print head and the nozzle were heated to 200 °C for each material. The collector distance to the print head was set to 2.5 mm and a voltage of 1.5 kV and -1.5 kV was applied to the nozzle tip and the collector, respectively.

Sample Imaging and Videography

For sample imaging, a scanning electron microscope (SEM) (Crossbeam 340 SEM equipped with GEMINI e-Beam column, Carl Zeiss Microscopy, Göttingen, Germany) was used. Energy dispersive X-ray spectroscopy (EDX) was conducted on 4 nm platinum sputter-coated (Leica EM ACE600, Wetzlar, Germany) blends.

Magnetic behavior was demonstrated on highly porous PVDF MEW-processed scaffolds containing 30 wt.% CI particles and a PVDF scaffold without particles as a non-magnetic sample was demonstrated using a magnet. The magnetic properties of the CI particles have been investigated using vibration sample magnetometry (VSM) in previous studies.[16, 17]

Videography was performed using a Nikon Z6 digital camera with Nikon ED 200 mm lens. Editing of the videos was performed using the software DaVinci Resolve 16.

Cell Viability Tests

The viability of murine fibroblast cell line L929 CC1 (ATCC, Rockville, USA) which cultured on neat PVDF and PVDF containing 1, 5, 15, and 30 wt.% of CI particles scaffolds were observed via live/dead-staining (LIVE/DEAD® Viability/Cytotoxicity Kit, ThermoFisher Scientific). The five hundred thousand L929 CC1 were seeded on each scaffold. Cells were cultured up to 4 days in DMEM F-12 (+1 vol.% Pen/Strep and +10 vol.% FCS) (Gibco, Thermo Fisher Scientific Inc., Waltham, USA) at 37 °C (5% CO_2/95% air). Live/dead-staining was performed and the cell seeded scaffolds were imaged using fluorescence microscopy (Axio Observer, Zeiss equipped with epi fluorescence optics, a MRm camera and an Apotome; Zeiss, Oberkochen, Germany).

3.4 Results and Discussion

TGA measurements revealed the thermal stability of the neat PVDF, as well as the blends with varying CI particle contents up to 350 °C (Figure S1). Using DSC, the influence of the particle concentration on the melting temperature was investigated and demonstrated that the measured melting point of PVDF does not shift by the addition of CI as it remains at 172 °C despite the increasing amount of the magnetic particles, as listed in Table 1. The corresponding graphs are shown in Figure S2A.

Neat PVDF shows an X-ray diffraction pattern similar to previously shown in the literature.[31] The overall crystallinity was nearly identical for individual master batches shown by the XRD measurements (Figure S2B). The continual decrease of the crystallinity is connected to the increasing amount of the magnetic particles in the master batches and thus the lower amount of PVDF present in the system (Table 1).

Table 1. Summarized results obtained for various master batches of PVDF containing CI particles up to 30 wt.%.

Sample code	T_m [°C]	ΔH_m [J g^{-1}]	X_c [%]
neat PVDF	172	43	41
PVDF 1 - 1 wt.%	172	42	41
PVDF 2 - 5 wt.%	172	41	39
PVDF 3 - 15 wt.%	172	36	35
PVDF 4 - 30 wt.%	172	32	31

Another important factor for MEW is the melt viscosity of the polymer. In a study by Florczak *et al*. [10], it was shown that PVDF, investigated under steady shear conditions, has a strong pseudoplastic character and a viscosity around 100 Pa s for low shear rates at 190 °C. In the present study, a different grade of PVDF was employed, and the addition of CI particles could be expected to increase the viscosity. At 200 °C, the viscosity of neat PVDF and blends is quite similar and in fact the presence of magnetic particles only slightly increases viscosity with increasing CI content (Figure 1). The relatively minor changes in the viscosity should therefore not have a major effect on the MEW processing.

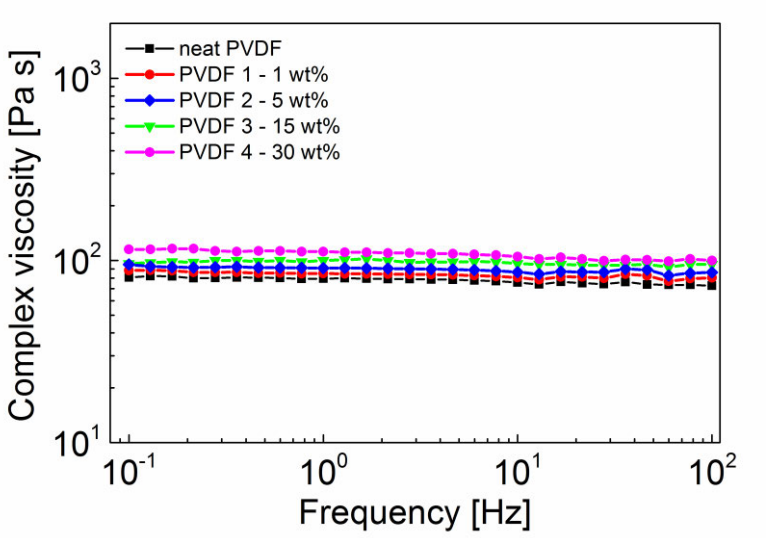

Figure 1. Dependence of the complex viscosity on the frequency for various master batches containing different amounts of carbonyl iron (CI) (1-30 wt.%) at temperature of 200 °C.

MEW of PVDF and its copolymers, as already shown by Florczak *et al*. [10] and Kade *et al*. [33], provides an option for solvent-free fabrication of well-defined structures using electroactive polymers (EAPs). Furthermore, combining these materials with magnetic particles offers the possibility to introduce magnetoactivity. Here, we could process PVDF with different amounts of CI particles (1, 5, 15 and 30 wt.%) using MEW without clogging the nozzle. Interestingly, the printing of all five materials below the CTS resulted in fiber pulsing and therefore, major variations of the fiber diameter, as shown in Supporting Video 1. Due to the fast solidification of the PVDF, the extruded material cools down “in air” while the fibers are coiling for printing speeds below the CTS. Stereomicroscopic images of all processed blends visualize the increasing amount of particles and the color change to more black fibers depending on the particle content (Figure 2).

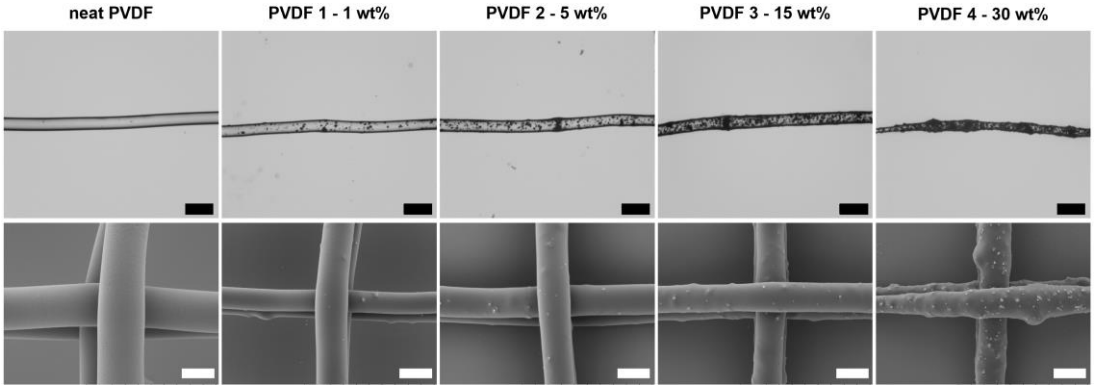

Figure 2. Images of the neat PVDF and blends with increasing magnetic CI particle content. Stereomicroscope images are shown in the first row (scale bar = 100 µm) and SEM images in the second row (scale bar = 50 µm).

When printing at speeds greater than the CTS, the neat PVDF fibers showed a homogenous and smooth fiber surface with similar results for the blends containing 1 and 5 wt.% of CI particles. Fiber uniformity starts to be affected for the PVDF / 15 wt.% CI, which can also be seen in the higher standard deviation for the fiber diameters (Table 2).

Table 2. Influence of two different collector speeds on the fiber diameter for neat PVDF and the different PVDF blends containing 1 wt.%, 5 wt.%,15 wt.% and 30 wt.% CI particles.

Collector speed	**neat PVDF**	**PVDF 1**	**PVDF 2**	**PVDF 3**	**PVDF 4**
		1 wt.% CI	**5 wt.% CI**	**15 wt.% CI**	**30 wt.% CI**
[mm/min]	**Diameter [µm]**				
2000	51 ± 7	42 ± 5	42 ± 5	50 ± 9	37 ± 12
2800	42 ± 9	40 ± 6	43 ± 10	45 ± 12	33 ± 11

Furthermore, the fiber diameter tested at two different speeds well above the CTS, remained similar for the different blends except PVDF / 30 wt.% CI, which resulted in a decrease of fiber diameters of around 10 µm (Table 2). For the PVDF blends with 15 and 30 wt.% of particles, the fiber deposition and layer stacking accuracy were reduced with higher particle content (Figure 2). Additionally, the warping of printed constructs was visible for all materials (Supporting Video S1) affecting the printing process and resulting in limited layer stacking, as previously mentioned and observed for PVDF.[10, 33]

With increasing number of particles, more particles are visible on the fiber morphology as shown in Figure 2. Even though the particles appear mostly homogenously dispersed within the PVDF matrix, the blends with 5 wt.% or more CI also show domains with agglomerated particles. A similar surface morphology was observed in films of 1 to 10 wt.% CI particles in PVDF by SEM showing a rougher surface with increasing particle content compared to neat PVDF films.[5]

EDX results of the fabricated scaffolds proved the presence of the iron (Fe) and gave further evidence of the rather homogenous distribution of the particles within the fibers even for PVDF with 30 wt.% magnetic particles (Figure 3). In Figure 3A, agglomerations of a few particles are visible on the fiber surface. Important to note, the larger inhomogeneities (bulges) of the fibers are apparently not directly connected to the CI, as these bulges do not show a visible increase or clustering of Fe in EDX. However, similar bulges have been observed for CI particles (3 to 8 %m) dispersed in a polysulfone polymer solution within electrospun fibers, especially with increasing additive content. Higher particle amounts within the polymer solution did not enable sufficient fiber production resulting in fiber clogging.[34] Figure 3

highlights the reduced stacking accuracy of the PVDF 4 - 30 wt.% CI blend, as well as the less uniform fiber diameter.

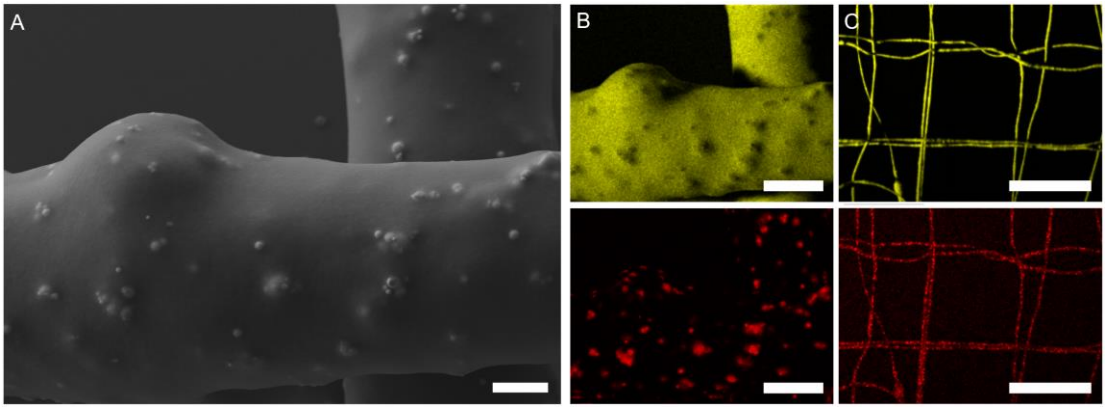

Figure 3. A) SEM and B-C) EDX images of a scaffolds printed with PVDF including 30 wt.% CI particles showing homogenous distribution throughout the printed fibers. In B-C) top images indicating the fluorine (F) within the PVDF in yellow and bottom images the iron (Fe) in red. Scale bars are A) 10 µm, B) 25 µm and C) 1 mm.

The incorporated CI particles are known to offer potential magnetic behavior and have previously been investigated using a vibrating sample magnetometer (VSM) resulting in values between 188 to 229 emu g^{-1} for the neat particles.[16, 17] Furthermore, CI particles incorporated within a PVDF film showed a saturation magnetization starting at 18 emu g^{-1} for 1 wt.% and increased with increasing particle amount to 29 emu g^{-1} for 10 wt.% as investigated by Sang *et al*. [5].

The magnetic behavior of the MEW-processed scaffold using the PVDF containing 30 wt.% CI particles is demonstrated in Supporting Video S2 compared to a scaffold made from neat PVDF. The scaffold containing CI particles adhered to magnets and followed its movement in contrast to the neat PVDF scaffold without particles. All blends with CI particles showed magnetic properties and resulted in stronger attraction to the magnet with increasing concentration.

The fibers demonstrated here could be the first step towards magnetically responsive 3D constructs with promising applications for stimuli-responsive 4D printing. MEW enables to overcome current resolution limits of other 3D printing techniques and offers freedom in design of scaffolds with high accuracy in fiber placement. A recent study, for example, developed a MEW fiber embedded silicone tube that provided ultra-fast actuation.[25] Furthermore, improved MEW printer capable of printing more than one material at a time could further enhance the complexity of printed constructs by combining advantageous properties of different materials, such as producing shape morphing constructs [21-23, 28] within a single processing step.

The live/dead assay was performed with L929 cells on those scaffolds at day 1 and day 4 as seen Figure 4. The cell viability at day 1 for the PVDF control was 96.8±2, and 87±8, 89±1, 82±11, 80±7% for 1 wt.%, 5 wt.%, 15 wt.% and 30 wt.% CI particles containing scaffolds, respectively. The fluorescence images of L929 cells on the novel hybrid materials also confirmed cells adhering well to PVDF scaffolds containing CI particles. The cell viability did not change significantly during the incubation time. The lowest cell viability was shown for scaffolds containing 30 wt.% CI particles.

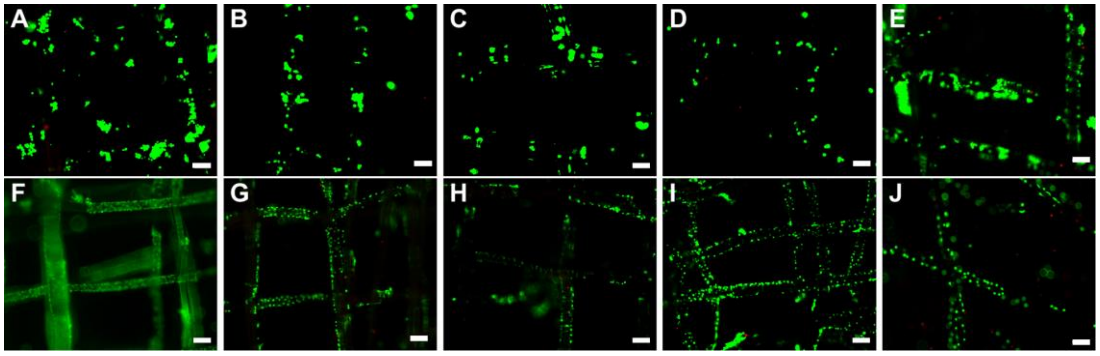

Figure 4. Showing Live/Dead staining using L929 cells with the corresponding cell viability at A-E) day 1 and F-J) day 4 for MEW-processed scaffolds using A, F) neat PVDF without particles and blends containing B, G) 1 wt.%, C, H) 5 wt.%, D, I) 15 wt.%, and E, J) 30 wt.% of CI particles. Scale bars are 100 µm. Green (Calcein AM): live cells, red (Ethidium homodimer^{-1}): dead cells.

The viability test of the electroactive PVDF scaffolds containing up to 30 wt.% CI particles could lead to promising applications, especially for biomechanical stimulation through loads induced via magnetic fields.[6] Piezoelectric PVDF containing magnetostrictive particles such as cobalt iron oxide ($CoFe_2O_4$) demonstrated promising results for bone tissue repair strategies due to the magneto mechanical and magnetoelectrical response of the material.[6] These hybrid materials have the potential for many tissue engineering applications since they can stimulate tissue regeneration via magnetic to mechanical to electrical conversion/stimuli and external scaffold control via magnetic fields.[35] Similar applications are envisioned for the presented microperiodic PVDF scaffolds.

3.5 Conclusion

In summary, the MEW-processability of PVDF blends with up to 30 wt.% CI particles was demonstrated, including a sufficient distribution of the particles without the use of solvent or nozzle clogging. Investigations of the crystalline phase using XRD and DSC showed negligible change in the material properties, and viscoelastic investigations confirmed slightly increased viscosity for master batches with higher particles content. Furthermore, the particles did not change significantly affect the printability of the blends as we could process the melts to obtain stable jets and microfiber scaffolds. Mostly, the fabricated fibers were uniform and showed diameters between 30 and 50 µm. Only the blend containing 30 wt.% CI particles resulted in less uniform fibers, as well as less accurate placement and rougher fiber surface. Nevertheless, to the best of our knowledge, this is the highest particle amount in MEW-processed polymers without the need of additives or solvents and still enabling a stable jet and sufficient MEW-processability without major changes compared to the neat material.

Furthermore, the cell viability of L929 cells showed similar behavior for the PVDF control sample and the PVDF blends containing up to 30 wt.% CI particles with sufficient cell adherence at day 4. Due to their proven high viability results, these blends offer the possibility for the use in magnetoactive cell stimulation or stimuli responsive 4D printing in combination with MEW offering the flexibility in design with resulting fiber diameters in the lower micron range.

3.6 Acknowledgement

We gratefully acknowledge financial support by the Volkswagen Foundation (grant number 93418). In addition, J. C. K. is supported by the Joachim Herz Foundation. The technical assistance of Philipp Stahlhut and Judith Friedlein for SEM imaging and EDX analysis and Simon Luposchainsky for recording the magnetic properties is appreciated while the Zeiss Crossbeam CB 340 SEM was funded by the German Research Foundation (DFG) State Major Instrumentation Programme (INST 105022/58-1 FUGG). M. M. and D.G. would like to acknowledge to the Czech Science Foundation, grant no. 19-17457S and the Ministry of Education, Youth and Sports of the Czech Republic - DKRVO (RP/CPS/2020/003) for financial support.

3.7 References

[1] C. Tsonos, H. Zois, A. Kanapitsas, N. Soin, E. Siores, G.D. Peppas, E.C. Pyrgioti, A. Sanida, S.G. Stavropoulos, G.C. Psarras, Polyvinylidene fluoride/magnetite nanocomposites: Dielectric and thermal response, Journal of Physics and Chemistry of Solids 129 (2019) 378-386.

[2] T. Prabhakaran, J. Hemalatha, Ferroelectric and magnetic studies on unpoled Poly (vinylidine Fluoride)/Fe3O4 magnetoelectric nanocomposite structures, Materials Chemistry and Physics 137(3) (2013) 781-787.

[3] C. Tsonos, N. Soin, G. Tomara, B. Yang, G.C. Psarras, A. Kanapitsas, E. Siores, Electromagnetic wave absorption properties of ternary poly(vinylidene fluoride)/magnetite nanocomposites with carbon nanotubes and graphene, RSC Advances 6(3) (2016) 1919-1924.

[4] H. Wang, Q. Fu, J. Luo, D. Zhao, L. Luo, W. Li, Three-phase Fe3O4/MWNT/PVDF nanocomposites with high dielectric constant for embedded capacitor, Applied Physics Letters 110(24) (2017) 242902.

[5] M. Sang, S. Wang, M. Liu, L. Bai, W. Jiang, S. Xuan, X. Gong, Fabrication of a piezoelectric polyvinylidene fluoride/carbonyl iron (PVDF/CI) magnetic composite film towards the magnetic field and deformation bi-sensor, Composites Science and Technology 165 (2018) 31-38.

[6] M.M. Fernandes, D.M. Correia, C. Ribeiro, N. Castro, V. Correia, S. Lanceros-Mendez, Bioinspired Three-Dimensional Magnetoactive Scaffolds for Bone Tissue Engineering, ACS Applied Materials & Interfaces 11(48) (2019) 45265-45275.

[7] C. Ribeiro, C.M. Costa, D.M. Correia, J. Nunes-Pereira, J. Oliveira, P. Martins, R. Gonçalves, V.F. Cardoso, S. Lanceros-Méndez, Electroactive poly(vinylidene fluoride)-based structures for advanced applications, Nature Protocols 13(4) (2018) 681-704.

[8] G. Hochleitner, T. Jüngst, T.D. Brown, K. Hahn, C. Moseke, F. Jakob, P.D. Dalton, J. Groll, Additive manufacturing of scaffolds with sub-micron filaments via melt electrospinning writing, Biofabrication 7(3) (2015) 035002.

[9] T.D. Brown, P.D. Dalton, D.W. Hutmacher, Direct Writing By Way of Melt Electrospinning, Advanced Materials 23(47) (2011) 5651-5657.

[10] S. Florczak, T. Lorson, T. Zheng, M. Mrlik, D.W. Hutmacher, M.J. Higgins, R. Luxenhofer, P.D. Dalton, Melt electrowriting of electroactive poly(vinylidene difluoride) fibers, Polymer International 68(4) (2019) 735-745.

[11] J.C. Kade, P.F. Otto, R. Luxenhofer, P.D. Dalton, Melt electrowriting of poly(vinylidene difluoride) using a heated collector, Polymers for Advanced Technologies n/a(n/a).

[12] A. Abdal-hay, N. Abbasi, M. Gwiazda, S. Hamlet, S. Ivanovski, Novel polycaprolactone/hydroxyapatite nanocomposite fibrous scaffolds by direct melt-electrospinning writing, European Polymer Journal 105 (2018) 257-264.

[13] N.C. Paxton, J. Ren, M.J. Ainsworth, A.K. Solanki, J.R. Jones, M.C. Allenby, M.M. Stevens, M.A. Woodruff, Rheological Characterization of Biomaterials Directs Additive Manufacturing of Strontium-Substituted Bioactive Glass/Polycaprolactone Microfibers, Macromolecular Rapid Communications 0(0) (2019) 1900019.

[14] E. Hewitt, S. Mros, M. McConnell, J. Cabral, A. Ali, Melt-electrowriting with novel milk protein/PCL biomaterials for skin regeneration, Biomedical Materials (2019).

[15] K. Somszor, O. Bas, F. Karimi, T. Shabab, N.T. Saidy, A.J. O'Connor, A.V. Ellis, D. Hutmacher, D.E. Heath, Personalized, Mechanically Strong, and Biodegradable Coronary Artery Stents via Melt Electrowriting, ACS Macro Letters 9(12) (2020) 1732-1739.

[16] M. Cvek, M. Mrlík, M. Ilčíková, J. Mosnáček, V. Babayan, Z. Kuceková, P. Humpolíček, V. Pavlínek, The chemical stability and cytotoxicity of carbonyl iron particles grafted with poly(glycidyl methacrylate) and the magnetorheological activity of their suspensions, RSC Advances 5(89) (2015) 72816-72824.

[17] M. Mrlík, M. Ilčíková, M. Cvek, V. Pavlínek, A. Zahoranová, Z. Kroneková, P. Kasak, Carbonyl iron coated with a sulfobetaine moiety as a biocompatible system and the magnetorheological performance of its silicone oil suspensions, RSC Advances 6(39) (2016) 32823-32830.

[18] D. Min, W. Zhou, F. Luo, D. Zhu, Facile preparation and enhanced microwave absorption properties of flake carbonyl iron/Fe3O4 composite, Journal of Magnetism and Magnetic Materials 435 (2017) 26-32.

[19] Y. Qing, D. Min, Y. Zhou, F. Luo, W. Zhou, Graphene nanosheet- and flake carbonyl iron particle-filled epoxy–silicone composites as thin–thickness and wide-bandwidth microwave absorber, Carbon 86 (2015) 98-107.

[20] D. Nahm, Poly(2-oxazine) Based Biomaterial Inks for the Additive Manufacturing of Microperiodic Hydrogel Scaffolds
Poly(2-oxazine) Basierte Biomaterialtinten für die Additive Fertigung von Mikroperiodischen Hydrogelstrukturen, 2021.

[21] G. Constante, I. Apsite, H. Alkhamis, M. Dulle, M. Schwarzer, A. Caspari, A. Synytska, S. Salehi, L. Ionov, 4D Biofabrication Using a Combination of 3D Printing and Melt-Electrowriting of Shape-Morphing Polymers, ACS Applied Materials & Interfaces 13(11) (2021) 12767-12776.

[22] J. Uribe-Gomez, A. Posada-Murcia, A. Shukla, M. Ergin, G. Constante, I. Apsite, D. Martin, M. Schwarzer, A. Caspari, A. Synytska, S. Salehi, L. Ionov, Shape-Morphing Fibrous Hydrogel/Elastomer Bilayers Fabricated by a Combination of 3D Printing and Melt Electrowriting for Muscle Tissue Regeneration, ACS Applied Bio Materials 4(2) (2021) 1720-1730.
[23] A. Kirillova, R. Maxson, G. Stoychev, C.T. Gomillion, L. Ionov, 4D Biofabrication Using Shape-Morphing Hydrogels, Advanced Materials 29(46) (2017) 1703443.
[24] X. Kuang, D.J. Roach, J. Wu, C.M. Hamel, Z. Ding, T. Wang, M.L. Dunn, H.J. Qi, Advances in 4D Printing: Materials and Applications, Advanced Functional Materials 29(2) (2019) 1805290.
[25] O. Bas, B. Gorissen, S. Luposchainsky, T. Shabab, K. Bertoldi, D.W. Hutmacher, Ultrafast, miniature soft actuators, Multifunctional Materials 4(4) (2021) 045001.
[26] A.Y. Chen, E. Pegg, A. Chen, Z. Jin, G.X. Gu, 4D Printing of Electroactive Materials, Advanced Intelligent Systems n/a(n/a) 2100019.
[27] P. Zhu, W. Yang, R. Wang, S. Gao, B. Li, Q. Li, 4D Printing of Complex Structures with a Fast Response Time to Magnetic Stimulus, ACS Applied Materials & Interfaces 10(42) (2018) 36435-36442.
[28] W. Zhao, F. Zhang, J. Leng, Y. Liu, Personalized 4D printing of bioinspired tracheal scaffold concept based on magnetic stimulated shape memory composites, Composites Science and Technology 184 (2019) 107866.
[29] Y. Zhang, Q. Wang, S. Yi, Z. Lin, C. Wang, Z. Chen, L. Jiang, 4D Printing of Magnetoactive Soft Materials for On-Demand Magnetic Actuation Transformation, ACS Applied Materials & Interfaces 13(3) (2021) 4174-4184.
[30] G. Hochleitner, M. Kessler, M. Schmitz, A.R. Boccaccini, J. Teßmar, J. Groll, Melt electrospinning writing of defined scaffolds using polylactide-poly(ethylene glycol) blends with 45S5 bioactive glass particles, Materials Letters 205 (2017) 257-260.
[31] M. Mrlík, J. Osička, M. Cvek, M. Ilčíková, P. Srnec, D. Gorgol, P. Tofel, Comparative Study of PVDF Sheets and Their Sensitivity to Mechanical Vibrations: The Role of Dimensions, Molecular Weight, Stretching and Poling, Nanomaterials 11(7) (2021) 1637.
[32] M. de Ruijter, A. Hrynevich, J.N. Haigh, G. Hochleitner, M. Castilho, J. Groll, J. Malda, P.D. Dalton, Out-of-Plane 3D-Printed Microfibers Improve the Shear Properties of Hydrogel Composites, Small 14(8) (2018) 1702773.

[33] J.C. Kade, B. Tandon, J. Weichhold, D. Pisignano, L. Persano, R. Luxenhofer, P.D. Dalton, Melt electrowriting of poly(vinylidene fluoride-co-trifluoroethylene), Polymer International n/a(n/a).

[34] D.-C. Silveira, T.-T.-d.-S. Braga, D.-M. Gil, N.-A.-d.-S. Gomes, L.-M. Guerrini, E.-C. Botelho, Electromagnetic Characterization of Recyclable Polymer Nanofibers Based on PSU/Carbonyl Iron, Journal of Renewable Materials 7(3) (2019) 279--287.

[35] B. Hermenegildo, C. Ribeiro, L. Pérez-Álvarez, J.L. Vilas, D.A. Learmonth, R.A. Sousa, P. Martins, S. Lanceros-Méndez, Hydrogel-based magnetoelectric microenvironments for tissue stimulation, Colloids and Surfaces B: Biointerfaces 181 (2019) 1041-1047.

Chapter 4

– Melt Electrowriting of poly(vinylidene fluoride-*co*-trifluoroethylene)

Chapter 4 was published as original research article (Kade, J.C., Tandon, B., Weichhold, J., Pisignano, D., Persano, L., Luxenhofer, R. and Dalton, P.D., *Melt electrowriting of poly(vinylidene fluoride-co-trifluoroethylene)*. Polymer International, 2021, 70: 1725-1732. https://doi.org/10.1002/pi.6272), reproduced from © 2021 The Authors. Polymer International published by John Wiley & Sons Ltd on behalf of Society of Industrial Chemistry. This is an open access article under the terms of the Creative Commons Attribution License, which permits use, distribution and reproduction in any medium, provided the original work is properly cited.

The original text was slightly modified to improve readability.

4.1 Abstract

Poly(vinylidene fluoride-*co*-trifluoroethylene) (P(VDF-*co*-TrFE)) is an electroactive polymer with growing interest for applications in biomedical materials and flexible electronics. In this study, a solvent-free additive manufacturing technique called melt electrowriting (MEW) has been utilized to fabricate well-defined microperiodic structures of the copolymer (P(VDF-*co*-TrFE)). MEW of the highly viscous polymer melt was initiated using a heated collector at temperatures above 120 °C and required remarkably slow collector speeds below 100 mm/min. The fiber surface morphology was affected by the collector speed and an increase in β-phase was observed for scaffolds compared to the unprocessed powder. Videography shows vibrations of the P(VDF-*co*-TrFE) jet previously unseen during MEW, probably due to repeated charge buildup and discharge. Furthermore, piezo-force microscopy measurements demonstrated the electromechanical response of MEW-fabricated fibers. This research therefore achieves the melt electrohydrodynamic processing of fibers with micrometer resolution into defined structures with an important electroactive polymer.

4.2 Introduction

Electroactive polymers with piezoelectric properties are of increasing interest for biomedical applications, in particular for the electrical stimulation of cells without the need for an external power supply.[1–4] Poly(vinylidene fluoride) (PVDF) and the copolymer poly(vinylidene fluoride-*co*-trifluoroethylene) (P(VDF-*co*-TrFE)) are often used for biomedical applications[2,5–9] owing to their flexibility, non-toxicity and good chemical resistance.[1,2,6,10] The piezoelectric properties of such polymers emerge when the crystalline structure is in the all-trans conformation which results in a net dipole moment.[1] PVDF is piezoelectric in the β-phase conformation, the content of which can be increased at the expense of the α-phase (*trans-gauche-trans-gauche* conformation) by stretching, poling or annealing of the raw material.[9,11] In contrast, P(VDF-*co*-TrFE) inherently prefers to crystallize into a crystal structure similar to the all-trans conformation (β-phase) due to the steric hindrance provided by the higher amount of fluorine atoms introduced by TrFE.[1,12–14] However, to improve the alignment of polymer chains/crystalline domains and generate a continuous macroscopic polarization, the copolymer P(VDF-*co*-TrFE) needs to be polarized by an electric field.[14] Solution electrospun PVDF and P(VDF-*co*-TrFE) have been extensively studied for tissue engineering applications by Arinzeh and colleagues.[7,15–19] Small diameter P(VDF-*co*-TrFE) fibers (ca 970 ± 480 nm) showed in vitro cytocompatibility using human skin fibroblasts[19] and improved neurite extension using Schwann cells and/or dorsal root ganglion[7,18] and human neural stem/progenitor cells.[17] An increase in chondrogenic and/or osteogenic differentiation of human mesenchymal stem cells on PVDF[16] and P(VDF-*co*-TrFE) fibers[15] has also been shown. Due to the increasing interest in PVDF-based polymers, a variety of processing technologies have been studied in an attempt to increase the β-phase, as well as to investigate methods to control the fabrication of samples and constructs.[9] However, most of these processing methods involve use of toxic solvents; therefore, an alternative and solvent-free processing approach for fabricating fibers is via the melt. When accurate fiber placement is desired, one can utilize melt electrowriting (MEW) which gives excellent control over fiber placement. The enhanced control provided by MEW allows scaffolds to be directly written with defined structures and pore sizes.[20–24] Previously, a piezoelectric polymer (PVDF) was processed via MEW for the first time, with the fibers having increased β-phase content compared to the unprocessed powder.[25] To date, the copolymer P(VDF-*co*-TrFE) has been processed predominantly using solution electrospinning (SES) and film drawing. Both approaches require post-treatment to either remove toxic solvents, a

particularly pertinent step for biomedical applications, or to maximize the macroscopic polarization (β-phase) by applying an electrical field.[14]

This study investigates the processing of P(VDF-*co*-TrFE) using MEW and determines the printability of the copolymer with this technique. The influence of the high viscosity of the material on the MEW process and the resulting scaffolds is investigated. Furthermore, a heated collector was essential with the temperature found to affect the overall crystallinity and β-phase content in the fibers. A collector temperature of 120 °C, close to the Curie temperature of the polymer when heating, was found to improve crystallization and consequently led to a higher amount of β-phase. Interestingly, buckling of the fibers occurred when the collector temperature was reduced to room temperature.

4.3 Experimental

Materials

P(VDF-*co*-TrFE) (Solvene® 200/P200; 80 mol% VDF, 20 mol% TrFE; #900895) was purchased from Sigma Aldrich (Taufkirchen, Germany) and used as received. The melt flow index, as provided by the manufacturer, is 25 g (10 min)$^{-1}$ (ASTM D1238).

Melt electrowriting (MEW)

The MEW processing of P(VDF-*co*-TrFE) was performed with a custom-built device as previously described,[26] which operated at a nitrogen (N_2) pressure of 0.5 bar. A stainless steel nozzle was attached to a 3 mL glass syringe (Fortuna Optima 3 mL Luer Lock). The flat-tipped nozzle was prepared by grinding an injection cannula (22 gauge with Luer Lock, Carl Roth, Germany) to a length of 7.0 ± 0.2 mm. The print head and nozzle tip temperatures were set to a value of 170 ± 2 °C as reported by respective thermocouples. A potential difference of +3.70 ± 0.20 kV was applied between the nozzle and the grounded collector plate. MEW was maintained at a collector distance of 4.4 ± 0.5 mm, with 3.0 ± 0.2 mm of the nozzle protruding beyond the electrowriting head. A heated collector was custom-built as previously described26 and set to 120–135 ± 5 °C during printing. Glass microscope slides (VWR, ground edge, cat # 631-1550) were chosen as a printing substrate and were placed on top of the heated collector. The glass syringe was loaded with approximately 0.5 g of P(VDF-*co*-TrFE) and pre-heated for at least 30 min prior to printing. MEW processing was conducted at collector speeds between 10 and 100 mm/min.

X-ray diffraction (XRD)

XRD spectra were collected using a Bruker D8 Advance. The operating voltage and current used were 30 kV and 53.3 mA. The samples were irradiated with Cu Kα radiation using a step size of 0.045°, a dwell time of 0.7 s and a rotation of 15 r in the 2θ range 10°–80° with a low background sample holder made of a specially cut silicon single crystal. The raw powder and MEW-processed scaffolds printed with speeds of 50, 70 and 100 mm/min at two different collector temperatures (120 and 135 °C) were measured by placing them directly on the sample holder without further fixation. Background corrections and calculations on the measurements were done using a beam knife and the software DIFFRAC.TOPAS.

Imaging and videography

Stereomicroscope images were taken with a Discovery V20 (Carl Zeiss Microscopy GmbH, Germany). SEM imaging of the MEW processed fibers and scaffolds was performed with a Crossbeam 340 (Carl Zeiss Microscopy GmbH) instrument with all samples sputter-coated with approximately 3 nm of platinum (Leica EM ACE600). Videography was done using a Sony Alpha 7 and Nikon Z6 digital camera with Nikon ED 200 mm lens. Editing of the videos was performed using the software DaVinci Resolve 16.2.7.01.

Fiber diameter

A tabletop scanning electron microscope (TM3030p, Hitachi HighTech Corporation) was used to take images from three different samples with four printed single lines per collection speed, which was varied between 10 and 100 mm/min. These images were then used to measure the diameter with ImageJ (Version 1.52a, National Institutes of Health, USA) at around 50 different locations for at least three samples per collection speed. For the measurements of the top and bottom fibers, SEM images, of a scaffold with 10 layers in each direction, were taken at three different positions. Therefore, while imaging, the focus was set either on the bottom or the top layers and 15 different positions were measured within one image. In total three images of the bottom or top fibers were taken.

Atomic force microscopy (AFM) and piezo-force microscopy (PFM)

The morphological/electromechanical characterization of P(VDF-*co*-TrFE) fibers deposited onto indium tin oxide coated glass substrates at a collector speed of 90 mm/min and temperature of 120 °C was carried out by AFM and piezo-force microscopy (PFM). Measurements were done in contact mode by using a conductive diamond-coated probe with a nominal spring constant of 80 N m^{-1} (Bruker, USA) on a Bruker Dimension Icon system, equipped with a Nanoscope V controller. The surface roughness was calculated as the average of the root mean square values for areas of 25 μm^2 distributed along the fiber backbone.

4.4 Results

Fiber fabrication

The processability of the P(VDF-*co*-TrFE) via MEW was initially tested using parameters traditionally used for this technology; however, extruding P(VDF-*co*-TrFE) proved to be difficult compared to other polymers. Owing to the high viscosity of the polymer (melt flow index 25 g (10 min)$^{-1}$, ASTM D1238), a pressure greater than 1 bar was tested for polymer extrusion and jet initiation. However, it was observed that the pressurized gas would sometimes push through within the nozzle, resulting in poor extrusion. Following jet stabilization at high pressures, the oscillating jet (Video S1, 0.25× original speed) became electrostatically attracted towards the print head and led to jet breakup (Video S2, 1.5× original speed). Therefore, despite the high viscosity of the P(VDF-*co*-TrFE), a lower N_2 pressure of 0.5 ± 0.1 bar was selected for further experiments.

Further experiments revealed that, due to the rapid solidification of the polymer melt, the extruded material did not adhere to the collector and was dragged over the surface of the collector (Video S3), similar to what was previously observed for polypropylene.[26] This issue of jet dragging was solved using a collector heated to temperatures of 120–135 °C. P(VDF-*co*-TrFE) fibers were printed onto glass slides using two different collector temperatures. The resulting fibers were uniform and demonstrated good adherence to the collector substrate with the possibility to stack up to 20 alternating layers in 0°–90° orientation. Using SEM imaging for fiber morphology, it was revealed that fibrils are formed normal to the fiber orientation during the crystallization and solidification process of the polymer melt (Fig. 1). Similar results, showing extended grain growth and crystallization for SES fibers at annealing temperatures above 115 °C, were observed by Kim *et al*. [27] Melt electrospun polymers have also shown similar surface morphologies.[28]

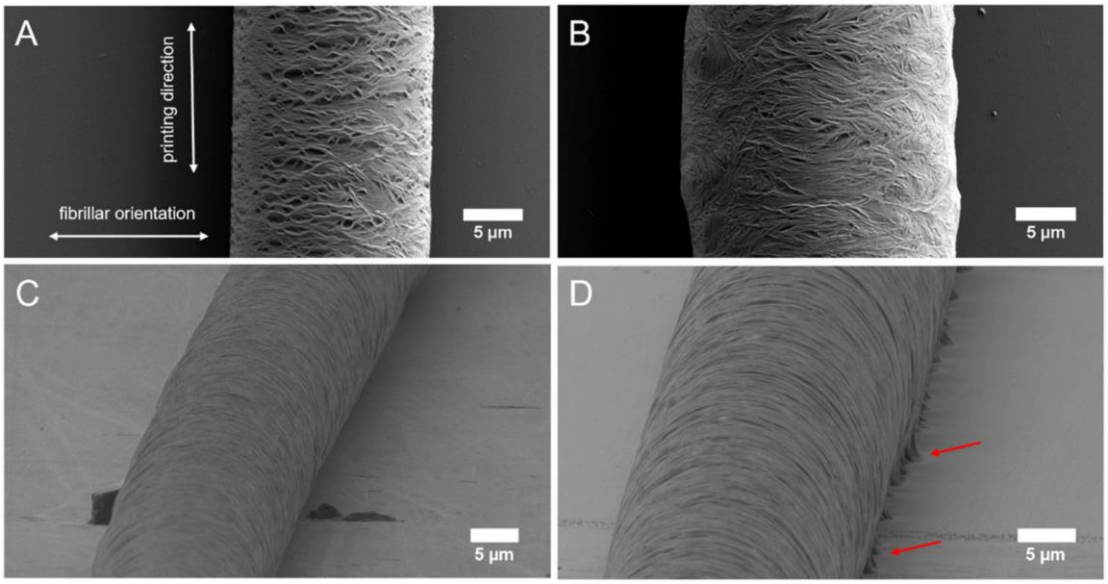

Figure 1. SEM images of fibers direct-written at 50 mm/min onto collectors heated at (A), (C) 120 °C and (B), (D) 135 °C. SEM images showing (A), (B) the top view of fibers depicting the printing direction and fibrillar orientation and (C), (D) the side view of the fibers. Fiber fusion and melting on the heated collector is highlighted by red arrows (D).

Using a collector temperature of 135 °C, the fibers start to show partial fusion and flattening onto the collector surface, consequently losing their circular shape (Fig. 1(D)). Removing the printed fibers and scaffolds from the glass slides without damage was challenging for the higher collector temperature of 135 °C, as the scaffolds adhered more to the glass surface. A lower collector temperature of 120 °C results in uniform and stable fibers that can be processed without noticeable flattening and can be detached without difficulties. Therefore, the use of a heated collector adds another adjustable instrument parameter for MEW of polymers where jet initiation is an issue due to non-adherence (Video S3). One of the notable outcomes of this study, in strong contrast to all other polymers processed to date using MEW, is the very low collector speed required for direct writing. Straight fibers, albeit with a larger 50 µm diameter, could be collected using collector speeds as low as 10 mm/min and it was difficult to determine a critical translation speed (CTS) where a transition between sinusoidal and linear deposition indicates the speed of the electrified jet.[24,29] Much higher CTS values were previously reported for other polymers including poly(*ε*-caprolactone) (300–750 mm/min),[24] urea-siloxane thermoplastic elastomers (1500– 3500 mm/min)[22] and poly(*ε*-caprolactone-*co*-acryloyl carbonate) (150–750 mm/min).[20] The lowest CTS value previously reported was for polypropylene (50–150 mm/min), which is also a polymer that requires a heated collector for direct writing.[26] This indicates that rapid cooling of the jet is probably responsible for the lack of a CTS in this instance. It was observed

that above a maximum collector speed of approximately 100 mm/min the molten jet readily ‘snapped’ and continuous direct writing could not be achieved. Clearly, MEW processing parameters for P(VDF-*co*-TrFE) differ rather significantly from all previously processed materials.

Thermal analysis of raw polymer and scaffolds was performed to study the effect of high processing temperatures on P(VDF-*co*-TrFE). TGA revealed that the mass of the P(VDF-*co*-TrFE) melt remains constant over the measured period of 5 h at 170 °C to simulate the conditions during the MEW process (Fig. S1(A)). A color change of the melt from colorless/transparent to yellow brown could be observed in line with that similarly observed for PVDF.[25] This color change may be attributed to low molar mass additives or unknown residues from the synthesis, rather than the polymer. At higher temperatures around 300 °C, TGA shows a significant reduction in the mass representing the onset of degradation of polymer. In the DSC measurements (Fig. S1(B)) both the polymer and the scaffolds showed the same peaks in the second heating cycle suggesting no change in the polymer due to MEW processing. The cooling curves from DSC (Fig. S1(B)) showed a Curie transition around approximately 75–80 °C for both powder and MEW scaffolds. This Curie transition is lower for the cooling of the P(VDF-*co*-TrFE) compared to the Curie transition measured upon heating (135 °C) of the polymer. At the Curie temperature a transition from the ferroelectric to paraelectric phase is taking place.[30,31]

Effect of collector speed on fiber diameter

To investigate the influence of the collector speed on the crystallization process and fiber diameter, it was varied from 10 to 100 mm/min in 10 mm/min increments at the aforementioned collector temperatures of 120 ± 5 °C and 135 ± 5 °C. The resulting fibers were imaged by SEM (Fig. 2). Increasing the collector speed results in a decrease of the fiber diameter for both collector temperatures. Above 30 mm/min, the decrease in fiber diameter levels off at around 15 µm for both collector temperatures (Fig. S2(A)). A similar behavior has been described previously for poly(*ε*-caprolactone).[32]

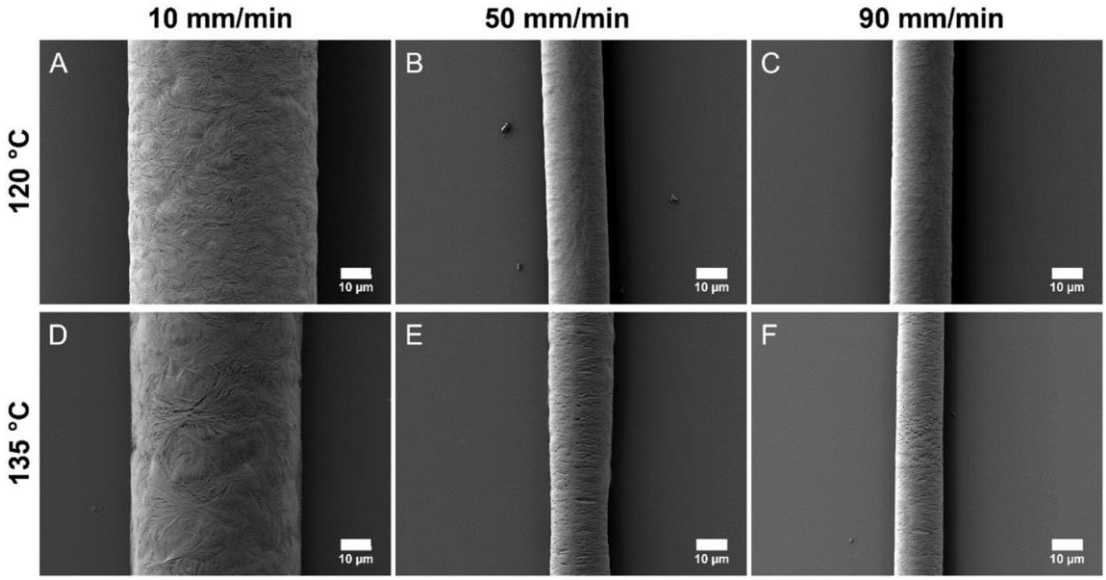

Figure 2. (A)–(F) SEM images of MEW-processed fibers printed at varying speeds (10, 50 and 90 mm/min) and two different collector temperatures (120 and 135 °C).

SEM images also showed differences in the formation of crystalline domains with varying fiber diameters. The change in the fiber morphology depending on the collector speed can be attributed to changes in collector temperature and cooling behavior of the jet. A change in the fiber morphology depending on the annealing temperature has been reported in the literature.[27] The fiber morphology can be related to grain growth and crystallization[27] and might be explained by a phase transition from the α-phase into the piezoelectric, all-trans zig-zag β-phase. This phase transformation has been previously described by different groups[33– 35] as a transformation from a spherulitic to a microfibrillar structure and can be induced by stretching of the molten jet. The radial spherulitic structure is visible on MEW fibers directly written with a collector speed of 10 mm/min (Figs 2(A), 2(D)) and transforms into different surface morphologies with increasing collector speed (Figs 2(B), 2(C), 2(E), 2(F) and in magnified view in Fig. 1). Those surface morphologies could be caused by the stretching of the jet into a fibrillar structure from crystallites.[33,35] Furthermore, the collector speed influenced the jet lag of the polymer melt[24,36] (Video S4; speed of the videos was adjusted to match the print duration of 10 mm/min prints) and might lead to different cooling rates of the printed fibers, which in turn influence the crystallinity of the fibers. As previously observed for MEW processed fibers, changes in the surface morphology can also originate from disparities in the solidification rates of the fiber surface and core.[37] It is known that, with increasing collector speeds, the electrified jet is increasingly stretched.[24,36]

Layer stacking behavior

With the direct-writing parameters for single fibers established, the fabrication of multi-layered 0–90° scaffolds, at 500 µm hatch spacing, with up to 10 alternating layers was investigated. Notably, and never reported before for MEW, printing more than three stacked layers on top of each other resulted in the formation of sinusoidal structures in between the crossing points, when cooling the collector to room temperature after printing (Fig. 3).

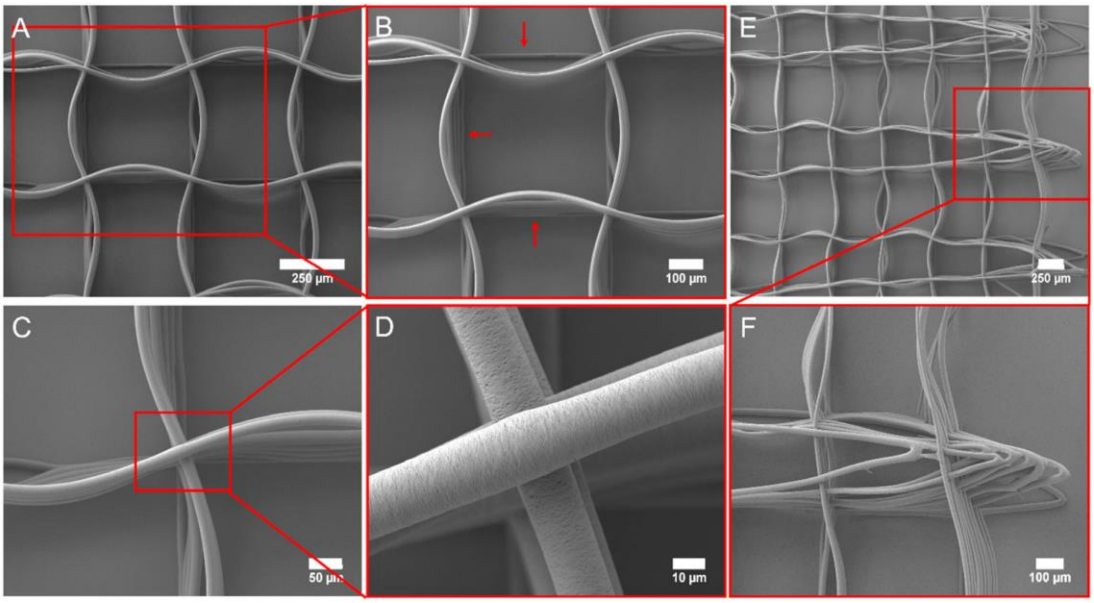

Figure 3. SEM images of a 0/90° scaffold: (A), (B) the box structure. Red arrows indicate the first three fibers deposited, which remain straight, unlike the sinusoidal nature of the higher layers. SEM images of (C), (D) the crossing points and (E), (F) the turns. (B), (C) and (F) show magnified views.

This phenomenon was studied for the two different collector temperatures, different collector speeds and scaffolds with 0–90° and 0–45° fiber orientation. The collector temperature while printing seems not to have any significant influence on the formation of sinusoidal fibers; only the collector temperature while cooling appears to impact this phenomenon (Video S5).

The sinusoidal formation starts to appear when the collector temperature reaches about 70–80 °C at the glass slide and 80– 90 °C for the set temperature of the heated collector (Video S5) and therefore could be connected to the Curie transition temperature during cooling as judged from the DSC thermograms (Fig. S1(B)). These structural variations could be due to changes in the recrystallization process during solidification and residual thermal strain, which are known to be highly dependent on the cooling rate.[37] However, the first two to three layers always stay straight independent of the collector speed or the collector temperature,

probably due to increased adherence to the collector and to the underlying layers (red arrows, Fig. 3(B)).

When measuring the fiber diameter of the top and bottom layers of the scaffold (Fig. S2(B)), no significant decrease or increase was observed. When inspecting the turns of the lines within the scaffolds (Figs 3(E), 3(F)), the jet lag is pulling the fibers at the turns inwards, as previously observed for radial structures printed using medical-grade poly(ε-caprolactone).[38] Therefore, the position of the fiber changes with the number of layers when the directing of writing is substantially changing.

Furthermore, fabricated P(VDF-*co*-TrFE) scaffolds with 20 alternating layers at 0° and 90° showed the solidified fiber breaking in between the scaffolds at various locations. The breakage of the fiber could be due to (i) the jet breaking or (ii) mechanical forces associated with fiber bending while cooling. Figures 4(A) and 4(B) show an overview of a 20-layer P(VDF-*co*-TrFE) scaffold printed with a speed of 70 mm/min and a collector temperature of 120 °C. At various locations one or more fibers are snapped, indicated with red arrows (Figs 4(A), 4(B)); however, a clear trend in where and when the fibers were breaking could not be determined. It seems that the fibers break probably due to rapid temperature changes, for example when removing the glass slides from the heated collector temperature (120–135 °C) to a surface at room temperature.

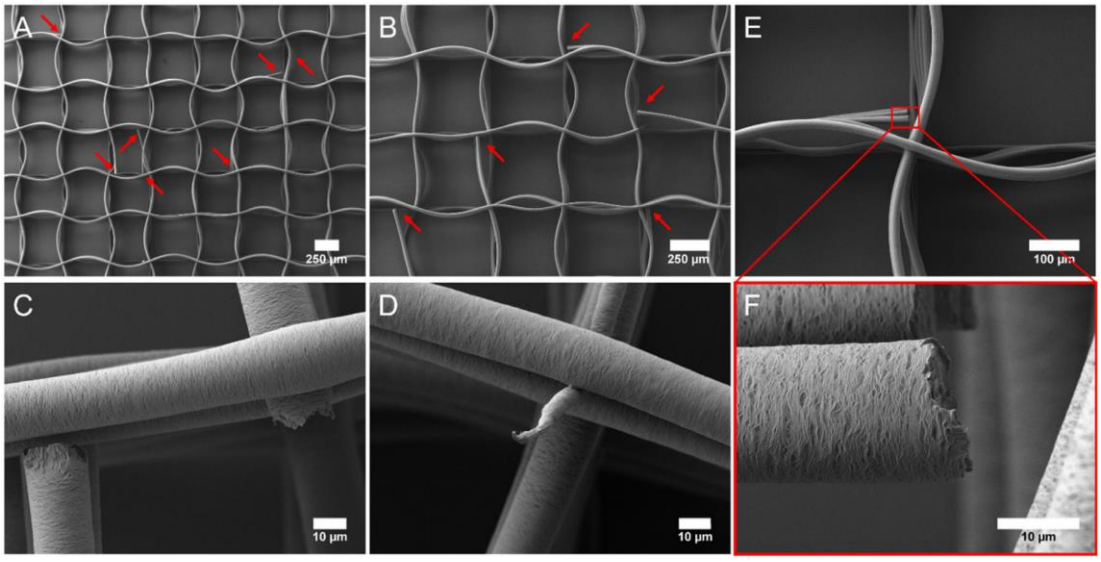

Figure 4. SEM images of 20 alternating layers with broken fibers and fiber bundle. (A), (B) Box structured scaffold with red arrows indicating brittle fractures. Magnified SEM images highlighting the differences between (C) a brittle fracture due to the bending/cooling crystallization process and (D) a snapped fiber caused by jet break-up. (E) Sharp breaks resulting in fiber bundles; (F) a magnified view.

Another indication of fibers breaking post-solidification is that the broken fiber bundles remain at their position within the scaffold (Figs 4(C) and 4(E-F)). In

comparison, the point of break within a jet break-up in the polymer melt is stretched and pulled until the jet snaps, resembling ductile failure behavior (Fig. 4(D)).

XRD measurements, crystallinity and β-phase content

The corresponding XRD measurements for the raw powder and the scaffolds printed at collector temperatures of 120 and 135 ° C are displayed in Fig. 5.

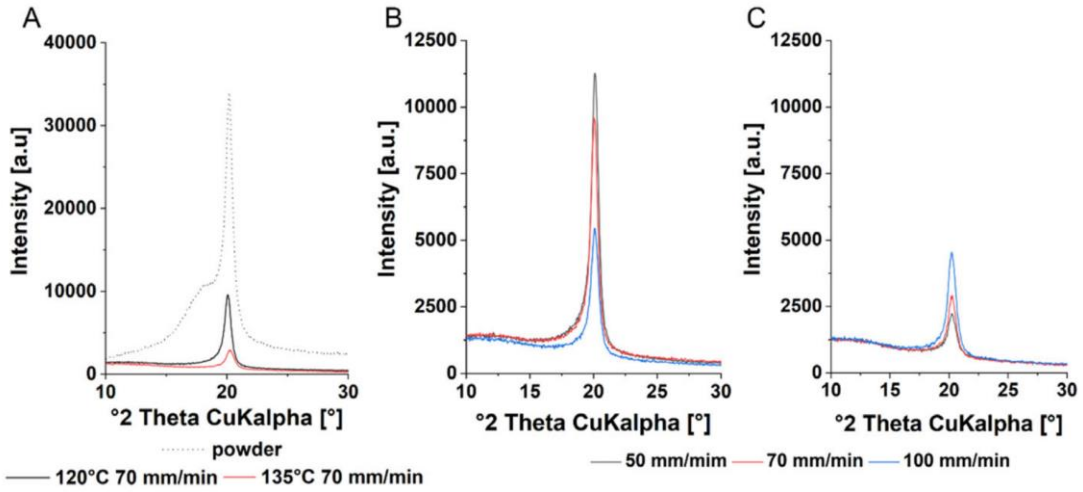

Figure 5. X-ray diffractogram showing (A) the raw P(VDF-*co*-TrFE) powder (dashed line) compared to scaffolds printed with 70 mm/min at collector temperatures of 120 °C (black line) and 135 °C (red line). MEW scaffolds fabricated with speeds of 50 mm/min (black line), 70 mm/min (red line) and 100 mm/min (blue line) at collector temperatures of (B) 120 °C and (C) 135 °C.

For the unprocessed P(VDF-*co*-TrFE) powder, a clearly visible shoulder peak can be seen at 18° and a peak at 20°, respectively, which can be attributed to the polar β-phase (110 and 200), as described previously for SES fibers.[6,27] For all MEW-processed scaffolds the shoulder peak at 18°, attributed to the α-phase, disappeared or reduced significantly. Comparing the measurements in Fig. 5(B), the peak at 20° is broader for the scaffolds printed with 50 and 70 mm/min. A similar broader peak can be seen at the collector temperature of 135 °C for the scaffold printed with 100 mm/min (Fig. 5(C)). Therefore, MEW processing of the raw powder seems to decrease the α-phase, as previously observed for SES fibers due to the *in-situ* poling and stretching while electrospinning.[6,15,27] However, as shown in Fig. 5(A), the intensity of the peaks is lower for the MEW-processed scaffolds compared to the unprocessed powder. For the scaffolds printed at 120 °C, the absolute intensity is lower compared to that of the unprocessed powder and higher compared to the scaffolds printed at 135 °C. Here, it needs to be mentioned that the XRD measurements were performed on MEW-fabricated scaffolds with high porosity

compared to a filled-up powder sample holder resulting in different intensities within the diffractogram measured for the samples.

From the XRD results, the ratio between α- and β-phase for the MEW-processed scaffolds printed at both collector temperatures can be calculated (Fig. S3 and Table S1). The background of the sample holder and crystalline phases within the XRD measurements of the unprocessed powder and MEW-fabricated scaffolds has been separated and the crystalline part was used for further investigations. Furthermore, the peaks of the crystalline region were separated into areas corresponding to the α- and β-phases as described in Fig. S3. A similar approach also using a multi-peaks fitting technique has previously been utilized based on DSC measurements.[39]

For both collector temperatures, the ratio between α- and β-phase content changed with β-phase contents at around 85% to 90% for the MEW-processed scaffolds. For the samples printed at the higher collector temperature with speeds of 50 and 70 mm/min the β-phase content is around 90%; however, the total crystallinity is significantly less compared to the samples printed at a collector temperature of 120 °C (Table S1 and Fig. 5). Therefore, MEW processing of the P(VDF-*co*-TrFE) with a heated collector can be seen as an *in situ* annealing process and annealing temperatures close to the Curie temperature can provide sufficient energy for chain reorientation and therefore can lead to an increase in β-phase formation compared to unprocessed material.[27]

Using the set temperature and the actual measured collector temperatures, we were able to quantify the cooling rates with a slightly faster cooling rate for the 135 °C collector temperature. Therefore, the collector with the set temperature of 135 °C might lead to a decrease in crystallinity, as it is known that crystallinity is highly dependent on the cooling rate and a fast cooling rate can lead to a lower crystallinity.[40,41]

These β-phase contents are within the range of values shown in the literature for differently treated films resulting in β-phase fractions of 66.33% to 100% using P(VDF-*co*-TrFE) (75/25)[42] or P(VDF-*co*-TrFE) (80/20).[39] Furthermore, SES fibers result in values around 85% P(VDF-*co*-TrFE) (75/25) depending on the fiber orientation[6] and 88% β-phase using P(VDF-*co*-TrFE) (70/30).[43] Those findings together with the results of the MEW-processed fibers in this study indicate the high impact of the TrFE content, as well as the applied electric field, which is in general higher for SES and/or the fabrication process (melt- or solvent-based), on the resulting β-phase fractions and the overall crystallinity.

Jet behavior

Rapid cooling of the polymer was believed to be the reason for dragging of the polymer jet on the collector as discussed above. This issue was simply circumvented by using a heated collector. Another interesting phenomenon shown for the copolymer jet is the oscillating/vibrating behavior as depicted in Video S1. The balance between the amount of polymer and voltage applied was found to be the key to laying down fibers consistently for long durations. As the pressure was increased, the jet was readily attracted towards the head (Video S2) and disrupted the jetting process. The collector temperature of 120 °C and the applied voltage were not sufficient to attract the jet and initiate the process of MEW.

The formation of a stable jet while printing is highly dependent on the processing parameters, especially the speed of the collector.[24,44,45] For other already established MEW-processable polymers, the CTS is a very important value and is sensitive to small changes in the processing parameters. The jet at speeds just above the CTS typically starts with a nearly vertical line and then increases the lag significantly until the lag seems to level off,[45] which can be related to the fiber diameter discussed previously. For the P(VDF-*co*-TrFE) a similar behavior was observed; however, no CTS was found, and the processed fibers resulted in straight and uniform lines even at significantly low speeds of 10 mm/min. Looking at the jet lag of the P(VDF-*co*-TrFE), within the processable speed range from 10 to 100 mm/min, an increase in the jet lag depending on the collector speed was detected and the jet lag seems to level off at 50 mm/min and higher (Video S4).

Morphological and piezoelectric characterization

The piezoelectric response of the MEW-processed fiber was measured by PFM upon the application of an alternating (AC) voltage with a frequency of 15 kHz (Fig. 6).

The measured fiber was deposited onto an indium tin oxide coated glass substrate at a collector speed of 90 mm/min and a temperature of 120 °C. The fiber diameter, taking into account a deconvolution of the profile of the AFM tip used, is 16 µm and the surface roughness along the fiber backbone is of the order of 100 nm. Upon the application of an AC bias of 10 V between the tip and the sample, the PFM amplitude signal indicates a strain response of tens of picometers, which is higher along the fiber backbone (Figs 6(C), 6(F)) highlighting a surface pattern that can be correlated with a local enhancement of the vertical component of the polarization vector in certain crystalline domains.

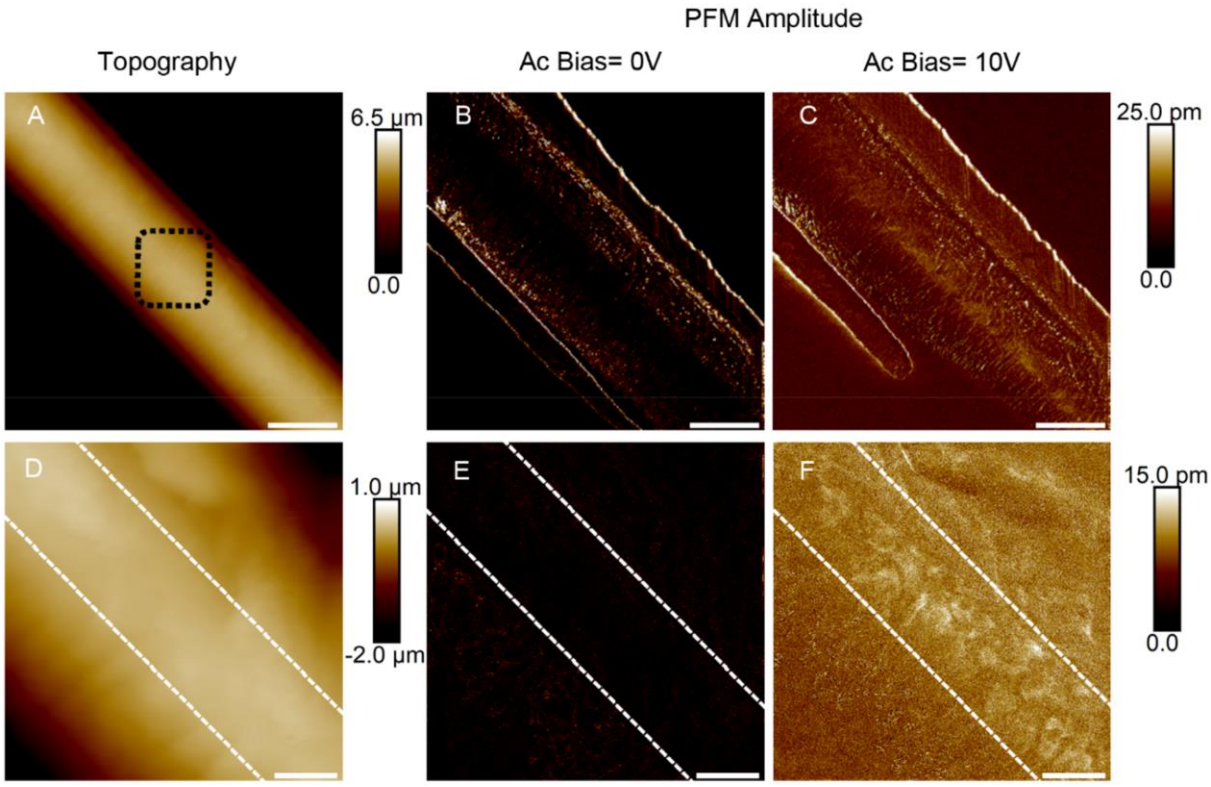

Figure 6. (A) AFM topographic images and corresponding PFM images of a P(VDF-*co*-TrFE) fiber at an AC bias voltage of (B) 0 V and (C) 10 V. (A)–(C) Scale bars 10 µm. (D)–(F) High magnification images of (A)–(C) measured in the area of the fiber highlighted by the black box in (A). The dashed white lines highlight the fiber backbone. (D)–(F) Scale bars 2 µm.

In contrast, the amplitude of the in-plane oscillation that was measured by lateral PFM indicates an almost uniform distribution of the in-plane piezo response (Fig. S4), suggesting different dynamics of crystallization and solidification along the fiber backbone. Changes in the PFM amplitude signal were measured for AC bias in the interval 2–10 V, leading to a linear dependence between the piezo response and the applied voltage typical of piezoelectricity (Fig. S5(A)). Dipoles are sensitive to the direction of the applied field and exhibit a phase shift when the external bias is inverted (i.e. the positive bias is applied to the sample and the tip is grounded) as reported in Figs S5(B) and S5(C).

4.5 Conclusion

In this study, an important piezoelectric polymer, P(VDF-*co*-TrFE), was shown to be processable via MEW into fibers ranging between 10 and 50 µm, depending on the collector speed. The direct writing had to be performed at remarkably low speeds of less than 100 mm/min while a heated collector was essential to initiate the direct writing. Upon cooling of the collector, straight fibers formed sinusoidal structures which were correlated to a change in the macromolecular orientation within the recrystallization process, in turn influenced by the collector temperature and speed. The resulting MEW-processed fibers showed a decrease in α-phase and an increase in the piezoelectric β-phase content of up to 85%–90% compared to the unprocessed powder even though the total crystallinity did not increase. The electroactive nature of this polymer was proven by PFM measurements and makes this study relevant to applications where well-resolved 3D printed structures of such piezoelectric polymers are of interest, such as biomedical products due to the absence of toxic solvents compared to other processing techniques, as well as energy harvesting, actuators and sensors.

4.6 Acknowledgements

We gratefully acknowledge financial support by the Volkswagen Foundation (grant number 93418), the Italian Minister of Research through the PRIN 20173L7W8K and 2017PHRM8X projects. J.C.K. is supported by the Joachim Herz Foundation. The technical assistance of Philipp Stahlhut and Judith Friedlein for SEM imaging is appreciated while the Zeiss Crossbeam CB 340 SEM was funded by the German Research Foundation (DFG) State Major Instrumentation Program (INST 105022/58-1 FUGG). Furthermore, we thank Dr Tomasz Jüngst for providing the camera and Michael Bartolf-Kopp for his input and help for the supporting videos. Proofreading by Professor Dr Uwe Gbureck is greatly appreciated.

4.7 References

[1] Rajabi AH, Jaffe M and Arinzeh TL, Acta Biomater 24:12–23 (2015).

[2] Zaszczynska A, Sajkiewicz P and Gradys A, Polymers 12:161 (2020).

[3] Palza H, Zapata PA and Angulo-Pineda C, Materials 12:277 (2019).

[4] Ribeiro C, Sencadas V, Correia DM and Lanceros-Méndez S, Colloids Surf B Biointerfaces 136:46–55 (2015).

[5] Liu X, Wang X, Zhao H and Du Y, J Phys Conf Ser 557:012057 (2014).

[6] Persano L, Dagdeviren C, Su Y, Zhang Y, Girardo S, Pisignano D et al., Nat Commun 4:1633 (2013).

[7] Wu S, Chen M-S, Maurel P, Lee Y-s, Bunge MB and Arinzeh TL, J Neural Eng 15:056010 (2018).

[8] Zaarour B, Zhu L, Huang C and Jin X, J Appl Polym Sci 136:47049 (2019).

[9] Ribeiro C, Costa CM, Correia DM, Nunes-Pereira J, Oliveira J, Martins P et al., Nat Protoc 13:681–704 (2018).

[10] Foster FS, Harasiewicz KA and Sherar MD, IEEE Trans Ultrason Ferroelectr Freq Control 47:1363–1371 (2000).

[11] Martins P, Lopes AC and Lanceros-Mendez S, Prog Polym Sci 39:683– 706 (2014).

[12] Haque RI, Vié R, Germainy M, Valbin L, Benaben P and Boddaert X, Flex Print Electron 1:015001 (2015).

[13] Wan C and Bowen CR, J Mater Chem A 5:3091–3128 (2017).

[14] Hafner J, Teuschel M, Schneider M and Schmid U, Polymer 170:1–6 (2019).

[15] Damaraju SM, Shen Y, Elele E, Khusid B, Eshghinejad A, Li J et al., Biomaterials 149:51–62 (2017).

[16] Damaraju SM, Wu S, Jaffe M and Arinzeh TL, Biomed Mater 8:045007 (2013).

[17] Lee Y-S and Arinzeh TL, Tissue Eng Part A 18:2063–2072 (2012).

[18] Lee Y-S, Collins G and Livingston Arinzeh T, Acta Biomater 7:3877–3886 (2011).

[19] Weber N, Lee YS, Shanmugasundaram S, Jaffe M and Arinzeh TL, Acta Biomater 6:3550–3556 (2010).

[20] Hochleitner G, Chen F, Blum C, Dalton PD, Amsden B and Groll J, Acta Biomater 72:110–120 (2018).

[21] Castilho M, van Mil A, Maher M, Metz CHG, Hochleitner G, Groll J et al., Adv Funct Mater 28:1803151 (2018).

[22] Hochleitner G, Fürsattel E, Giesa R, Groll J, Schmidt H-W and Dalton PD, Macromol Rapid Commun 39:1800055 (2018).

[23] Hochleitner G, Jüngst T, Brown TD, Hahn K, Moseke C, Jakob F et al., Biofabrication 7:035002 (2015).
[24] Hrynevich A, Elci BS, Haigh JN, McMaster R, Youssef A, Blum C et al., Small 14:e1800232 (2018).
[25] Florczak S, Lorson T, Zheng T, Mrlik M, Hutmacher DW, Higgins MJ et al., Polym Int 68:735–745 (2019).
[26] Haigh JN, Dargaville TR and Dalton PD, Mater Sci Eng C 77:883–887 (2017).
[27] Kim M, Lee S and Kim Y-i, APL Mater 8:071109 (2020).
[28] Dalton PD, Grafahrend D, Klinkhammer K, Klee D and Moller M, Polymer 48:6823–6833 (2007).
[29] Dalton PD, Curr Opin Biomed Eng 2:49–57 (2017).
[30] Meng N, Zhu X, Mao R, Reece MJ and Bilotti E, J Mater Chem C 5:3296– 3305 (2017).
[31] Furukawa T, Johnson GE, Bair HE, Tajitsu Y, Chiba A and Fukada E, Ferroelectrics 32:61–67 (1981).
[32] Brown TD, Dalton PD and Hutmacher DW, Adv Mater 23:5651–5657 (2011).
[33] Gomes J, Serrado Nunes J, Sencadas V and Lanceros-Mendez S, Smart Mater Struct 19:065010 (2010).
[34] Lando JB and Doll WW, J Macromol Sci B 2:205–218 (1968).
[35] Sencadas V, Gregorio R and Lanceros-Méndez S, J Macromol Sci B 48: 514–525 (2009).
[36] Liashenko I, Hrynevich A and Dalton PD, Adv Mater 32:2001874 (2020).
[37] Uribe-Gomez J, Posada-Murcia A, Shukla A, Ergin M, Constante G, Apsite I et al., ACS Appl Bio Mater 4:1720–1730 (2021).
[38] Bakirci E, Schaefer N, Dahri O, Hrynevich A, Strissel P, Strick R et al., Adv Biosyst 4:2000077 (2020).
[39] Zhang Q, Xia W, Zhu Z and Zhang Z, J Appl Polym Sci 127:3002–3008 (2013).
[40] Schawe JEK, J Appl Polym Sci 133:42977 (2016).
[41] Fischer C and Drummer D, Int J Polym Sci 2016:5450708 (2016).
[42] Bae J-H and Chang S-H, Compos Struct 131:1090–1098 (2015).
[43] Orkwis JA, Wolf AK, Shahid SM, Smith C, Esfandiari L and Harris GM, Macromol Biosci 20:2000197 (2020).
[44] Wunner FM, Mieszczanek P, Bas O, Eggert S, Maartens J, Dalton PD et al., Biofabrication 11:025004 (2019).
[45] Hrynevich A, Liashenko I and Dalton PD, Adv Mater Technol 5:2000772. (2020)

Chapter 5

– Establishing a Coaxial Melt Electrowriting System

Chapter 5 is written in the style of a manuscript. This chapter was thoroughly written by the author of this thesis Juliane C. Kade, who conceived the research, performed all experiments and data evaluation.

5.1 Abstract

In this study, a custom-built melt electrowriting printer has been adapted with a coaxial nozzle and print-head setup. Dual material scaffolds with either *Janus*- or coaxial fibers, have been investigated and established. Both polymers used in this study are based on poly(*ε*-caprolactone) (PCL). For the shell neat PCL was used and for the core PCL containing 30 wt.% carbonyl iron (CI) particles enabling a visual difference between the core and shell given by the colors of the polymers used. The influence of the printing parameters like collector speed and applied pressure were studied and the resulting fibers had diameters ranging from 30 to 180 µm. Furthermore, the influence of the core diameter on the flow rates of the shell has been investigated for two different core nozzles. Within this study, the potential for a coaxial melt electrowriting system has been established, however, further adjustments regarding the nozzle alignment needs to be done in future.

5.2 Introduction

Additive manufacturing (AM) is a field of increasing interest with fast developing methods as well as materials. One method, melt electrowriting (MEW), is a high-resolution 3D printing method based on an electrohydrodynamic principle leading to the stabilization and thinning of a polymer melt jet. It allows to direct write fibers with resulting diameters between 5 to 50 µm. However, the number of processable materials is still limited despite being expanded upon within the last five years. Additionally, more and more studies are investigating and improving printing parameters, as well as the printer themselves, to enhance the MEW-process and the resulting constructs.

One example has been published in 2021 by Eberle *et al*.[1] when printing a coaxial MEW nozzle by using a selective laser melting (SLM) printer. The coaxial nozzle was used to process hollow fibers by forming air bubbles within medical-grade poly(*ε*-caprolactone) (PCL). This is the first time a coaxial nozzle system has been used for MEW resulting in hollow PCL fibers.[1]

Other techniques such as solution electrospinning (SES) or bioprinting have processed a wide range of material combinations by using a coaxial nozzle setup allowing to combine different materials within one fiber. This opens the possibility to embed specific properties within the materials for example as drug-loaded matrices for pharmaceutical release profiles.

In this study, we established a coaxial MEW system based on a custom-made print-head and nozzle setup design allowing to MEW-process two materials within one fiber. The resulting fibers are based on the current gold standard material used for MEW, namely PCL. Neat PCL has been used as the shell material and PCL containing 30 wt.% carbonyl iron (CI) particles in the core resulting in grey to black fibers with magnetic properties due to the CI particles. The processed fibers were investigated regarding the resulting fiber diameters of the total fiber and the core and different printing parameters have been studied. Furthermore, using scanning electron microscopy (SEM) visualized the fabricated fibers, as well as the core and shell material.

5.3 Materials and methods

5.3.1 Materials

Medical grade PCL was sourced from Corbion Inc. (PURASORB PC 12, Gorinchem, Netherlands) and PCL containing CI particles was kindly provided by Miroslav Mirlik (Centre of Polymer Systems, Tomas Bata University in Zlin, Czech Republic) and used as received with a particle content of 30 wt.%.

5.3.2 Methods

Coaxial MEW printer setup

A custom-built MEW printer, as previously described,[2] was used for all experiments. Briefly, the movement of the collector in X- and Y-direction by linear stages was controlled via G-code and operated by the CNC software (Bosch Rexroth AG, Lohr am Main, Germany). Movement in Z-direction was enabled by moving the print head controlled by G-code. The print head was designed and engineered by Andrei Hrynevich and Harald Hümpfer and is shown in Figure 1. Both print heads, the core and the shell, were equipped with two electrical heaters connected to the polymer reservoir within the syringe, as well as the nozzle, respectively. The polymers were loaded into glass syringes (FORTUNA Optima, Poulten & Graf GmbH, Wertheim, Germany) using a 2 mL syringe for the core and a 3 mL syringe for the shell. Furthermore, both print heads were connected to a controllable air pressure system (Aventics, Germany) and the core-shell nozzle was connected to a high voltage (HCP 140-20000, FuG Elektronik GmbH, Schechen, Germany).

Coaxial MEW printing

The printing parameters used are listed in Table 1 summarizing the conditions for the core and the shell.

Table 1. Printing parameters for the coaxial MEW setup processing neat PCL as the shell and PCL containing 30 wt.% CI particles as the core.

	pressure [bar]	temperature syringe [°C]	temperature nozzle [°C]	voltage nozzle tip [kV]	voltage collector [kV]	distance [mm]
22G core nozzle						
shell	1.5 – 3.0	85	85	+5.5	-2.5	4
core	0.1 – 0.75	80	80			
30G core nozzle						
shell	0.1 – 0.75	85	85	+5.5	-2.5	4
core	1.5 – 3.0	80	80			

Flow rates

Flow rates at different pressures were investigated using a G-code kindly provided by Biranche Tandon. The code was programmed to print a short stabilization before starting to print a spiral at constant speed. The code was running for 30 minutes and then stopped to collect the processed fibers. The sample was then weighted using a balance (Mettler Toledo XPE26 Delta Range, Columbus, USA). For each pressure at least n=3 samples were printed and measured.

Imaging

To analyze MEW-processed fibers a stereomicroscope (Discovery V20, Carl Zeiss Microscopy GmbH, Göttingen, Germany) was used for imaging.

SEM imaging, as well as EDX and FIB.

A crossbeam 340 SEM equipped with GEMINI e-Beam column (Carl Zeiss Microscopy GmbH) was used to get a closer look on the fiber morphology. Prior to SEM imaging, all samples were sputter coated with a 4 nm layer of platinum using a sputter coater (Leica EM ACE600, Wetzlar, Germany).

In situ cutting of the fibers was carried out using a focused ion beam (FIB). Energy dispersive X-ray spectroscopy (EDX) were conducted on 4 nm platinum sputter-coated composite fibers.

Graphics Interchange Format (GIF) animation

A set of SEM images was taken by Philipp Stahlhut. The images were combined as a GIF animation using Adope Photoshop software (Version 13.0).

Fiber diameter

To investigate the influence of the applied pressures onto the total fiber diameter and the core diameter straight lines in sets of six lines per printing speed, were processed with at least n=3 samples per applied pressure set. The printing speeds were changed in the range of 50 to 250 mm/min in increments of 50 mm/min. The resulting fibers were imaged using the stereomicroscope and measured via ZEN software (3.4.91.00000, Carl Zeiss Microscopy GmbH, Oberkochen, Germany).

5.4 Results and discussion

5.4.1 Coaxial MEW printer setup

The MEW processing of the PCL-based materials was carried out on a custom-built MEW device as previously described elsewhere.[2] To enable coaxial MEW-processing, the print-head of the device has been changed and modified, as well as the nozzle setup to provide a double material supply connected via a custom-made coaxial nozzle setup. The design and setup of the print-head and the nozzle is shown in Figure 1.

The coaxial print-head consits of two individual print-heads for the core and the shell material allowing to adjust the temperatures for the nozzle and the syringe individually, as well as the applied synthetic air pressure. The two material reservoirs within the glass syringes where connected via a coaxial nozzle setup with a fixed shell nozzle diameter given by the design of the nozzle (Figure 1). The core nozzle was connected to the core syringe enabling changes of the nozzle tip, as well as the core material while maintaining the same shell material, without disasambling the whole coaxial print-head.

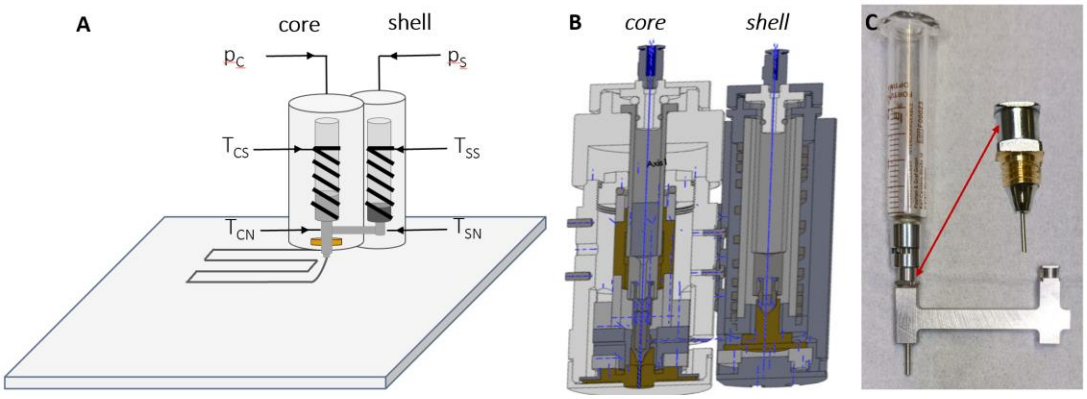

Figure 1. Custom-made coaxial MEW printer A) showing a schemtic presentation, B) the CAD file of the print-head and C) the nozzle setup with fixed shell nozzle and changeable core nozzle. CAD image kindly provided by Harald Hümpfer and Andrei Hrynevich.

While coaxial fibers have been reported for SES, only one study has recently proven the production of a hollow fiber using a 3D printed coaxial nozzle by using melt electrowriting as 3D printing technique.[1] Therefore, the here mentioned results are the first coaxial MEW fibers using two different materials within one fiber.

5.4.2 Coaxial MEW

The coaxial MEW setup was established using neat PCL as the shell material and PCL containing 30 wt.% of CI particles as the core material. Those materials were choosen due to their similar processing temperatures. Furthermore, the CI

particles embedded within the PCL resulted in grey to black fibers helping to easily visualize the core material within the shell using microscopy.

The first prints showed promising dual material fibers, however, the core material was not idealy aligned in-between the shell material resulting in alternating, so called *Janus* fibers. Furthermore, the nature of the coaxial fibers depend on the printing direction (Figure 2). This limitation might be due to a slightly bent core nozzle tip, when manually grinding to the lenth needed or when inserting the tip into the nozzle setup, resulting in a not perfectly centered core within the shell.

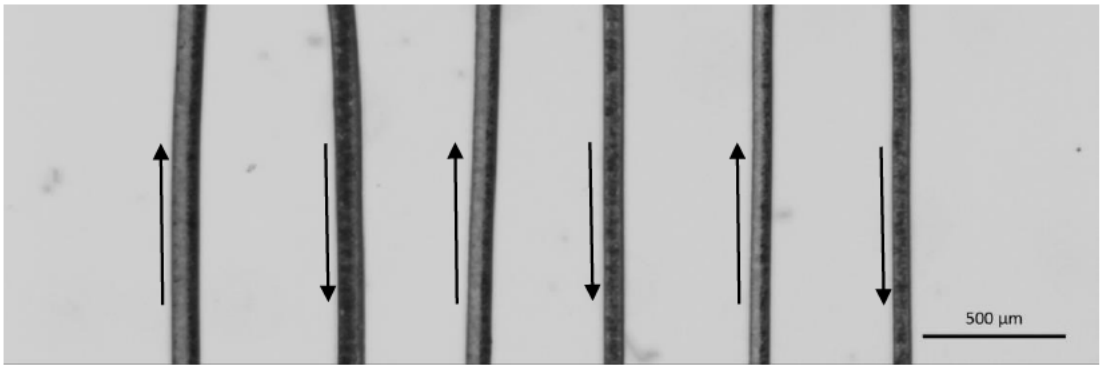

Figure 2. 22G core nozzle; shell 1.5 bar, core 0.1 bar, 100 mm/min. Arrows indicating the printing direction.

5.4.3 Fiber diameters at different applied pressures

5.4.3.1 MEW with a 22G core nozzle

For the coaxial MEW setup, based on PCL and PCL containing 30 wt.% CI particles, a 16G shell nozzle and a 22G core nozzle were used. To investigate the resulting fiber diameters, as well as the ratios of the two materials, the applied shell pressure was set constant to 1.5, 2.0, 2.5 or 3.0 bar and the core pressure was investigated for 0.1, 0.5 and 0.75 bar. Additionally, a range of printing speeds from 50 to 250 mm/min with 50 mm/min increments was tested for each pressure combination.

In Figure 3 the resulting total fiber diameter (16G nozzle), as well as the core diameter using a 22G nozzle tip are listed. In general, the total fiber diameter are quite large between 100 to 150 µm for most of the applied pressures, which is probably caused by the large nozzle diamater, as the most common nozzle sizes processing PCL are between 21 to 30G.[3, 4] The resulting MEW fibers using PCL are commonly in the range of 5 to 50 µm depending on the nozzle tip used, as well as the other printing parameters like printing speed, applied pressure and voltage.[4, 5]

By increasing the printing speed, the total fiber diameter was generally reduced for all tested printing setting, but interestingly, the core diameter stayed relative constant when increasing the printing speed. Especially for the speeds between 150 to 250 mm/min it was not possible to detect any neat PCL as the shell, when checking under the microscope. Therefore, the resulting total fiber diameter is the core diameter, as for example at a applied shell pressure of 1.5 bar and 0.5 and 0.75 bar for the inner material.

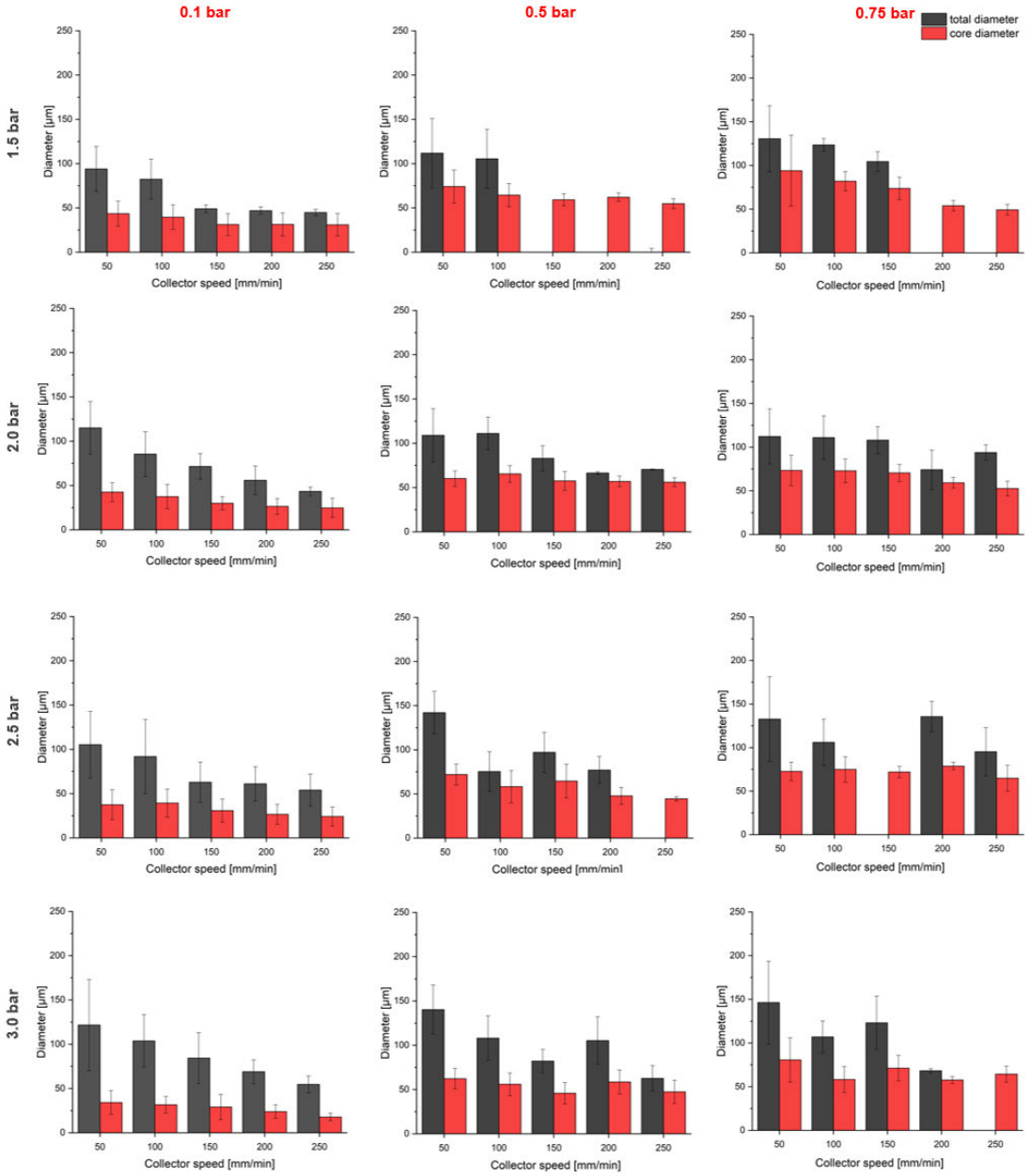

Figure 3. Fiber diameter ratios of coaxial fibers using a 16G nozzle tip as the shell and a 22G nozzle tip as the core. Applied shell pressures were varied from 1.5, 2.0, 2.5 and 3.0 bar and core pressures between 0.1, 0.5 and 0.75 bar. The resulting total fiber diameter is indicated in dark grey and the core diameter in red for printing speeds between 50 to 250 mm/min increased in increments of 50 mm/min.

5.4.3.2 MEW with a 30G core nozzle

To reduce the amount of core material, as well as to hopefully better aligne it within the shell, the core nozzle has been changed to a 30G tip. The shell nozzle was kept the same using a 16G as previously described. As indicated by the measured flow rates, the applied pressures were changed and pressures of 0.1, 0.5 and 0.75 bar were applied on the shell and 1.5, 2.0, 2.5 and 3.0 bar on the core.

Reducing the core diameter lowered the amount of core material within the shell, as well as still being visible under the microscope. Nevertheless, the processed fibers are alternating between *Janus*- and coaxial fibers depending on the printing direction probably due to an missalignement of the core nozzle within the shell. Due to the smaller diameter 30G nozzle, the tip is more prone to be bent, especially when manually ground to the required length.

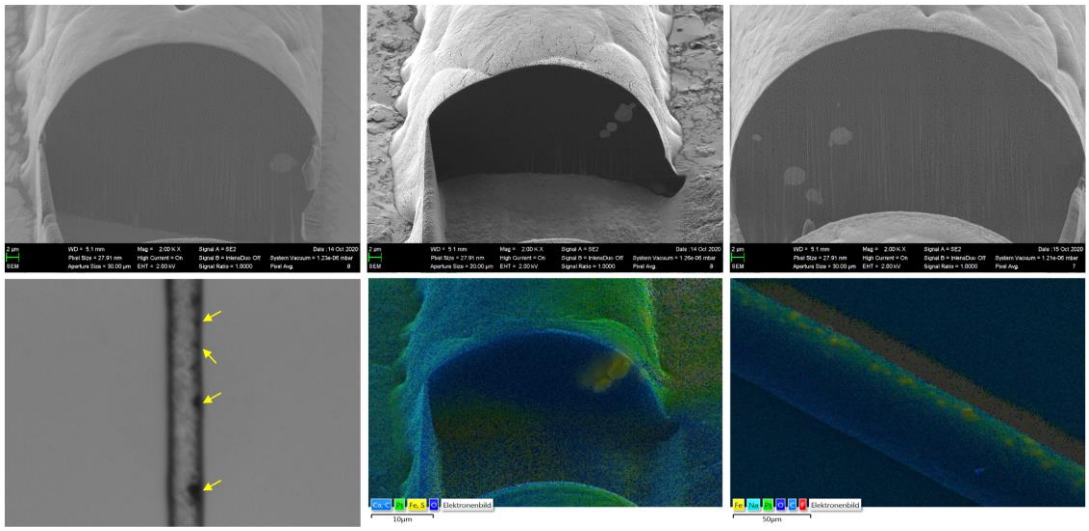

Figure 4. Showing examples of *Janus* fibers using neat PCL and PCL containing CI particles. A-C) SEM images of *Janus* fibers cutted using FIB. D) showing a stereomicroscope images of a *Janus* fiber consisting of PCL (white-grey) and CI particles (black, indicated using arrows). E-F) showing SEM images with EDX to visualize the embedded CI particles located on one side of the *Janus* fibers.

The resulting core and total fiber diameter are shown in Figure 5. In general, with increasing applied pressure, the total fiber diameter increased. In contrast, even when increasing the applied core pressure, the resulting core diameter stayed quite constant at around 10 µm for most of the applied pressures even when varying the collector speed.

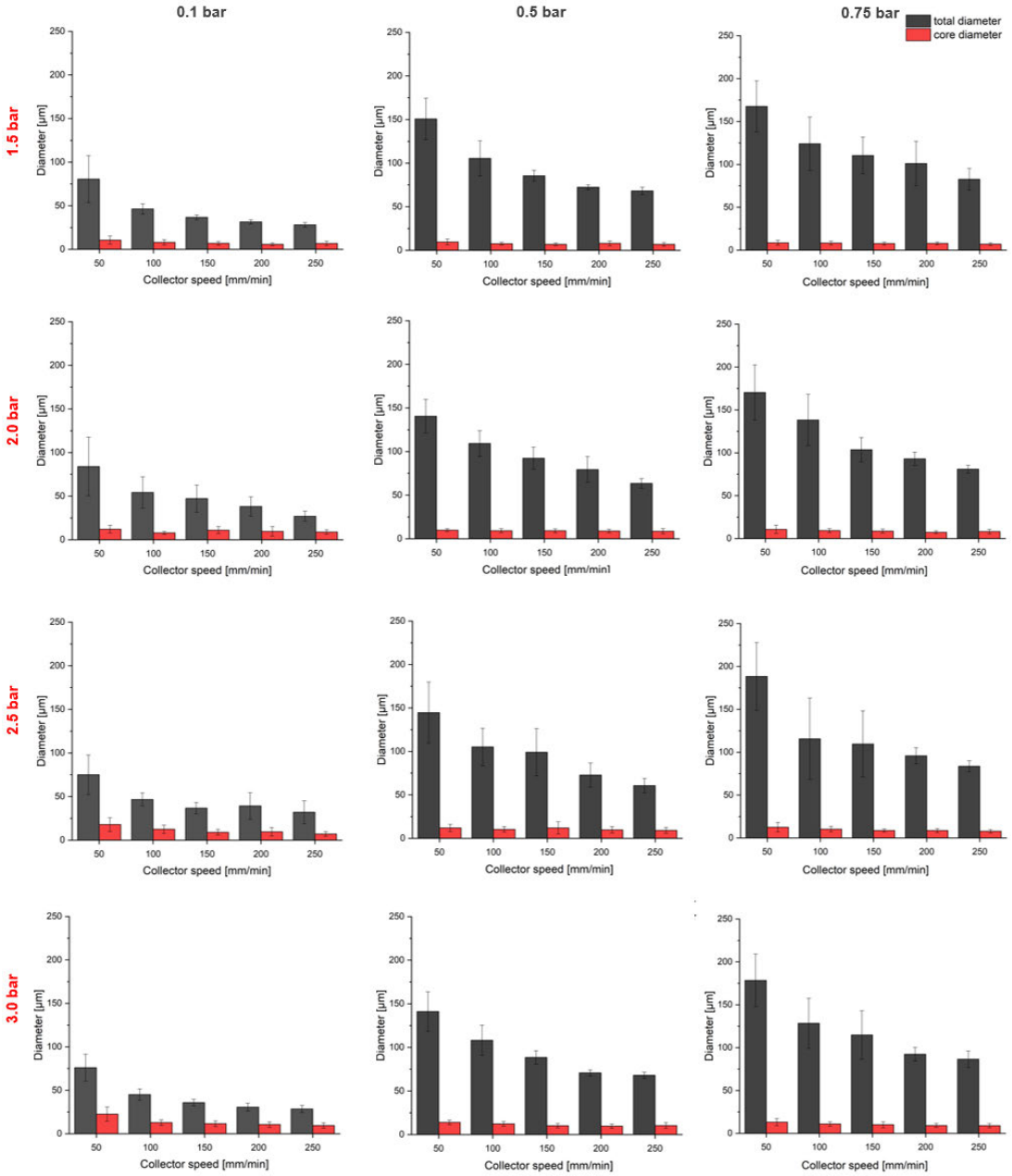

Figure 5. Fiber diameter ratios of coaxial fibers using a 16G nozzle tip as the shell and a 30G nozzle tip as the core. Applied shell pressures were varied from 0.1, 0.5 and 0.75 bar and core pressures between 1.5, 2.0, 2.5 and 3.0 bar. The resulting total fiber diameter is indicated in dark grey and the core diameter in red for printing speeds between 50 to 250 mm/min increased in increments of 50 mm/min.

In general, an increasing printing speed will lead to a decrease in fiber diameter when processing polymers using MEW.[5] This trend is also visible for the coaxial fibers and their resulting total fiber diameter.[1] Using the 30G core nozzle, depending on the applied pressure and the printing speed, the total coaxial fiber diameter is ranging from around 30 µm to 190 µm (Figure 5). The quite large fiber diameters of up to 180 µm might be due to the big 16G shell nozzle. Most

commonly, nozzle ranging from 20 to 30G are used for MEW-processing resulting in fiber diameters in the lower micron range between 5 to 50 µm.[3, 4]

In Figure 6, SEM images of coaxial fibers are shown. Focused ion beam (FIB) was used to cut into the fiber to check the position of the PCL containing CI particles. The CI particles are visible as white dots indicated using a yellow arrow. Supporting video S1 is showing a GIF animation of a series of SEM images with cuts throughout the coaxial fiber. SEM images were taken by Philipp Stahlhut.

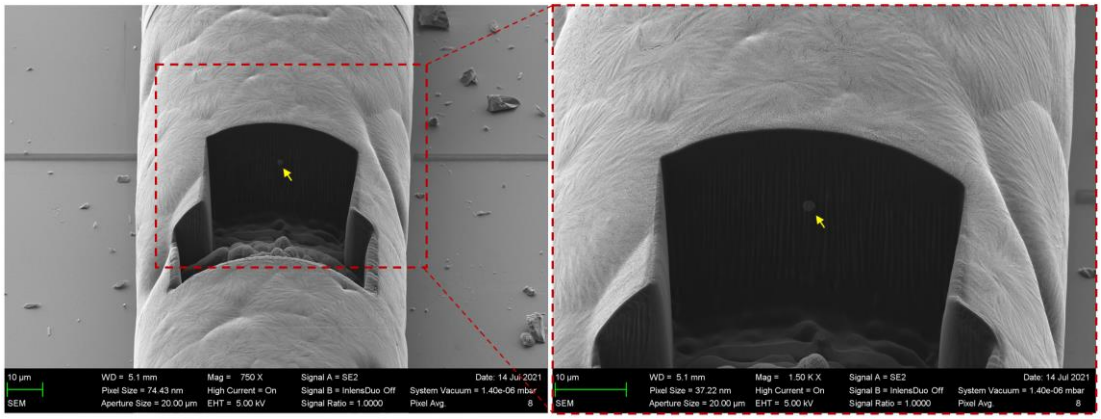

Figure 6. Coaxial fibers using a 16G nozzle tip as the shell and a 30G nozzle tip as the core. CI particles embedded within the PCL matrix is indicated with a yellow arrow.

To get an impression how different nozzle setups are influencing the flow rates, the flow rates of the resulting shell material has been investigated. Therefore, the 16G nozzle tip as the shell and the 22G and 30G nozzle tip for the core were used. The pressure of the core material was turned off and by printing a spiral design at different shell pressures, the resulting flow rates were studied. The results are listed in Table 2.

Table 2. Shell flow rates measured for the 22G and 30 G core nozzle at varying shell pressures.

22G shell pressure [bar]	**1.5**	**2.0**	**2.5**	**3.0**
flow rate (shell) [mg / 30 min]	16.35 ± 0.68	16.29 ± 0.07	25.17 ± 0.19	29.66 ± 1.38
30G shell pressure [bar]	**2.0**	**0.1**	**0.5**	**0.75**
flow rate (shell) [mg / 30 min]	106.30 ± 3.87	6.58 ± 0.62	22.99 ± 4.20	44.60 ± 1.37

As expected, when decreasing the nozzle diameter of the core, the flow rates of the shell material will increase even though the applied pressure on the shell has

been significantly reduced (values adapted from previous experiments). To be able to compare the results, within both nozzle systems an applied pressure of 2.0 bar has been investigated resulting in a flow rate of around 16 mg/30min for the 22G core nozzle and a flow rate of around 106 mg/30min for the 30G core nozzle. The flow rates are generally matching with the fiber diameter results, as the smaller core nozzle resulted in more shell material within the coaxial fiber.

5.5 Conclusion

In this study, a coaxial MEW system has been established and studied using PCL-based materials. Using neat PCL as the shell material and PCL containing 30 wt.% CI particles allowed to visualize the core material within the shell material using microscopy. However, due to the limitations of the current coaxial nozzle design, not all resulting fibers were coaxial with perfectly centered core within the shell. Nevertheless, successful fabrication of homogenous dual material fibers resulting in *Janus*- and coaxial fibers, depending on the printing direction, has been shown and further investigated using SEM imaging. To improve the alignment of the core, a 3D printed nozzle might be a promising approach by for example adding positioning guides to better align the core tip within the shell, as previously shown by Eberle *et al*. [1]. Furthermore, reducing the size of the shell nozzle might be of interest to decrease the resulting fiber diameter to more common fiber sizes produced by MEW: Additionally, testing and establishing further material combinations using a coaxial MEW system can offer promising results for applications in e.g., drug release studies or electronic devices. Nevertheless, to the best of our knowledge, it is the first-time using MEW to produce coaxial fibers including two materials within one fiber.

5.6 References

[1] F. Eberle, A.-K. Gruska, B. Filippi, P. Stahlhut, G.G. Wallace, P.D. Dalton, S. Beirne, Hollow-Fiber Melt Electrowriting Using a 3D-Printed Coaxial Nozzle, Advanced Engineering Materials n/a(n/a) 2100750.

[2] J. Kim, E. Bakirci, K.L. O'Neill, A. Hrynevich, P.D. Dalton, Fiber Bridging during Melt Electrowriting of Poly(ε-Caprolactone) and the Influence of Fiber Diameter and Wall Height, Macromolecular Materials and Engineering 306(3) (2021) 2000685.

[3] J.C. Kade, P.D. Dalton, Polymers for Melt Electrowriting, Advanced Healthcare Materials 10(1) (2021) 2001232.

[4] T.M. Robinson, D.W. Hutmacher, P.D. Dalton, The Next Frontier in Melt Electrospinning: Taming the Jet, Advanced Functional Materials 0(0) (2019) 1904664.

[5] A. Hrynevich, B.Ş. Elçi, J.N. Haigh, R. McMaster, A. Youssef, C. Blum, T. Blunk, G. Hochleitner, J. Groll, P.D. Dalton, Dimension-Based Design of Melt Electrowritten Scaffolds, Small 14(22) (2018) 1800232.

Chapter 6

– Concluding Discussion and Further Perspectives

Concluding Discussion and Further Perspectives

Additive manufacturing (AM) is of increasing interest due to its freedom in design allowing to fabricate structures, that haven´t been possible before. This compltements formative or additive manufacturing technologies that have been previously developed. However, most of the afore-mentioned techniques, especially in the field of regenerative medicine and tissue engineering, use either toxic solvents such as SES or have limited resolution.

Within this study, MEW, a high-resolution AM technique has been further investigated to expand the list of processable materials with special focus on electroactive PVDF based materials. The technique is quite young and has been demonstrated for the first time in 2011.[2] Therefore, only a limited number of materials have been shown to be processable and the most common material used is PCL, the current gold standard.[3] Using PCL for MEW allows to process well-defined and complex structures either on flat collectors made of different materials to further investigate the influence of those materials on the charge transfer[4]; on non-flat collectors[5-7] to better mimic the native structures, or on tubular collectors allowing to fabricate stent-like and blood-vessel like structures.[8-12]

PVDF, a piezoelectric material, has been previously demonstrated MEW-processability by Florczak *et al*. [1]. However, while direct-writing this polymer, the printed fibers and samples often started to warp and detach from the collector limiting the stackability of the polymer when processing onto a collector at room temperature. The fabricated samples start to detach at the edges interfering with the printing process and either causing jet break-ups or damage of the processed scaffold.[13] Known from fused deposition modelling (FDM) printing, warping can be minimized when using a heated print bed.[14] Therefore, in Chapter 2 we investigated the influence of a heated collector between 50-150 °C. At collector temperatures of 110 °C scaffolds with 10 alternating layers in x- and y-direction were fabricated at printing speeds of 2000 mm/min. Additionally, the heat from the collector improved the layer fusion resulting in more stable and easier to handle scaffolds. At collector temperatures of 120 °C and higher, fibers coalesced into spheres at the intersections of the scaffolds.[13] This might be caused due to too high temperatures between the print head and the collector.

The use of a heated collector introduces a new parameter when MEW-processing materials helping to control fiber fusion, as well as the solidification of the melt, especially when direct-writing high melting temperature polymers.[13] Therefore, further investigations regarding the heat transfer between the print head and the collector would be of interest and could additionally performed using model

simulations. *In situ* model simulations are of growing interest and have successfully been used to support experimental studies specially to visualize the electric field and its influences on the MEW process.[6, 7, 15, 16]

As previously mentioned, MEW is a quite young fabrication methods still lacking a wide range of processable materials. Therefore, different studies successfully incorporated particles into polymer matrices to further expand the list of potential polymers, as well as to enable special properties like improved cell growth[17] and bioactivity[18] to either new or already established materials as summarized in the introduction.[3]

In Chapter 3, the list of MEW-processable polymers was expanded by compounding carbonyl iron (CI) particles into a PVDF matrix with up to 30 wt.%. CI particles are a black powder known for its magnetic properties, as well as high thermal stability and biocompatibility.[19, 20] Printing of four different composites containing 1, 5, 15 and 30 wt.% CI particles within the PVDF matrix were investigated and compared to neat PVDF. All blends were processable via MEW without nozzle clogging resulting in uniform fibers. Processing 30 wt.% CI particles in the PVDF did result in less uniform fibers and rougher surface. Additionally, the fiber color changed from white-light grey with a smooth fiber morphology for neat PVDF to dark grey-black fibers showing rougher fiber morphology with increasing CI particle content. The resulting fiber diameters did vary between 30 to 50 µm depending on the particle content and the printing speed. Homogenous distribution of the particles within the PVDF matrix was proven by SEM and EDX images. Furthermore, all blends showed sufficient cytocompatibility investigated using L929 cells offering the possibility for the use in magnetoactive cell simulation. To the best of my knowledge, 30 wt.% particles within a polymer matrix is the highest number of compounded particles processed via MEW without the addition of further additives or solvents to lower the viscosity while printing.

In Chapter 4, another electroactive polymer, the PVDF copolymer P(VDF-*co*-TrFE), was tested and established via MEW.[21] Processing the copolymer was only possible when using a heated collector at 120 °C and remarkable low printing speeds between 10 to 100 mm/min. The highly viscous material showed a very fast solidification while printing resulting in non-adherence to the collector when direct written onto a substrate temperature below 120 °C. Similar results, where a heated collector was needed to enable MEW-processing, was previously shown when processing polypropylene (PP).[22] Processing PP was mainly conducted at printing speeds below 200 mm/min and a collector temperature of at least 70 °C was needed to enable sufficient jet adherence.[22]

Furthermore, when cooling down the fabricated P(VDF-*co*-TrFE) scaffolds, the straight lines formed sinusoidal structures and no critical translation speed (CTS) was detected for this material with fiber morphologies changing to fibrillar structures from crystallites depending on the printing speed. The different morphologies could be caused by the stretching of the jet, which is highly depending on the printing speed and can influence the solidification of the processed melt.

Additionally, PVDF-based polymers are known for their different crystallite polymorphs with the β-phase being the most interesting one related to the electroactive properties. An increase in β-phase can be achieved by stretching, pooling and/or annealing of those materials.[21, 23-27] Therefore, XRD measurements were done on the scaffolds processed at different collector temperatures and an increase of the piezoelectric β-phase was detected after MEW-processing when compared to unprocessed powder. Furthermore, the electroactive nature was proven by PFM measurements.[21]

Being able to direct-write P(VDF-*co*-TrFE) via MEW without the need of any toxic solvent into well-defined structures with resulting fiber diameters in the lower micron-range offers promising potential in biomedical applications, as well as actuators and sensors.[21]

Within this thesis, MEW of PVDF, PVDF containing CI particles and P(VDF-*co*-TrFE) has been successfully demonstrated and thereby two new materials have been added to the list of processable materials using MEW. Additionally, investigating the direct-writing of new materials can lead to interesting findings and phenomena, which have not been observed before like the absence of the CTS when processing P(VDF-*co*-TrFE) and/or very low printing speeds. Furthermore, testing new polymers can require additional printing parameters like a heated collector to enable the fabrication of fibers and scaffolds especially when using highly viscous and/or high melting point materials.

Future steps should focus on in depth characterization of the PVDF-based fibers and scaffolds regarding their piezoelectric behavior and the influence of the MEW-processing. The magnetic behavior of the scaffolds fabricated using PVDF containing CI particles should also be studied more in depth, for example via vibrating sample magnetometry. Due to the proven cytocompatibility of the PVDF containing CI particles, this blend offers promising potential for the use as magnetoactive material for muscle and/or bone regeneration as previously shown by Fernandes *et al*.[28] using PVDF and cobalt ferrite nanoparticles.

Furthermore, due to the piezoelectric properties of the PVDF-based materials, MEW-processing those polymers into well-defined scaffolds without the need of

toxic solvents, is offering promising potential to stimulate cells under electrical and/or mechanical stimulation. This research area could benefit from the freedom in design of such scaffolds enabled by MEW and therefore, these polymer scaffolds might support cell differentiation under mechanical load especially of interest for bone tissue engineering.[28-30]

Thinking about fiber and scaffold designs for biomedical applications, an increasing field of interest is dealing with the incorporation of drugs or bioactive molecules.[31-35] Coaxial fibers are therefore offering promising potential enabling to fabricate dual material combinations. So far, a coaxial MEW setup has only been described to process hollow fibers using PCL[36], however, not yet to process dual material fibers.

Therefore, in Chapter 5, the aim of the study was to establish a coaxial MEW setup enabling the fabrication of dual material coaxial fibers with diameters in the lower micron-range typically for MEW. The coaxial MEW print head and nozzle was designed and assembled by Andrei Hrynevich and Harald Hümpfer. With this setup, an existing MEW printer has been adapted and modified to study the fabrication of dual material fibers. In this study, PCL-based polymers were used to investigate the influence of the applied pressures, as well as the printing speed onto the resulting fibers. Neat PCL was used as the shell and as core material, PCL containing CI particles has been used, as the black material in the core allowed faster visualization of the printed fibers under a light microscope. The results showed dual material fibers, however, depending on the printing direction, the resulting fibers were either *Janus*- or coaxial fibers. With the first causing two materials processed next to each other instead of one material surrounding the other material (coaxial fibers).

Depending on the core diameter, as well as the applied pressures to both materials, it was possible to control the polymer ratios within the fibers. Furthermore, the typical trend of increasing speed leading to smaller diameter fibers was detected. Interestingly, the shell material seemed to be mainly influenced be the printing speeds. SEM images and FIB helped to visualize the outer fiber morphology, as well as to cut into the fibers to see the placement of the core material within the shell. As both materials are based on PCL, using EDX only helped to indicate the carbonyl iron particles within the core and an intersection area between the core and shell was not possible to see.

Future investigations regarding other material combinations would be of interest and could allow to better visualize the transition between the core and shell polymer under the SEM. Furthermore, adjustments to the nozzle design are needed to better

align the inner nozzle within the outer nozzle. An interesting approach has been shown by Eberle *et al*.[36] using a 3D metal printer to fabricate the coaxial nozzle including positioning guides for better centering of the core nozzle. Additionally, as previously mentioned, simulation techniques are more often used to further understand and improve 3D printing processes, as well as the resulting designs. Therefore, future approaches regarding the improved nozzle design should incorporate flow simulations within the nozzle design. This could help to improve the designs without wasting a lot of resources and should definetly be considered within the next steps.

As MEW is a high-resolution 3D printing technique with growing interest especially in the field of regenerative medicine and tissue engineering, within this work, it was possible to extend the list of processable materials. The established PVDF-based materials offer promising potential for the application in tissue engineering, biomedical and electronic devices.[23, 37, 38]

Additionally, when establishing new materials, as well new printer designs, often the general printer setup must be adjusted depending on the requirements and needs. This has also been shown in literature for example by implementing an adjustable voltage and Z-distance while printing to increase the resulting sample height[8, 39], to be able to print onto non-flat surfaces[5-7] and/or to monitor and analyze the printing process *in situ* to faster understand and adapt printer parameters.[8, 40]

References

[1] S. Florczak, T. Lorson, T. Zheng, M. Mrlik, D.W. Hutmacher, M.J. Higgins, R. Luxenhofer, P.D. Dalton, Melt electrowriting of electroactive poly(vinylidene difluoride) fibers, Polymer International 68(4) (2019) 735-745.

[2] T.D. Brown, P.D. Dalton, D.W. Hutmacher, Direct Writing By Way of Melt Electrospinning, Advanced Materials 23(47) (2011) 5651-5657.

[3] J.C. Kade, P.D. Dalton, Polymers for Melt Electrowriting, Advanced Healthcare Materials 10(1) (2021) 2001232.

[4] H. Ding, K. Cao, F. Zhang, R. C. Chang, A fundamental study of charge effects on the melt electrowritten polymer fibers, Materials & Design (2019) 107857.

[5] C.D. O'Connell, O. Bridges, C. Everett, N. Antill-O'Brien, C. Onofrillo, C. Di Bella, Electrostatic Distortion of Melt-Electrowritten Patterns by 3D Objects: Quantification, Modeling, and Toolpath Correction, Advanced Materials Technologies n/a(n/a) 2100345.

[6] Q.C. Peiffer, M. de Ruijter, J. van Duijn, D. Crottet, E. Dominic, J. Malda, M. Castilho, Melt electrowriting onto anatomically relevant biodegradable substrates: Resurfacing a diarthrodial joint, Materials & Design 195 (2020) 109025.

[7] N.T. Saidy, T. Shabab, O. Bas, D.M. Rojas-González, M. Menne, T. Henry, D.W. Hutmacher, P. Mela, E.M. De-Juan-Pardo, Melt Electrowriting of Complex 3D Anatomically Relevant Scaffolds, Frontiers in Bioengineering and Biotechnology 8(793) (2020).

[8] P. Mieszczanek, T.M. Robinson, P.D. Dalton, D.W. Hutmacher, Convergence of Machine Vision and Melt Electrowriting, Advanced Materials 33(29) (2021) 2100519.

[9] I. Pennings, E.E. van Haaften, T. Jungst, J.A. Bulsink, A.J.W.P. Rosenberg, J. Groll, C.V.C. Bouten, N.A. Kurniawan, A.I.P.M. Smits, D. Gawlitta, Layer-specific cell differentiation in bi-layered vascular grafts under flow perfusion, Biofabrication 12(1) (2019) 015009.

[10] E. McColl, J. Groll, T. Jungst, P.D. Dalton, Design and fabrication of melt electrowritten tubes using intuitive software, Materials & Design 155 (2018) 46-58.

[11] K. Somszor, O. Bas, F. Karimi, T. Shabab, N.T. Saidy, A.J. O'Connor, A.V. Ellis, D. Hutmacher, D.E. Heath, Personalized, Mechanically Strong, and Biodegradable Coronary Artery Stents via Melt Electrowriting, ACS Macro Letters 9(12) (2020) 1732-1739.

[12] N.C. Paxton, R. Daley, D.P. Forrestal, M.C. Allenby, M.A. Woodruff, Auxetic tubular scaffolds via melt electrowriting, Materials & Design (2020) 108787.

[13] J.C. Kade, P.F. Otto, R. Luxenhofer, P.D. Dalton, Melt electrowriting of poly(vinylidene difluoride) using a heated collector, Polymers for Advanced Technologies n/a(n/a).

[14] M. Alsoufi, A. El-Sayed, Warping Deformation of Desktop 3D Printed Parts Manufactured by Open Source Fused Deposition Modeling (FDM) System, International Journal of Mechanical & Mechatronics Engineering 17 (2017) 7-16.

[15] F.M. Wunner, S. Eggert, J. Maartens, O. Bas, P.D. Dalton, E.M. De-Juan-Pardo, D.W. Hutmacher, Design and Development of a Three-Dimensional Printing High-Throughput Melt Electrowriting Technology Platform, 3D Printing and Additive Manufacturing 6(2) (2018) 82-90.

[16] U. Saha, R. Nairn, O. Keenan, M.G. Monaghan, A Deeper Insight into the Influence of the Electric Field Strength When Melt-Electrowriting on Non-Planar Surfaces, Macromolecular Materials and Engineering n/a(n/a) 2100496.

[17] A. Abdal-hay, N. Abbasi, M. Gwiazda, S. Hamlet, S. Ivanovski, Novel polycaprolactone/hydroxyapatite nanocomposite fibrous scaffolds by direct melt-electrospinning writing, European Polymer Journal 105 (2018) 257-264.

[18] E. Hewitt, S. Mros, M. McConnell, J. Cabral, A. Ali, Melt-electrowriting with novel milk protein/PCL biomaterials for skin regeneration, Biomedical Materials (2019).

[19] M. Cvek, M. Mrlík, M. Ilčíková, J. Mosnáček, V. Babayan, Z. Kuceková, P. Humpolíček, V. Pavlínek, The chemical stability and cytotoxicity of carbonyl iron particles grafted with poly(glycidyl methacrylate) and the magnetorheological activity of their suspensions, RSC Advances 5(89) (2015) 72816-72824.

[20] M. Mrlík, M. Ilčíková, M. Cvek, V. Pavlínek, A. Zahoranová, Z. Kroneková, P. Kasak, Carbonyl iron coated with a sulfobetaine moiety as a biocompatible system and the magnetorheological performance of its silicone oil suspensions, RSC Advances 6(39) (2016) 32823-32830.

[21] J.C. Kade, B. Tandon, J. Weichhold, D. Pisignano, L. Persano, R. Luxenhofer, P.D. Dalton, Melt electrowriting of poly(vinylidene fluoride-co-trifluoroethylene), Polymer International n/a(n/a).

[22] J.N. Haigh, T.R. Dargaville, P.D. Dalton, Additive manufacturing with polypropylene microfibers, Materials Science and Engineering: C 77 (2017) 883-887.

[23] A.H. Rajabi, M. Jaffe, T.L. Arinzeh, Piezoelectric materials for tissue regeneration: A review, Acta Biomaterialia 24 (2015) 12-23.

[24] C. Ribeiro, C.M. Costa, D.M. Correia, J. Nunes-Pereira, J. Oliveira, P. Martins, R. Gonçalves, V.F. Cardoso, S. Lanceros-Méndez, Electroactive poly(vinylidene

fluoride)-based strctures for advanced applications, Nature Protocols 13(4) (2018) 681-704.

[25] P. Martins, A.C. Lopes, S. Lanceros-Mendez, Electroactive phases of poly(vinylidene fluoride): Determination, processing and applications, Progress in Polymer Science 39(4) (2014) 683-706.

[26] R.I. Haque, R. Vié, M. Germainy, L. Valbin, P. Benaben, X. Boddaert, Inkjet printing of high molecular weight PVDF-TrFE for flexible electronics, Flexible and Printed Electronics 1(1) (2015) 015001.

[27] J. Hafner, M. Teuschel, M. Schneider, U. Schmid, Origin of the strong temperature effect on the piezoelectric response of the ferroelectric (co-)polymer P(VDF70-TrFE30), Polymer 170 (2019) 1-6.

[28] M.M. Fernandes, D.M. Correia, C. Ribeiro, N. Castro, V. Correia, S. Lanceros-Mendez, Bioinspired Three-Dimensional Magnetoactive Scaffolds for Bone Tissue Engineering, ACS Applied Materials & Interfaces 11(48) (2019) 45265-45275.

[29] M.F. Abazari, F. Soleimanifar, S.E. Enderami, M. Nematzadeh, N. Nasiri, F. Nejati, E. Saburi, S. Khodashenas, B. Darbasizadeh, M.M. Khani, P. Ghoraeian, Incorporated-bFGF polycaprolactone/polyvinylidene fluoride nanocomposite scaffold promotes human induced pluripotent stem cells osteogenic differentiation, Journal of Cellular Biochemistry 120(10) (2019) 16750-16759.

[30] A. Mirzaei, A.S. Moghadam, M.F. Abazari, F. Nejati, S. Torabinejad, M. Kaabi, S.E. Enderami, A. Ardeshirylajimi, M. Darvish, F. Soleimanifar, E. Saburi, Comparison of osteogenic differentiation potential of induced pluripotent stem cells on 2D and 3D polyvinylidene fluoride scaffolds, Journal of Cellular Physiology 234(10) (2019) 17854-17862.

[31] L. Hahn, M. Beudert, M. Gutmann, L. Keßler, P. Stahlhut, L. Fischer, E. Karakaya, T. Lorson, I. Thievessen, R. Detsch, T. Lühmann, R. Luxenhofer, From Thermogelling Hydrogels toward Functional Bioinks: Controlled Modification and Cytocompatible Crosslinking, Macromolecular Bioscience 21(10) (2021) 2100122.

[32] J. Plch, K. Venclikova, O. Janouskova, J. Hrabeta, T. Eckschlager, K. Kopeckova, Z. Hampejsova, Z. Bosakova, J. Sirc, R. Hobzova, Paclitaxel-Loaded Polylactide/Polyethylene Glycol Fibers with Long-Term Antitumor Activity as a Potential Drug Carrier for Local Chemotherapy, Macromolecular Bioscience 18(6) (2018) 1800011.

[33] N.N. Maşlakcı, Development and Characterization of Drug-Loaded PVP/PAN/Gr Electrospun Fibers for Drug Delivery Systems, ChemistrySelect 6(10) (2021) 2548-2560.

[34] K. Wulf, D. Arbeiter, C. Matschegewski, M. Teske, J. Huling, K.-P. Schmitz, N. Grabow, S. Kohse, Smart releasing electrospun nanofibers—poly: L.lactide fibers as dual drug delivery system for biomedical application, Biomedical Materials 16(1) (2020) 015022.
[35] M.B. Taskin, T. Ahmad, L. Wistlich, L. Meinel, M. Schmitz, A. Rossi, J. Groll, Bioactive Electrospun Fibers: Fabrication Strategies and a Critical Review of Surface-Sensitive Characterization and Quantification, Chemical Reviews 121(18) (2021) 11194-11237.
[36] F. Eberle, A.-K. Gruska, B. Filippi, P. Stahlhut, G.G. Wallace, P.D. Dalton, S. Beirne, Hollow-Fiber Melt Electrowriting Using a 3D-Printed Coaxial Nozzle, Advanced Engineering Materials n/a(n/a) 2100750.
[37] Y. Bar-Cohen, Electroactive Polymers as Artificial Muscles: A Review, Journal of Spacecraft and Rockets 39(6) (2002) 822-827.
[38] R.A. Surmenev, R.V. Chernozem, I.O. Pariy, M.A. Surmeneva, A review on piezo- and pyroelectric responses of flexible nano- and micropatterned polymer surfaces for biomedical sensing and energy harvesting applications, Nano Energy 79 (2021) 105442.
[39] F.M. Wunner, M.-L. Wille, T.G. Noonan, O. Bas, P.D. Dalton, E.M. De-Juan-Pardo, D.W. Hutmacher, Melt Electrospinning Writing of Highly Ordered Large Volume Scaffold Architectures, Advanced Materials 30(20) (2018) 1706570.
[40] F.M. Wunner, P. Mieszczanek, O. Bas, S. Eggert, J. Maartens, P.D. Dalton, E.M. De-Juan-Pardo, D.W. Hutmacher, Printomics: the high-throughput analysis of printing parameters applied to melt electrowriting, Biofabrication 11(2) (2019) 025004.

Appendix

A1. Supporting Information

Chapter 2 – Melt electrowriting of poly(vinylidene difluoride) using a heated collector

Melt electrowriting (MEW) Printer

MEW of poly(vinylidene difluoride) (PVDF) has been performed on a custom-built MEW device as previously described [1-3] equipped with a handmade temperature controlled collector.[1] The melting of the polymer powder within the glass syringe was guaranteed using a proportional-integral-derivative-regulated (TR400, Delta-t, Bielefeld, Germany) electrical heating system. To extrude the polymer melt through the metal nozzle tip, nitrogen gas is supplied and controlled with a pneumatic melt feeding system (regulator, FESTO, Berkheim, Germany). The nozzle tip is connected to a high voltage source (DX250R, EMCO, Hallein, Austria) operated by a voltage divided measurement (Digit Multimeter 2100, Keithley, Cleveland, USA) allowing the formation of a Taylor cone at the tip.

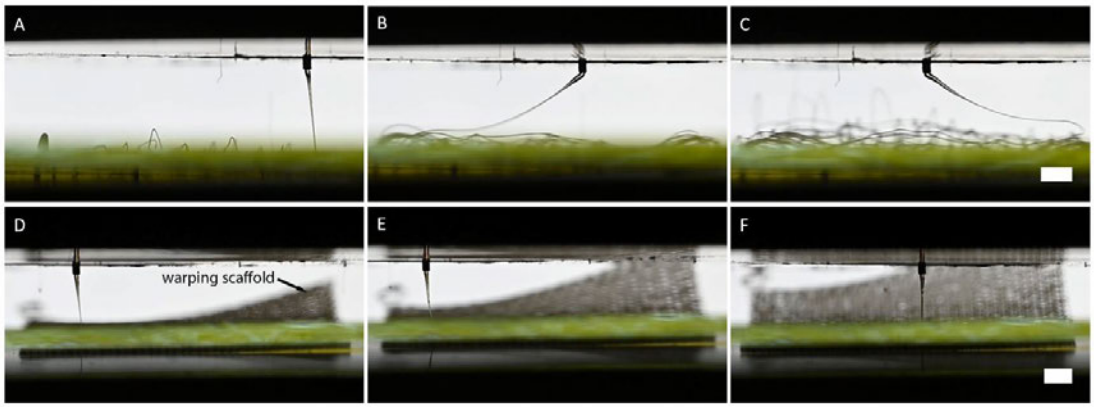

Figure S1. A-C) screenshots illustrating the lifting of fibers and the attraction to the print head while printing at RT and D-F) showing the warping process starting at the corners of the printed construct while using a heated collector at 100 °C. Scale bars = 2 mm.

The moveable collector in x- and y-direction is triggered by G-code (MACH 3 CNC software, ARTSOFT, Livermore Falls, USA) allowing precise fiber placement onto the custom-made collector consisting of an aluminum collector plate (top), an electrical Hotform® silicone heating mat (Hotset Heizpatronen und Zubehör, Lüdenscheid, Germany) in the middle and a non-conducting polyether ether ketone (PEEK) base plate.[1] The temperature of the silicone heating mat was controlled by a Hotset® PID system (Hotset Heizpatronen und Zubehör, Lüdenscheid, Germany).[1] Furthermore, when using the heated collector, the syringe and the

collector have been heated prior to adjusting the z-height between the collector and the print head manually.

X-ray diffraction (XRD) measurements

To investigate the influence of the MEW process onto the crystal phase contents of the PVDF fibers, XRD spectra were collected using a BRUKER D8 ADVANCE. The operating voltage and current used were 30 kV and 53.3 mA. Cu Kα radiation was used with a step size of 0.045°, a dwell time of 0.7 s and a rotation of 15 rpm in the 2θ range of 10° to 50° with a zero-background sample holder made of a silicon single crystal. The unprocessed PVDF powder and MEW-processed scaffolds printed at different collector temperatures were measured with n=2 scaffolds per condition. Background corrections on the measurements were done using a beam knife and the software DIFFRAC.EVA.

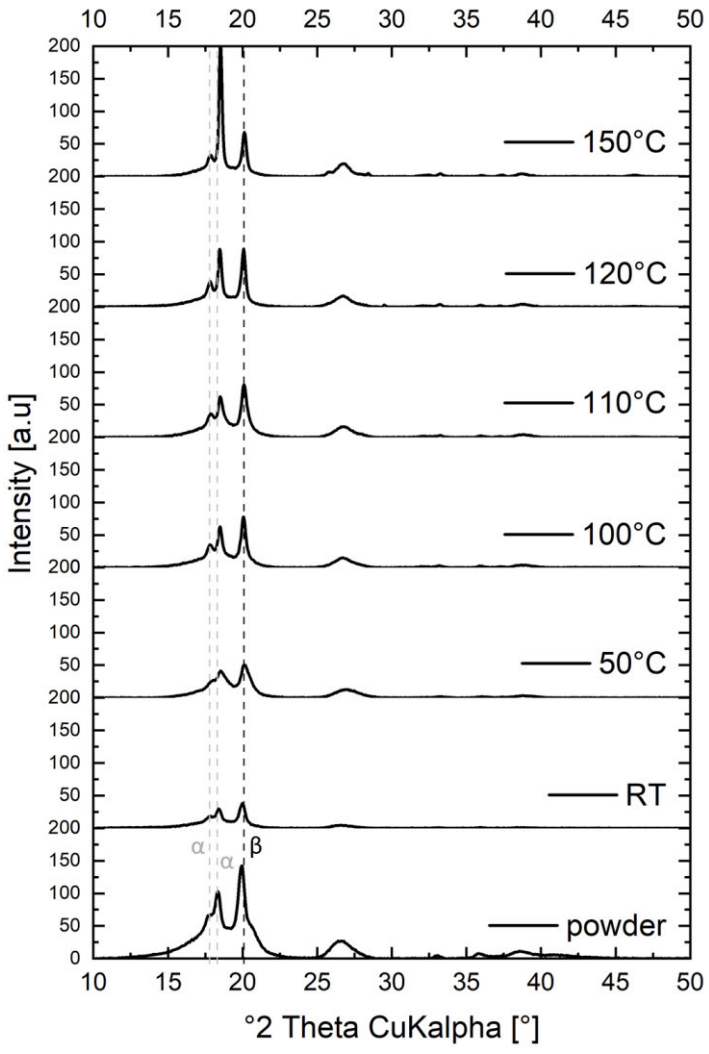

Figure S2. Showing the XRD measurements of the MEW-processed scaffolds at different collector temperatures ranging from room temperature (RT) to 150 °C, as well as the unprocessed PVDF powder as a reference. Dotted lines indicate the peaks for the α- (grey) and β-phase (black).

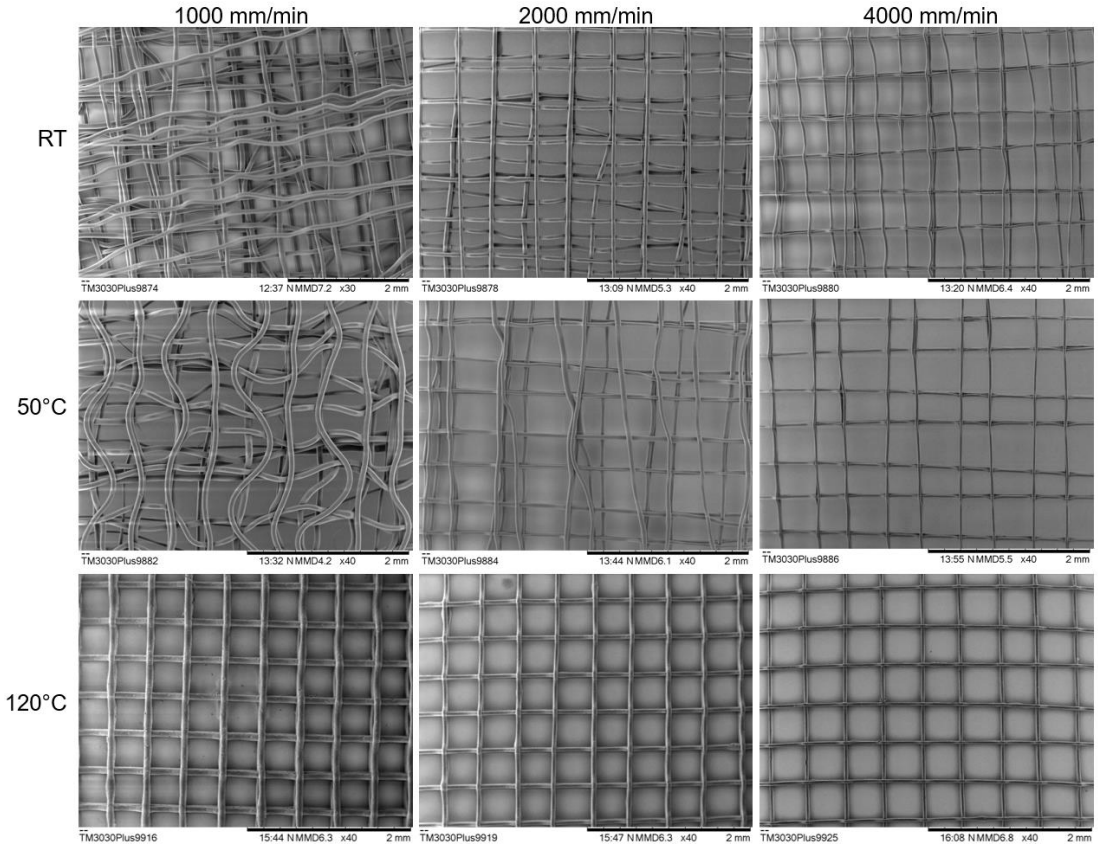

Figure S3. SEM images showing scaffolds (3 layers in each direction) printed at RT without the use of a heated collector and at collector temperatures of 50 °C and 120 °C with different printing speeds of 1000, 2000 and 4000 mm/min.

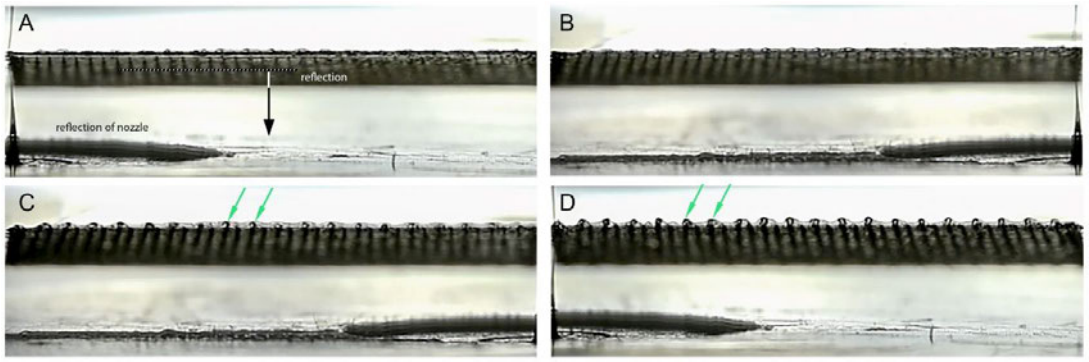

Figure S4. Series of screenshots showing the formation of the coalesced spheres with increased layers. A-D) indicating the coalescence of the newly printed layer to the spheres (green arrows).

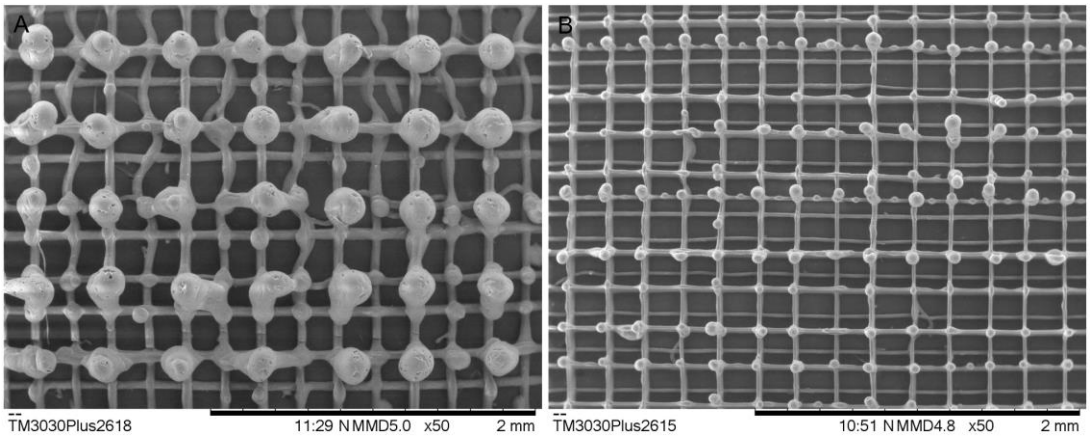

Figure S5. Tabletop SEM images showing sphere formation within scaffolds printed with a 250 µm fiber spacing using a A) 26-gauge (10 layers) and B) 30-gauge nozzle tip (15 layers).

Table S1. Contact angle measurements of PVDF scaffolds printed at a collector temperature of 140-150 °C and different numbers of layers in x- and y-direction, as well as different nozzle gauge. For scaffolds printed with a 30G nozzle, the distance between the collector and print head was set to around 2.5 mm.

	contact angle [°]				
	3 layers	5 layers	7 layers	10 layers	15 layers
26 G 500 µm	115 ± 15,68	127 ± 3,79	132 ± 5,15	125 ± 3,51	-
26 G 250 µm	129 ± 8,49	119 ± 4,54	120 ± 10,14	126 ± 5,47	-
30 G 250 µm	127 ± 6,64	130 ± 4,16	134 ± 5,09	129 ± 6,23	124 ± 5,47

Supporting Video S1. Showing the difference in scaffold stability during handling depending on the usage of a heated collector. Left scaffold is fabricated without the use of a heated collector and the right scaffold was fabricated at a collector temperature of 110 °C.

Supporting Video S2. Showing the printing process of a scaffold in real speed at 4000 mm/min. Some repeating sections throughout the video have been slowed down to 10% of the printing speed to better visualize the sphere formation process.

References

[1] J.N. Haigh, T.R. Dargaville, P.D. Dalton, Additive manufacturing with polypropylene microfibers, Materials Science and Engineering: C 77 (2017) 883-887.

[2] G. Hochleitner, J.F. Hümmer, R. Luxenhofer, J. Groll, High definition fibrous poly(2-ethyl-2-oxazoline) scaffolds through melt electrospinning writing, Polymer 55(20) (2014) 5017-5023.

[3] G. Hochleitner, T. Jüngst, T.D. Brown, K. Hahn, C. Moseke, F. Jakob, P.D. Dalton, J. Groll, Additive manufacturing of scaffolds with sub-micron filaments via melt electrospinning writing, Biofabrication 7(3) (2015) 035002.

Chapter 3 – Effect of carbonyl iron particles on the melt electrowriting process

Thermogravimetric Analysis (TGA)

TGA was performed on a TG 209F1 Iris (NETZSCH, Selb, Germany). The samples (5 – 10 mg) were added to aluminum oxide crucibles (NETZSCH, Selb, Germany) and heated under synthetic air from 30 °C to 900 °C with a heating rate of 10 °C/min. The mass loss for all samples started at around 350 °C, which allows a processability of the blends at least up to 250 °C. The CI particles remained stable even at 900 °C as shown in Figure S1.

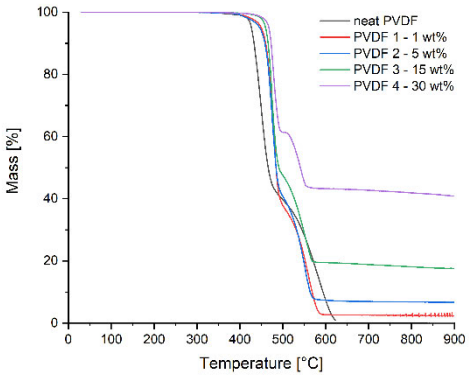

Figure S1. TGA results of the neat PVDF and the different blends containing 1, 5, 15 and 30 wt.% CI particles.

Differential Scanning Calorimetry (DSC) and X-Ray Diffraction (XRD)

The crystalline phase development, in terms of the α-phase and β-phase, was investigated in the prepared sheets using the X-Ray diffractometer (XRD) MiniFlex600 (Rigaku, Tokyo, Japan) with Co-K_α radiation source (operating at 40 kV and 20 mA) and a scan range 2θ between 5° and 45°. Due to the employment of the Co-K_α source with different working characteristics (λ = 1.789 Å) from the conventional Cu-K_α source (λ = 1.541 Å), the angle 2θ for the α-phase and β-phase was slightly shifted towards higher values.

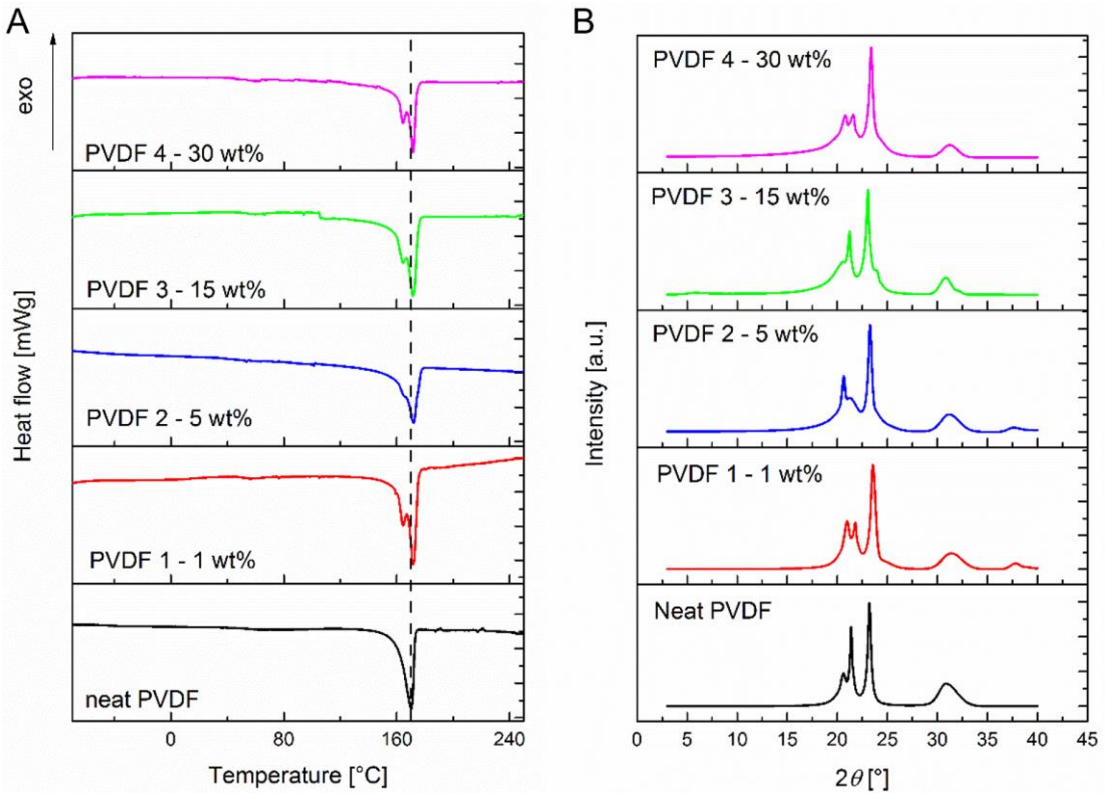

Figure S2. A) DSC scans and B) XRD pattern for individual prepared master batches of the PVDF and CI particle blends.

Infrared (IR) Spectroscopy

A Nicolet™ iS™ 10 FT IR spectrometer equipped with an DTGS KBr (Thermo Fisher Scientific) was used for the samples measured from 1500 – 550 cm^{-1}.

β-phase calculations were performed as described previously.[1, 2] The characteristic peaks for β-phase and α- phase are at wavenumbers 510, 840 and 1279 cm^{-1} and 408, 532, 614, 766, 795, 855 and 976 cm^{-1}, respectively.[2, 3] The equation (2) was used to quantify the percentage of β-phase.

$$F_\beta = \frac{A_{840}}{\left(\frac{K_{840}}{K_{766}}\right)A_{766} + A_{840}} X\ 100 \qquad (2)$$

where A_{766} and A_{840} are the absorbance values at 766 and 840 cm^{-1}, respectively. The values of K_{766} and K_{840} (absorption coefficients at respective wavenumbers) are 6.1 × 104 and 7.7 × 104 $cm^2\ mol^{-1}$, respectively.[2, 3]

The phase calculations revealed no significant change in the β-phase content after MEW-processing (**Figure S3**).

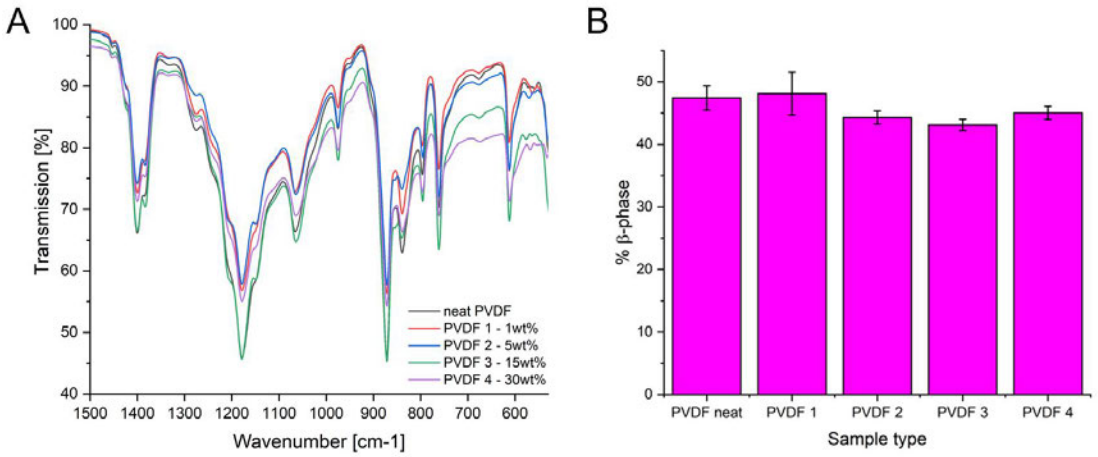

Figure S3. A) FTIR graphs of the MEW-processed scaffolds using neat PVDF, as well as blends containing 1, 5, 15 and 30 wt.% CI particles. B) the calculated β-phase contents based on the FTIR results of the MEW-processed scaffolds.

Supporting Videos

Video S1. Showing the MEW-processing of the PVDF / 30 wt.% CI below the critical translation speed (CTS).

Video S2. Demonstrating the magnetic properties of the PVDF / 30 wt.% CI scaffold.

References

[1] B. Tandon, P. Kamble, R.T. Olsson, J.J. Blaker, S.H. Cartmell, Fabrication and Characterisation of Stimuli Responsive Piezoelectric PVDF and Hydroxyapatite-Filled PVDF Fibrous Membranes, Molecules 24(10) (2019) 1903.

[2] X. Cai, T. Lei, D. Sun, L. Lin, A critical analysis of the α, β and γ phases in poly(vinylidene fluoride) using FTIR, RSC Advances 7(25) (2017) 15382-15389.

[3] P. Martins, A.C. Lopes, S. Lanceros-Mendez, Electroactive phases of poly(vinylidene fluoride): Determination, processing and applications, Progress in Polymer Science 39(4) (2014) 683-706.

Chapter 4 – Melt Electrowriting of poly(vinylidene fluoride-*co*-trifluoroethylene)

Thermogravimetric analysis (TGA)

TGA of the P(VDF-*co*-TrFE) powder was performed on a TG 209F1 Iris (NETZSCH, Selb, Germany). The samples (5 – 10 mg) were added to aluminum oxide crucibles (NETZSCH, Selb, Germany) and heated under synthetic air from 30 °C to 900 °C with a heating rate of 10 °C/min. At 170 °C (the processing temperature), the temperature was kept constant for 5 h while monitoring the mass. The provided NETZSCH Proteus – Thermal Analysis – V.5.2.1 software was used to evaluate the obtained spectra and the graph was plotted with Origin.

Differential scanning calorimetry (DSC)

DSC was performed on a DSC 204F1 Phoenix (NETZSCH, Selb, Germany) under N2-atmosphere (20 mL/min). The samples were placed in pierced aluminum crucibles (NETZSCH, Selb, Germany), heated to 200 °C (10 °C/min), kept for 10 min at 200 °C, then subsequently cooled to -50 °C (10 °C/min) and kept for 10 min at – 50 °C before heating to 200 °C for a second time (10 °C/min) (via three repeating heat/cool cycles). NETZSCH Proteus – Thermal Analysis – V.4.2.1 software was used for the heating/cooling cycle spectra and then graphed with Origin.

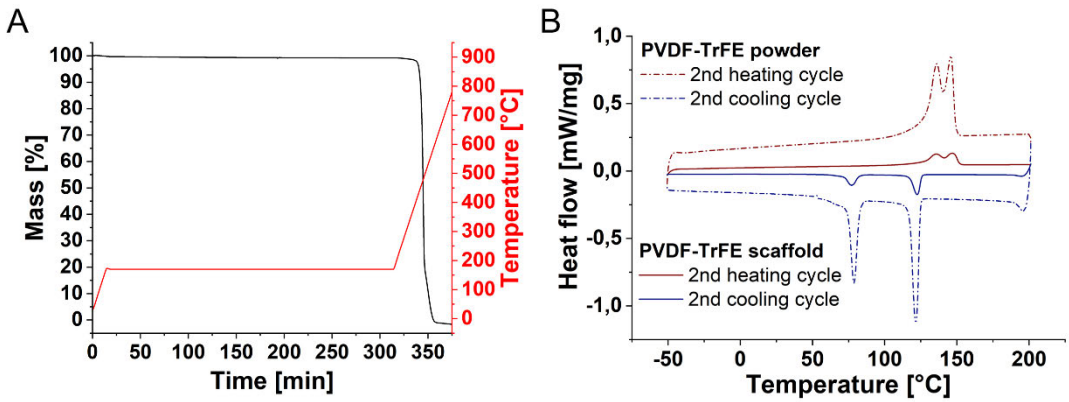

Figure S1. A) The thermogravimetric analysis for P(VDF-*co*-TrFE) powder held at 5 h at 170 °C, and subsequent elevation in temperature shows minimal, if any, degradation at the processing temperature over prolonged periods. B) DSC thermograms showing all heating (red) and cooling (blue) cycles of the commercial P(VDF-*co*-TrFE) powder (dashed lines) and a MEW-processed scaffold (solid lines).

The DSC measurements of the P(VDF-*co*-TrFE) powder and the MEW-processed fibers (Figure S1B) allowed the evaluation of changes in the crystal structure. For the raw powder and the MEW-processed fibers, two peaks within the

individual heating cycles were detected. For the second heating cycle, the two peaks are at 135-136 °C corresponding to the ferroelectric-to-paraelectric transition at the Curie temperature of the P(VDF-*co*-TrFE) [1-3] and the peaks at 146 °C for both, the powder and the scaffold, indicate the melting temperature of the crystalline phase.[1]

The cooling cycles show two endothermic peaks for each cycle at around 121 °C and 78 °C for the powder and similar peaks at 122 °C and 76 °C for the MEW scaffolds. The first peak at around 120 °C corresponds to the recrystallization and solidification process of the polymer melt. The second peak at approximately 80 °C can be correlated to the Curie transition temperature which, when cooling, is significantly lower than when heating P(VDF-*co*-TrFE).[4, 5]

Fiber diameter

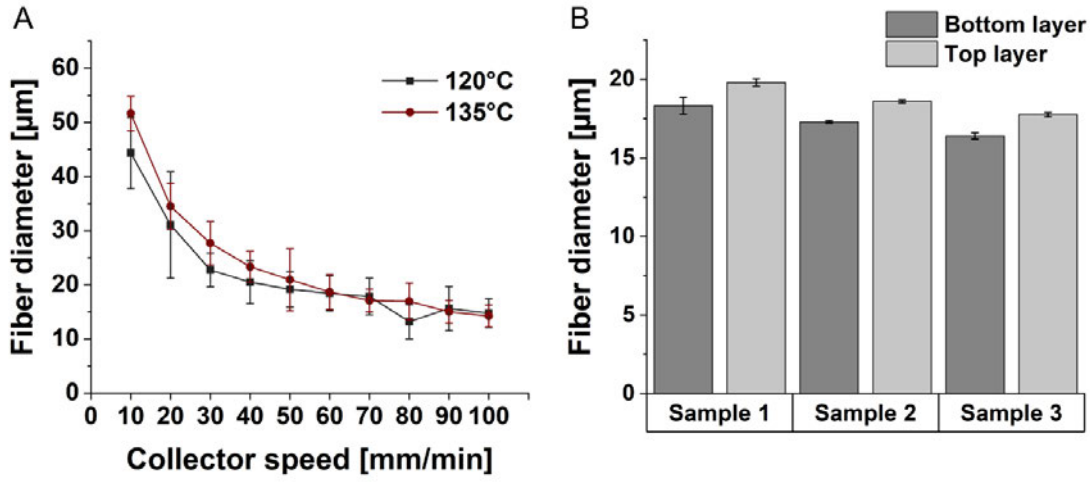

Figure S2. A) showing the relationship between the fiber diameter and collector speed at the two different collector temperatures of 120 °C and 135 °C. B) showing the measured fiber diameters of the top and bottom layers of the scaffold.

X-ray diffraction (XRD) and crystallinity

The degree of crystallinity of the measured scaffolds is defined as the fraction of the signal area produced by the crystalline parts of the scaffold divided by the sum of the amorphous and crystalline areas using the Software DIFFRAC.TOPAS (Figure S3). To isolate the crystalline, amorphous and general background contributions in the diffractogram, a separate diffractogram of an empty sample holder was measured. In DIFFRAC.TOPAS a whole pattern fitting technique was used introducing peaks phase, which were, after the refinement, in the following steps fixed to the resulting values to represent the general background contributions of the sample holder (purple). The different crystalline modifications of P(VDF-*co*-TrFE) were introduced to the refinement as *hkl* phases with lattice parameters

based on the values presented by Lee *et al*. [6]. These parameters have been adjusted and fixed on the measurement of the raw P(VDF-*co*-TrFE) powder, as this was the source material (Figure S3A). Lastly, the amorphous phase content was then tried to define as the difference between the general background and the before refined crystalline contributions. However, there the whole pattern fitting techniques shows some limitations, as the background and the amorphous phase did interact while calculating within the software. Therefore, the focus was only set on the ratio between the α- and β-phase. Following this scheme, for each sample (powder and MEW-processed scaffolds) the diffractogram was separated into sample holder and crystalline area with the contribution of α- and β-phase content within the measured diffractogram (Figure S3). Analyzation was performed for the raw powder and MEW-processed scaffolds with collector speeds of 50, 70 and 100 mm/min at collector temperatures of 120 °C and 135 °C for n=3 samples (Table S1).

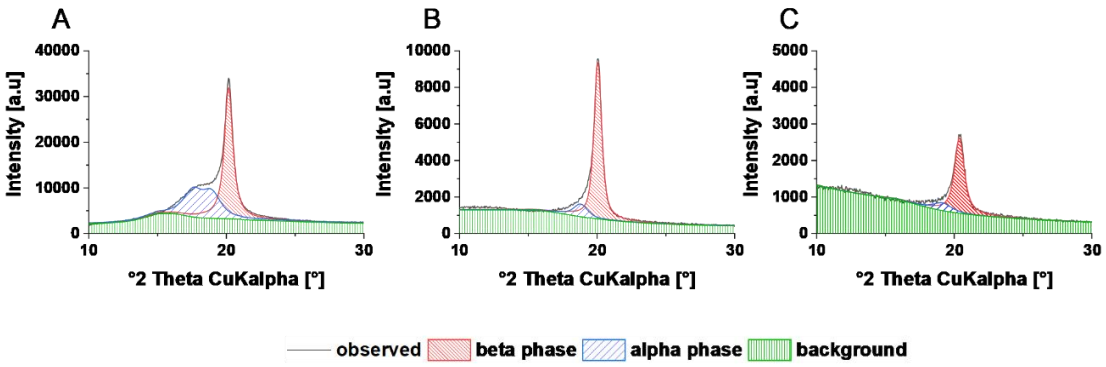

Figure S3. Refinement for the XRD measurements to calculate the crystallinity and the α- and β-phase content. XRD measurements with the refinements and the separated phases for A) the neat powder, B) MEW scaffold printed at 70 mm/min at a collector temperature of 120 °C and C) a MEW scaffold printed at 70 mm/min at a collector temperature of 135 °C.

Table S1. Related α-, β-phase contents of the crystalline components for the MEW-processed scaffolds printed at 50, 70 and 100 mm/min at collector temperatures of 120 °C and 135 °C, respectively compared to the unprocessed powder (n=3).

powder			50 mm/min		70 mm/min		100 mm/min	
α	β		α	β	A	β	α	β
content [%]			content [%]					
37±1	63±1	120 °C	18±0	82±0	14±3	86±3	15±2	85±2
		135 °C	10±4	90±4	15±2	85±2	10±4	90±4

Atomic force microscopy (AFM) and piezo force microscopy (PFM)

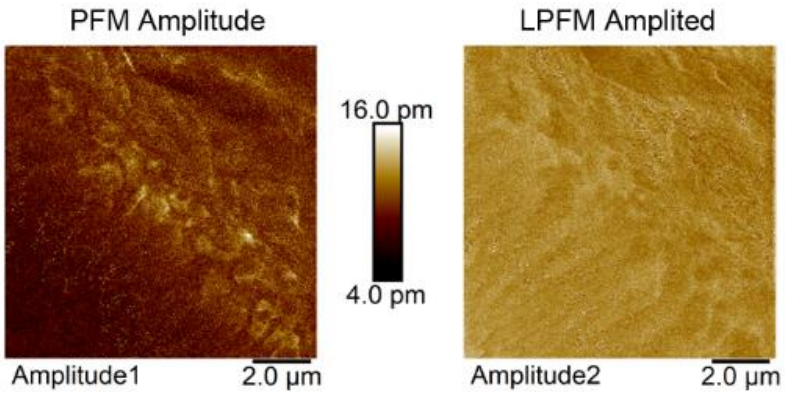

Figure S4. PFM and LPFM images at AC bias voltage = 10 V.

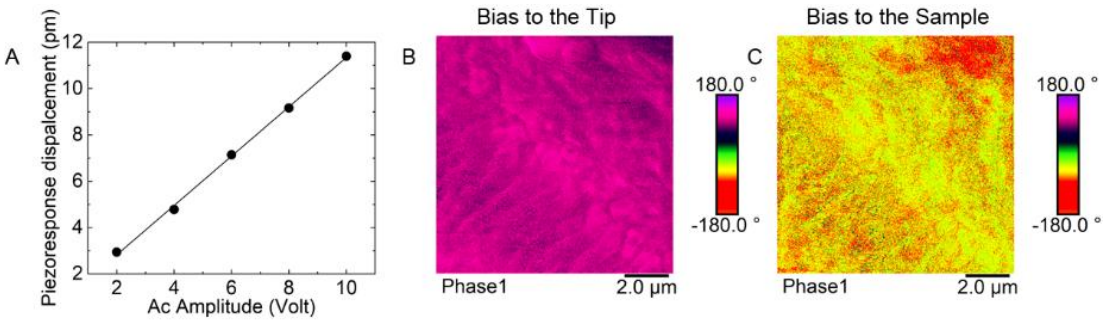

Figure S5. A) Plot of the measured PFM displacement *vs.* applied voltage (dots). The line is the linear fit to the experimental data, yielding an effective coefficient of 1.2 pm/V. PFM phase micrographs highlighting the phase signal inversion when a bias of 10 V is applied to B) the tip or to C) the sample.

Video S1. Showing the oscillating/vibrating jet of the P(VDF-*co*-TrFE) with 0.25x original speed.

Video S2. MEW-processing of the P(VDF-*co*-TrFE) with pressures higher than 0.5 bar causing jet break-ups due to the attraction of the jet towards the print head shown with 1.5x original speed.

Video S3. Jet initiation with and without heated collector.

Video S4. Showing the jet lags at speeds of 10, 50, 70 and 100 mm/min from a straight and vertical jet to increasing jet lags with increasing speed to a highly stretched jet at 100 mm/min.

Video S5. Bending behavior of the 0-90° scaffold printed with a speed of 70 mm/min while cooling down the collector temperature from 120 °C. The scaffold has a thickness of 10 alternating layers in x- and y-direction.

References

[1] F. Oliveira, Y. Leterrier, J.-A. Månson, O. Sereda, A. Neels, A. Dommann, D. Damjanovic, Process influences on the structure, piezoelectric, and gas-barrier properties of PVDF-TrFE copolymer, Journal of Polymer Science Part B: Polymer Physics 52(7) (2014) 496-506.

[2] R. Gregorio Jr, M.M. Botta, Effect of crystallization temperature on the phase transitions of P(VDF/TrFE) copolymers, Journal of Polymer Science Part B: Polymer Physics 36(3) (1998) 403-414.

[3] A.J. Lovinger, T. Furukawa, G.T. Davis, M.G. Broadhurst, Crystallographic changes characterizing the Curie transition in three ferroelectric copolymers of vinylidene fluoride and trifluoroethylene: 2. Oriented or poled samples, Polymer 24(10) (1983) 1233-1239.

[4] M.A. Barique, H. Ohigashi, Annealing effects on the Curie transition temperature and melting temperature of poly(vinylidene fluoride/trifluoroethylene) single crystalline films, Polymer 42(11) (2001) 4981-4987.

[5] K. Koga, H. Ohigashi, Piezoelectricity and related properties of vinylidene fluoride and trifluoroethylene copolymers, Journal of Applied Physics 59(6) (1986) 2142-2150.

[6] Y. Lee, K.L. Kim, H.S. Kang, B. Jeong, C. Park, I. Bae, S.J. Kang, Y.J. Park, C. Park, Epitaxially Grown Ferroelectric PVDF-TrFE Film on Shape-Tailored Semiconducting Rubrene Single Crystal, Small 14(22) (2018) e1704024.

A2. Statements on individual author contributions

Publication (complete reference): J.C. Kade, P.D. Dalton, *Polymers for Melt Electrowriting*, Advanced Healthcare Materials 10(1) (2021) 2001232.					
Participated in	**Author Initials,** Responsibility decreasing from left to right				
Study Design Methods Development	JCK	PDD			
Data Collection	JCK	PDD			
Data Analysis and Interpretation	JCK	PDD			
Manuscript Writing Writing of Introduction Writing of Materials & Methods Writing of Discussion Writing of First Draft	JCK	PDD			

Publication (complete reference): J.C. Kade, P.D. Dalton, *Polymers for Melt Electrowriting*, Advanced Healthcare Materials 10(1) (2021) 2001232.		
Figure	**Author Initials,** Responsibility decreasing from left to right	
1	JCK	PDD
2	JCK	PDD
3	JCK	PDD
4	JCK	PDD
5	JCK	PDD
6	JCK	PDD
7	JCK	PDD
8	PDD	JCK
9	PDD	JCK

Explanations (if applicable):

Publication (complete reference): J.C. Kade, B. Tandon, J. Weichhold, D. Pisignano, L. Persano, R. Luxenhofer, P.D. Dalton, *Melt Electrowriting of Poly(vinylidene fluoride-co-trifluoroethylene)*, Polymer International n/a (n/a). (https://doi.org/10.1002/pi.6272).							
Participated in	**Author Initials,** Responsibility decreasing from left to right						
Study Design Methods Development	JCK	BT	JW	LP	PDD	RL	DP
Data Collection	JCK	BT	JW	LP	PDD	RL	DP
Data Analysis and Interpretation	JCK	BT	JW	LP	PDD	RL	DP
Manuscript Writing Writing of Introduction Writing of Materials & Methods Writing of Discussion Writing of First Draft	JCK	BT	PDD	RL	LP	JW	DP

Publication (complete reference): J.C. Kade, B. Tandon, J. Weichhold, D. Pisignano, L. Persano, R. Luxenhofer, P.D. Dalton, *Melt Electrowriting of Poly(vinylidene fluoride-co-trifluoroethylene)*, Polymer International n/a (n/a). (https://doi.org/10.1002/pi.6272).

Figure	**Author Initials, Responsibility decreasing from left to right**						
1	JCK	BT	PDD	RL	JW	LP	DP
2	JCK	BT	PDD	RL	JW	LP	DP
3	JCK	BT	PDD	RL	JW	LP	DP
4	JCK	BT	PDD	RL	JW	LP	DP
5	JCK	JW	BT	PDD	RL	LP	DP
6	LP	JCK	BT	PDD	RL	JW	DP
S1	JCK	BT	PDD	RL	JW	LP	DP
S2	JCK	BT	PDD	RL	JW	LP	DP
S3	JW	JCK	BT	PDD	RL	JW	DP
S4	LP	DP	JCK	BT	PDD	RL	JW
S5	LP	DP	JCK	BT	PDD	RL	JW

Publication (complete reference): J.C. Kade, P.F. Otto, R. Luxenhofer, P.D. Dalton, *Melt electrowriting of poly(vinylidene difluoride) using a heated collector*, Polymers for Advanced Technologies n/a (n/a). (accepted article DOI: 10.1002/pat.5463).

Participated in	**Author Initials,** Responsibility decreasing from left to right				
Study Design Methods Development	JCK	PFO	PDD	RL	
Data Collection	PFO	JCK	PDD	RL	
Data Analysis and Interpretation	JCK	PFO	PDD	RL	
Manuscript Writing Writing of Introduction Writing of Materials & Methods Writing of Discussion Writing of First Draft	JCK	PDD	PFO	RL	

Publication (complete reference): J.C. Kade, P.F. Otto, R. Luxenhofer, P.D. Dalton, *Melt electrowriting of poly(vinylidene difluoride) using a heated collector*, Polymers for Advanced Technologies n/a (n/a). (accepted article DOI: 10.1002/pat.5463).

Figure	**Author Initials,** Responsibility decreasing from left to right			
1	JCK	PFO	PDD	RL
2	PDD	JCK	PFO	RL
3	JCK	PFO	PDD	RL

Explanations (if applicable): This work is part of the project thesis of Paul F. Otto who was directly supervised by Juliane C. Kade. J.C. Kade conducted the contact angle measurements, XRD measurements and further printing experiments.

Publication (complete reference): *Manuscript in preparation (close to submission); changes for the title and participation might change.* J.C. Kade, E. Bakirci, B. Tandon, Danila Gorgol, M. Mrlik, R. Luxenhofer, P. D. Dalton, *Melt Electrowriting of substituted Poly(vinylidene fluoride) with carbonyl iron (CI) particles.*							
Participated in			**Author Initials,** Responsibility decreasing from left to right				
Study Design Methods Development	JCK	BT	EB	MM	DG	PDD	RL
Data Collection	JCK	MM T	EB	B	DG	PDD	RL
Data Analysis and Interpretation	JCK	MM	EB	BT	DG	PDD	RL
Manuscript Writing Writing of Introduction Writing of Materials & Methods Writing of Discussion Writing of First Draft	JCK	MM	EB	BT	RL	PDD	DG

Publication (complete reference):): *Manuscript in preparation (close to submission); changes for the title and participation might change.* J.C. Kade, E. Bakirci, B. Tandon, Danila Gorgol, M. Mrlik, R. Luxenhofer, P. D. Dalton, *Melt Electrowriting of substituted Poly(vinylidene fluoride) with carbonyl iron (CI) particles.*							
Figure			**Author Initials,** Responsibility decreasing from left to right				
1	MM	JCK	DG	EB	BT	PDD	RL
2	JCK	BT	EB	MM	DG	PDD	RL
3	JCK	BT	EB	PDD	RL	MM	DG
4	EB	BT	JCK	PDD	RL	MM	DG
Table 1	MM	JK	EB	BT	RL	PDD	DG
Table 2	JCK	BT	EB	RL	PDD	MM	DG
S1	JCK	BT	EB	MM	DG	PDD	RL
S2	MM	JK	EB	BT	RL	PDD	DG
S3	BT	JCK	EB	PDD	RL	MM	DG
Video S1	JCK	BT	EB	PDD	RL	MM	DG
Video S2	BT	JCK	EB	PDD	RL	MM	DG

The doctoral researcher confirms that she/he has obtained permission from both the publishers and the co-authors for legal second publication.

The doctoral researcher and the primary supervisor confirm the correctness of the above mentioned assessment.

Juliane Carolin Kade	12/11/21	Helsinki	
Doctoral Researcher's Name	Date	Place	Signature

Prof. Paul D. Dalton	11/11/2021	Eugene, Oregon (U	
Primary Supervisor's Name	Date	Place	Signature

A3. Abbreviations

2D	Two-dimensional
3D	Three-dimensional
4D	Four-dimensional
AC	Acryloyl carbonate
AFM	Atomic force microscopy
AM	Additive manufacturing
AMP	Amorphous magnesium phosphate
Al	Aluminum
Au	Gold
BG	Bioactive glass
bmMSCs	Human bone-marrow mesenchymal stromal cells
ε-CL	ε-caprolactone
CAD	Computer-aided design
CaP	Calcium phosphate
$CoFe_2O_4$	Cobalt iron oxide
CI	Carbonyl iron
CTS	Critical translation speed
DMEM	Dulbecco's Modified Eagle Medium
DI water	Deionized water
DSC	Differential scanning calorimetry
EAPs	Electroactive polymers
ECM	Extracellular matrix
EDX	Energy-dispersive X-ray spectroscopy
EHD	Electrohydrodynamic
FCS	Fetal calf serum
FDA	Food and Drug Administration
FDM	Fused deposition modeling
Fe	Iron
FIB	Focused ion beam
G	Gauge
GelMA	Gelatin methacryloyl
GIF	Graphics Interchange Format
GMP	Good-manufacturing practices
HAp	Hydroxyapatite
HV	High voltage
IR	Infrared
L929	Murine fibroblast cell line
LLA	L-lactide
MES	Melt electrospinning
MEW	Melt electrowriting
MFI	Melt flow index
MgP	Magnesium phosphate
M_n	Number average molecular weight
M_w	Weight average molecular weight
N_2	Nitrogen
PCL	Poly(ε-caprolactone)
PDMS	Poly(dimethyl siloxane)
PEG	Poly(ethylene glycol)
PEtOx	Poly(2-ethyl-2-oxazoline)
PEtOx-ButenOx	Poly(2-ethyl-2-oxazoline-*co*-2-(3-butenyl)-2-oxazoline)

PEtOzi	Poly(2-ethyl-2-oxazine)
PFM	Piezo-force microscopy
pHMGCL	Poly(hydroxymethylglycolide-*co*-*ε*-caprolactone)
PLA-PEG-PLA	Poly(lactide-*block*-ethylene glycol-*block*-lactide)
POx	Poly(2-oxazoline)s
Poly(LLA-AC)	Poly(L-lactide-*co*-acryloyl carbonate)
Poly(LLA-*ε*-CL-AC)	Poly(L-lactide-*co*-*ε*-caprolactone-*co*-acryloyl carbonate)
PP	Poly(propylene)
PPy	Polypyrrole
PVA	Polyvinyl alcohol
PVDF	Poly(vinylidene fluoride)
P(VDF-*co*-TrFE)	Poly(vinylidene fluoride-*co*-trifluoroethylene)
rGO	Reduced graphene oxide
r.h.	Relative humidity
RT	Room temperature
ROX	Roxithromycin
SEM	Scanning electron microscopy
SES	Solution electrospinning
sP(EO-*stat*-PO)	Six-arm star-shaped NCO-poly(ethylene oxide-*stat*-propylene oxide)
SrBG	Strontium-substituted bioactive glass
TGA	Thermogravimetric Analysis
TPE	Thermoplastic elastomer
UV	Ultraviolet
VSM	Vibrating sample magnetometer
XRD	X-ray diffraction

A4. Curriculum Vitae

A5. Publications and conference contributions

Publications

As the first author:

Kade, JC, Otto, PF, Luxenhofer, R, Dalton, PD. Melt electrowriting of poly(vinylidene difluoride) using a heated collector. *Polym Adv Technol*. 2021; 32(12): 4951- 4955. https://doi.org/10.1002/pat.5463

Kade, J.C., Tandon, B., Weichhold, J., Pisignano, D., Persano, L., Luxenhofer, R. and Dalton, P.D. (2021), Melt electrowriting of poly(vinylidene fluoride-*co*-trifluoroethylene). *Polym Int*, 70: 1725-1732. https://doi.org/10.1002/pi.6272

Kade, J. C., Dalton, P. D., Polymers for Melt Electrowriting. *Adv. Healthcare Mater*. 2020, 10, 2001232. https://doi.org/10.1002/adhm.202001232

As a co-author:

Großhaus, C., Bakirci, E., Berthel, M., Hrynevich, A., Kade, J. C., Hochleitner, G., Groll, J., Dalton, P. D., Melt Electrospinning of Nanofibers from Medical-Grade Poly(ε-Caprolactone) with a Modified Nozzle. *Small* 2020, 16, 2003471. https://doi.org/10.1002/smll.202003471

Conference contributions

11/2019 The Belgian Symposium on Tissue Engineering
"*Melt electrowriting of poly(vinylidene fluoride-trifluoroethylene)*";
Poster presentation; Hasselt, Belgium

12/2020 11th World Biomaterials Congress
"*Melt Electrowriting of Poly(Vinylidene Difluoride) and its Copolymers*"
Oral presentation; Online conference

09/2021 31st Annual Conference of the European Society for Biomaterials (ESB 2021)
"*Melt Electrowriting of Polymers beyond Poly(ε-caprolactone) with Focus on Electroactive Materials*"
Oral presentation; Online conference

A6. Acknowledgement / Danksagung

First of all, thank you to everyone who was involved and always supported me during these three-year PhD journey. I really enjoyed the time, and most important I learned so many things starting with MEW to research in general and especially about myself. I would definitely do it again and I´m very thankful for all the experiences, and enthusiastic and fantastic people I met.

I deeply thank Paul Dalton, my doctor-father, for your continuous trust and support always believing in me and giving me the opportunity for this important chapter in my life. You are such an inspiring and enthusiastic researcher teaching me so many things and showing me that writing is enjoyable. Thank you, Paul, for always listening and especially showing me to *choose my battlefield* and to *work hard, play hard*. You really deserve the title of being a doctor-father! Thank you!

I also want to thank my co-supervisor, Robert Luxenhofer for providing critical feedback and support throughout the project. Furthermore, to give me the opportunity and support to join your lab and great team at the University of Helsinki challenging myself with tough projects while writing my thesis and to leave my comfort zone moving to the beautiful country Finland. This definitely completed my PhD journey.

Furthermore, thank you Rylie Green for your support, helpful discussions, and input. Additionally, I want to thank the VW foundation for the project funding enabling to work in a great team including Julian Heck, Jochen Löblein, as well as Andrei Hrynevich and Harald Hümpfer designing and building the coaxial print-head. Additionally, I appreciate the fruitful projects with our collaboration partners resulting in nice papers.

I also want to thank the support of the Joachim Herz Foundation and for all the nice online and in-person meetings, as well as being part of the Add-on Fellow community enabling to connect and collaborate with other young researchers in different interdisciplinary fields.

Moreover, I thank the whole FMZ for providing a supportive and friendly environment to conduct my research in the very well-equipped labs. And I especially want to thank Toni and Harald for always helping with any problem, as well as Tanja, Birgit and Diana for your administrative support and all the very nice conversations. Judith and Philipp your SEM images are amazing and Philipp thanks for cutting and visualizing all the coaxial fibers.

Special thanks to the whole MEW lab members and students for all your help, support, as well as nice and fun discussions and conversations: I really enjoyed working together with all of you and had a lot of fun!

Paul, you did a great job during your project- and master thesis and I´m happy that I had the chance to supervise you, as well as Anna-Lena and Andreas for your Hiwi project working with the coaxial MEW printer.

To the polymers group at the University of Helsinki, I really appreciate warmly welcoming me in the dark and cold Finland and being part of the team not only getting to know new colleagues but even becoming friends. Thanks for the three months and two more to come.

Office A009 - Biranche and Ezgi – thank you soooo much for everything and for making the office space greener! Our discussions about research and life, cakes, coffees, lunch dates, future and all the time together in the lab. Ezgi, you were always there, always helping, always hugging, always open for fun and always had an open ear!

Finally, thank you to my friends and family for standing by throughout all the years of studying, especially you Mom. All of you continuously supported me through all the ups and downs, drawbacks, and successes.

My deepest thanks belong to you, Flo! At all times, you provided safety and hold, encouraged me to leave my comfort zone and supported me going abroad not only once.

A7. Affidavit

I hereby confirm that my thesis entitled "*Expanding the Processability of Polymers for a High-Resolution 3D Printing Technology*" is the result of my own work. I did not receive any help or support from commercial consultants. All sources and / or materials applied are listed and specified in the thesis.

Furthermore, I confirm that this thesis has not yet been submitted as part of another examination process neither in identical nor in similar form.

Place, Date *Signature*

A8. Eidesstattliche Erklärung

Hiermit erkläre ich an Eides statt, die Dissertation „*Erweiterung der Verarbeitbarkeit von Polymeren für eine hochauflösende 3D-Drucktechnologie*“ eigenständig, d.h. insbesondere selbständig und ohne Hilfe eines kommerziellen Promotionsberaters, angefertigt und keine anderen als die von mir angegebenen Quellen und Hilfsmittel verwendet zu haben.

Ich erkläre außerdem, dass die Dissertation weder in gleicher noch in ähnlicher Form bereits in einem anderen Prüfungsverfahren vorgelegen hat.

Ort, Datum *Unterschrift*